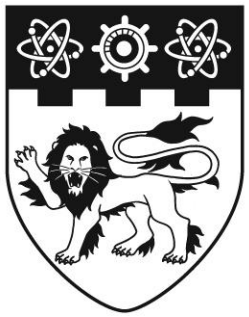

NANYANG
TECHNOLOGICAL
UNIVERSITY

Liquid Crystal Spiral Phase Plate: Design, Fabrication and Characterization

Wang Qin

School of Electrical & Electronic Engineering

2008

Liquid Crystal Spiral Phase Plate: Design, Fabrication and Characterization

Wang Qin

School of Electrical & Electronic Engineering

A thesis submitted to the Nanyang Technological University

in fulfillment of the requirement for the degree of
Doctor of Philosophy

2008

Acknowledgments

Abstract

Optical vortices have both theoretical and application value, and have attracted many research interests. Using spiral phase plates (SPP) to generate optical vortices has the advantages of high conversion efficiency and flexibility in applications. Moreover, SPP have found applications in edge contrast enhancement in microscopy, optical vortex coronagraph and generating radially polarized beams etc. Among various kinds of SPP, Liquid crystal spiral phase plates (LC SPP) have the potential advantages of dynamic switching between optical vortices with different topological charge, adaptability to any visible wavelength and capability to realize high slice number etc. These are unique advantages of LC SPPs comparing with other kinds of SPP.

Three types of LC SPP with progressing performance have been designed, fabricated and tested. The optical vortices were observed through the Fraunhofer diffraction patterns of LC SPP. The interference patterns between optical vortices generated by LC SPP and its coherent Gaussian beams were observed and used for the determination of topological charge. Unique advantages of LC SPP, such as generation and dynamic switching of optical vortices with different topological charges, adaptability to any visible wavelength etc, were realized.

The mechanism of the conversion efficiency degradation of LC SPP was experimentally studied, and solution to this problem was proved effective. The phenomena

of discreteness and distortion of the optical vortices generated by LC SPP were observed, and the explanations based on comparisons between experiment and simulation results were given. The relationship between the total slice number and the purity of topological charge of optical vortices generated by multi-level SPP was found through Fourier analysis.

A batch fabrication process for LC SPP developed was introduced in detail. Improvements to the glass scribing process, sealant drawing process, LC filling process and cell gap control technique etc are described in detail.

A phase shift measurement system was successfully developed to measure the phase shift versus driving voltage of LC SPP. This system is based on a Michelson interferometer with a detector of linear photo detector array. A trough position method was used to extract the phase information from equidistant fringes. The thermal drift and non-thermal drift of the system was observed. The measurement accuracy of this system was evaluated by measuring the displacement of a piezoelectric actuated mirror, and the experiment results show 0.2 nm or 0.1 ^{o}of standard deviation can be achieved.

Rotational frequency shift (RFS) is the frequency shift arises from the relative rotational motion between an optical vortex and an observer.RFS was observed and measured in mm-wavelength and optical wavelength by specially designed optical systems in 1997 and 2003, respectively. In this thesis, it is shown that RFS can also be observed and measured in a more straightforward way, i.e., through the interference

pattern of optical vortices generated by LC SPP. Further, it is found that angular momentum can also be determined from RFS according to energy conservation law. The same idea was found applicable to the cases of Doppler frequency shift and frequency shift caused by rotational circularly polarized light. This implies an intrinsic relationship between frequency shift and momentum of photons.

Abbreviations

LC	liquid crystal
LCD	liquid crystal display
OV	optical vortex/vortices
SPP	spiral phase plate
HG	Hermit-Gaussian
LG	Laguerre-Gaussian
LPDA	linear photo detector array
OAM	orbital angular momentum
RFS	rotational frequency shift
SLM	spatial light modulator

List of Figures

List of Tables

Table of Contents

Chapter 1 Introduction

1.1 Background

1.1.1 Optical vortices and its applications

Vortices, such as tornado and water vortices, which exist in air and water, are well known to most people. The less-well-known is that vortices can also exist in light beams, which are called optical vortices.

Optical vortices have helical wave front, null intensity center. The Poynting vector of an optical vortex has a component surrounding the beam axis. It has also been found that Optical vortices carry orbital angular momentum. All these properties of an optical vortex are related to its topological charge number, which is an important parameter of optical vortices.

Optical vortices are interesting phenomena both in theory and applications, and have attracted many research interests. The applications of optical vortices include the study of optical tweezers [1~3], trapping and guiding of cool atoms [4~6], rotational frequency shift [7~9], studies of mode transformation with non-linear frequency doubling [10]; switching helicities as a means of information processing [11]; and entanglement of the orbital angular momentum states of photons [12] etc.

1.1.2 Approaches to generate optical vortices

There are several approaches to generate optical vortices.

The most common approach is the computer generated hologram [13], in which an optical vortex can be obtained as a diffraction beam of the hologram film in certain direction.

The second approach is that, through an asymmetric structure inside a laser cavity, a high order Hermit-Gaussian beam is generated, which is then converted into an optical vortex by two astigmatic lenses [14]. There are also papers on changing the structure inside laser cavity to obtain optical vortices without using cylindrical lens mode converter [15].

The third approach is using a spiral phase plate (SPP) to convert a Gaussian beam into an optical vortex.

1.1.3 The spiral phase plate approach

The spiral phase plate approach has the merits of high conversion efficiency and the coaxiality of the converted and the incident beam comparing with the hologram approach, and flexibility in using comparing with the cylindrical lens mode converter.

Besides the applications of generation of optical vortices, SPPs has also found applications in the generation of radially polarized beams [16], edge contrast enhancement in microscopy [17] and optical vortex coronagraph [18] etc.

Various kinds of SPPs published hitherto are listed as follows, (1) a large pitch spiral phase plate dip into a refractive index matched solution [19]; (2) fabricating multi-steps on the silica material though multi-etching process [20]; (3) by use of excimer laser ablation to make multi-steps on polyimide substrate [21]; (4) employing a diamond tool on a high-precision computer driven lathe to make a mold at first, into the mold a polymer is cast, which is then UV cured [22]; (5) using a deformed cracked plexiglass plate [23]; (6) electron-beam writing in photo resist [24]; (7) multi-stage vapor deposition [25]; (8) using liquid crystal (LC) cell as a phase modulator [26], in this reference, LC SPP which can generate optical vortices with topological charge 1 and topological charge 2 is reported.

1.2 Motivations and objectives

1.2.1 Motivations

Liquid crystal devices, such as LCDs, have electrically tunable optical properties. Making use of liquid crystal, we can realize a tunable SPP, which may open up new applications. In fact, Ganic *et al.* was the first to explore SPP made of LC in 2002 [26]. However, only low topological charge beams (charge 1 and 2) can be generated and the beam quality of topological charge 2 is poor.

Besides, some important topics related to LC SPP are not touched or sufficiently studied, such as the effect due to the nonlinearity of the phase shift versus driving voltage of LC cell; the measurement of phase shift versus driving voltage; diffraction at the edge of slices; the actual conversion efficiency of LC SPP (in reference 26, the conversion efficiency is simply regarded as 100% without any experimental sustention), and the effect

due to the limited slice number of LC SPP etc. It is worth carrying out further studies in these issues.

Comparing with other kinds of SPPs, LC SPPs has potential advantages of generating high quality optical vortices with different topological charges and any fractional topological charge by only one LC SPP, and the adaptability to any visible wavelength. Dynamic switching between optical vortices with different topological charge is possible to achieve with LC SPPs. These unique advantages distinguish LC SPP from other kinds of SPP and have merits in some applications. However, these advantages are not exhibited or fully exhibited in the existing LC SPP, so further works need to be done to improve the existing LC SPP.

1.2.2 Objectives

The objectives of this project is ① To design and fabricate high quality LC SPP, which can be used to generate optical vortices with different topological charge and can be used in any visible wavelength with high conversion efficiency; ② To study some related issues like beam purity of optical vortices generated by a SPP; ③ By improving the existing LC cell fabrication process, to develop efficient batch fabrication process for high quality LC SPP, and meanwhile, to benefit other on-going research projects such as the fabrication of Liquid crystal on silicon (LCoS); ④ To carry out rotational frequency shift related researches with the help of the LC SPP developed.

1.3 Major contributions

(1). The LC SPP, which can be used to generate high quality optical vortices with different topological charge for any visible wavelength, was designed and successfully fabricated. The dynamic switching between optical vortices with different topological charge was achieved.

(2). The mechanism of the conversion efficiency degradation of LC SPP was experimentally studied, and solution to this problem was proved effective. The phenomena of discreteness and distortion of the optical vortices generated by LC SPP were observed, and the explanations based on experimental and simulation results were given. The relationship between the total slice number and the purity of topological charge of optical vortices generated by multi-level SPP was found through Fourier analysis.

(3). An efficient batch fabrication process for LC SPP was developed based on the existing LCD fabrication line. Some improvements were done to the existing machine and process, such as the glass scribing process, sealant drawing process and LC filling process etc. These improvements benefit other related research projects as well.

(4). A phase shift measurement system was successfully developed to measure the phase shift versus driving voltage of LC SPP. A trough position method was used to extract the phase information from equidistant fringes. The experiment results show a standard deviation of 0.2 nm or 0.1 ^{o} can be achieved by using the trough position method. The thermal drift and non-thermal drift of the system was observed.

(5). It is found that RFS can also be observed and measured in a more straightforward way, i.e., through the interference patterns of optical vortices generated by LC SPP. Further, it is found that the orbital angular momentum of the photon of an optical vortex can also be determined by RFS according to energy conservation law. Further, the same idea is found applicable to the cases of Doppler frequency shift and RFS caused by rotational circularly polarized beams.

1.4 Organization of the thesis

In chapter 1, the motivations, objectives, major contributions and the organization of the thesis are introduced.

In chapter 2, The theories, properties, applications and generation of optical vortices are reviewed; the principle of LC SPP are introduced; the merits of generation optical vortices with LC SPP are introduced by comparing with other methods.

In chapter 3, the structure design, experimental results, merits and demerits of three types of LC SPP fabricated are introduced; phenomena related to LC SPP are analyzed in this chapter.

In chapter 4, the developing of the phase shift measurement system and its application in the measurement of phase shift versus voltage of LC SPP and displacement of piezoelectric actuated mirror are described.

In chapter 5, the methodology, machinery and principle of the fabrication processes of LC SPP are introduced.

In chapter 6, the major improvements to the existing LC cell fabrication process, such as glass scribing process, sealant drawing process, LC filling process and cell gap control technology are described.

In chapter 7, the observing and measurement of rotational frequency shift through the interference patterns of optical vortices generated by LC SPP and the determination of orbital angular momentum from rotational frequency shift are introduced.

In chapter 8, conclusions and recommendations are presented.

Chapter 2 Background of optical vortices and LC SPP

2.1 Optical vortex and Laguerre-Gaussian modes

Optical vortices are laser beams containing phase singularities. Generally, a phase singularity is such a point, in the plane that contains this point and perpendicular to the propagation direction of the light beam, the line integral of the gradient of phase over a closed line around this point is equal to a integer multiple of 2π. Mathematically, it can be expressed as [27],

$$\oint \nabla\Phi \cdot d\vec{q} \Big/ \oint d\vec{q} = 2l\pi \tag{2.1}$$

where Φ represents the phase function; l is an integer.

Under the paraxial approximation, electromagnetic waves in free space satisfy paraxial wave equation. In rectangular coordinates, the solutions to the paraxial equation are Hermite-Gaussian (HG) solutions; while in cylindrical coordinates, the solutions are Laguerre-Gaussian (LG) solutions [28]. Since both the HG and LG functions are a complete basis set of orthogonal functions, any wave satisfying the paraxial approximation can be expanded in terms of either HG or LG solutions [29]. For optical beams having larger amount of cylindrical symmetry, like optical vortices, it would be more convenient to expand the beams in terms of LG solutions.

The expression of the LG solutions can be stated as following [28]:

$$u_{pl}(\rho,\phi,z) = C_{pl}\cdot(\frac{1}{w})\exp(-i\frac{k\rho^2}{2R})\exp(-\frac{\rho^2}{w^2})\exp(-i(2p+l+1)\psi)$$
$$\exp(-il\phi)\cdot(-1)^p(\frac{\sqrt{2}\rho}{w})^l L_p^l(\frac{2\rho^2}{w^2}) \quad (2.2)$$

where u is the complex scalar wave amplitude which describes the transverse profile of the beam. p, l can be either zero or any positive integer. z_R is the Rayleigh range, $R(z) = (z_R^2 + z^2)/z$, $\frac{1}{2}kw^2(z) = (z_R^2 + z^2)/z_R$, $\psi(z) = \arctan(z/z_R)$, C_{pl} is a normalization constant, $k = 2\pi/\lambda$ is the wave number, ρ,ϕ and z are parameters of cylindrical coordinates, $L_p^l(x)$ is the generalized Laguerre polynomial with [30], $L_n^s(x) = \frac{e^x}{x^s}\cdot\frac{d^n}{dx^n}(e^{-x}x^{n+s})$. Some low-order generalized Laguerre polynomials are shown in Table 2-1

Table 2-1: Some low-order Generalized Laguerre polynomials

$L_0^0 = L_0^1 = L_0^2 = ... = L_0^n = 1$		
$L_1^1 = 2 - x$	$L_2^1 = x^2 - 6x + 6$	$L_3^1 = -x^3 + 12x^2 - 36x + 24$
$L_1^2 = 3 - x$	$L_2^2 = x^2 - 8x + 12$	$L_3^2 = -x^3 + 15x^2 - 60x + 60$
$L_1^3 = 4 - x$	$L_2^3 = x^2 - 10x + 20$	$L_3^3 = -x^3 + 18x^2 - 90x + 120$

The LG solutions are composed of infinite discrete terms; they are also called LG modes. The phase Φ depends on azimuthal angle ϕ by $\Phi = l\phi$. It can be easily verified that LG modes satisfy Eq. (2.1), therefore LG modes are optical vortices.

From Eq. (2.2), the transverse intensity profiles of LG modes can be expressed as:

$$u_{pl}(\rho,\phi,z)u_{pl}^{*}(\rho,\phi,z) = C_{pl}^{2}\cdot\frac{1}{w^{2}}(\frac{\sqrt{2}\rho}{w})^{2l}\exp(-\frac{\rho^{2}}{w^{2}})\left[L_{p}^{l}(\frac{2\rho^{2}}{w^{2}})\right]^{2} \tag{2.3}$$

The profile diagrams of several LG modes are shown in Fig. 2.1. All these modes have zero intensity in their centers. Because of this, sometimes they are called "doughnut beam".

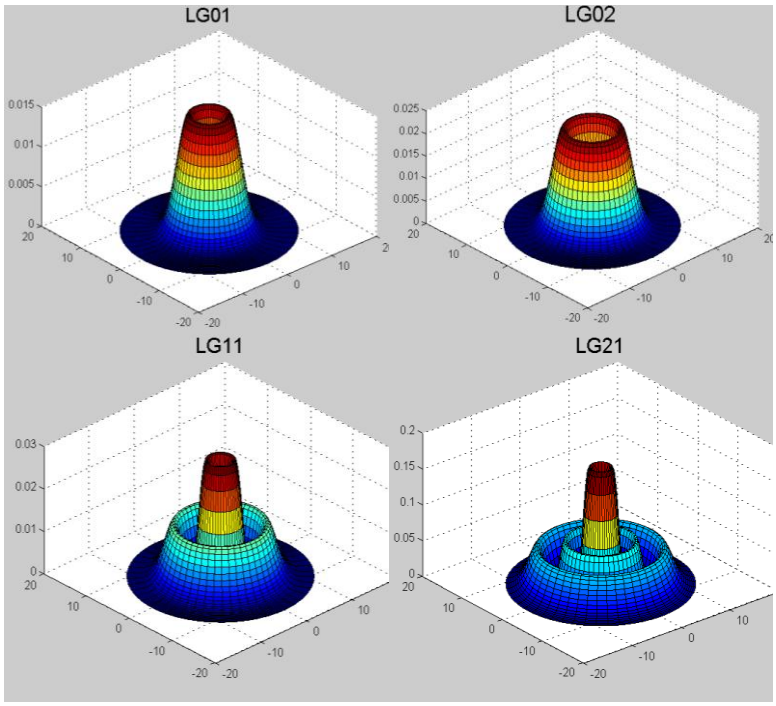

Fig. 2.1 Transverse intensity profiles of several LG modes.

The LG modes have another version of expression, which is slightly different from Eq. (2.2). If the term of $\exp(-il\phi)$ in Eq. (2.2) is replaced by $\cos(l\phi)$, then the new expression also satisfies paraxial equation, forming an equivalent solution set as the previous one. In this case, the transverse intensity profiles can be expressed as Eq (2.4), and the mode patterns are shown in Fig. 2.2 [31].

$$u_{pl}(\rho,\phi,z)u_{pl}^{*}(\rho,\phi,z) = C_{pl}^{2}\cdot\frac{1}{w^{2}}(\frac{\sqrt{2}\rho}{w})^{2l}\exp(-\frac{\rho^{2}}{w^{2}})\left[L_{p}^{l}(\frac{2\rho^{2}}{w^{2}})\right]^{2}\cos^{2}(l\phi) \qquad (2.4)$$

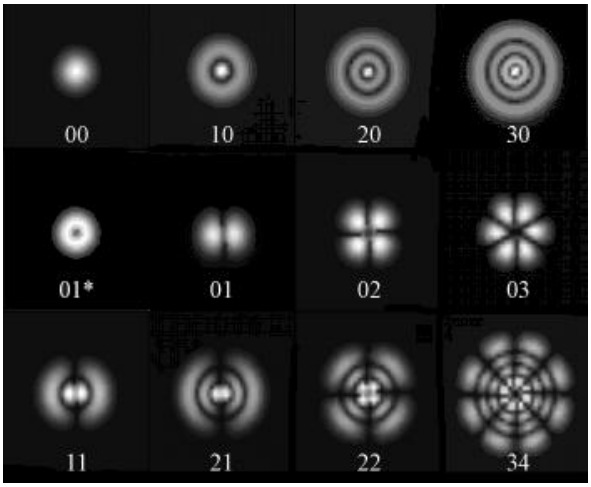

Fig. 2.2 Transverse intensity profiles as expressed in Eq.2.4.

It can be seen clearly from Fig. 2.2 that, the number of nodes is equal to p in radial direction and equal to l in azimuthal direction. Because of this, p is known as radial index, and l is azimuthal index, which is also called topological charge that is more often used in literatures.

2.2 Properties of LG beam

2.2.1 Momentum

The momentum density is equal to the cross product of the time average of the real part of electric field and magnetic field, i.e. $\varepsilon_0\langle\vec{E}\rangle\times\langle\vec{B}\rangle$. As the electric field amplitude of

LG mode is given by Eq. (2.2), given $\vec{E} = ue^{i\omega t}$, $\vec{B} = -\frac{\exp(j\omega t)}{j\omega}\nabla \times u$, the momentum density can be found as [32]

$$\vec{M} = \frac{1}{c}\left[\frac{rz}{z^2 + z_R^2}|u|^2 \hat{r} + \frac{l}{kr}|u|^2 \hat{\phi} + |u|^2 \hat{z}\right] \tag{2.5}$$

2.2.2 Angular momentum and Poynting vector

The angular momentum of the beam of unit length is the integration of the angular momentum density, i.e. $\vec{r} \times \vec{M}$, over the whole transverse profile.

Since the radial and azimuthal components are symmetric about z axis, the integration over the beam profile leaves only the z component, through Eq. (2.5), the angular momentum of the beam with unit length can be calculated as $\frac{l}{ck}\iint |u|^2 dr d\phi$. Further, the flux of angular momentum along z axis is $\frac{l}{k}\iint |u|^2 r dr d\phi$.

On the other hand, since the Poynting vector is $\langle \vec{E} \rangle \times \langle \vec{H} \rangle$, which is equal to $c^2 \vec{M}$, thus the flux of energy along z axis is $c\iint |u|^2 r dr d\phi$, and the ratio of the flux of angular momentum to the flux of energy is $\frac{l}{kc}$. For a single photon, its energy flux is $h\nu$, so the angular momentum carried by a photon is $l\hbar$.

So far the linearly polarized light beam is considered, in the case of arbitrary polarization, the angular momentum carried by each photon is $l\hbar + \sigma\hbar$, where $\sigma = \mp 1$ for

right-handed or left-handed circularly polarized light and $\sigma = 0$ for linearly polarized light [32].

It should be noted that the Poynting vector for a LG beam has an azimuthal component, which is responsible for the existence of the orbital angular momentum.

2.2.3 Null intensity center

The dark center area of a LG beam is concerned in most applications of optical vortices. Because of the term of $(\frac{\sqrt{2}\rho}{w})^{2l}$ in Eq. (2.3), LG beams with higher topological charge possess a larger radius of dark center. It is worth mentioning: in the case of azimuthal index $p = 0$, the LG beam profile has only a single ring, and the radius of the maximum amplitude is simply $\frac{\sqrt{2}}{2}\omega(z)\sqrt{l}$ [33].

2.3 Working principle of LC phase retarder [34~36]

Liquid crystal (LC) materials are classified into nematic, smectic and cholesteric phases. Almost all the liquid crystal used in LCD and LC phase retarder is nematic liquid crystal. The molecules of nematic liquid crystal have no positional order, but they do have long-range orientational order. Hereafter, liquid crystal refers to the nematic phase liquid crystal, unless otherwise mentioned.

The molecules of liquid crystal have a rod-like shape. The longitudinal direction of the rod molecule is called the director of the molecule. At the ends of the rod, there are

chemical groups. Normally, these terminal groups have some polarity. Due to the existence of the geometry anisotropy and the polar terminal groups, when the external electric field is parallel to the director, the response of the electrons inside the LC molecules is different from the response when external electric field is perpendicular to the director. This anisotropy response of electrons to external electric field account for the anisotropy of permittivity and the anisotropy of refractive index in low frequency and optical frequency range, respectively.

The permittivity in the direction paralleled to the director of molecule is noted as $\varepsilon_{\parallel}$, and that perpendicular to the director of molecule is noted as $\varepsilon_{\perp}$. Similarly, $n_{\parallel}$ means the refractive index when light waves polarized along the director, and $n_{\perp}$ is the refractive index when light waves polarized perpendicularly to the director. In the case when liquid crystal molecules are all aligned in one direction, the liquid crystal layer acts as a birefringent crystal, and $n_{\parallel}$, $n_{\perp}$ sometimes are noted as n_e, n_o, here "e" and "o" mean the extraordinary wave and ordinary wave. All LC materials are positive birefringence, i.e. $n_{\parallel} > n_{\perp}$.

The liquid crystal is referred to as positive liquid crystal if $\varepsilon_{\parallel} > \varepsilon_{\perp}$, and negative liquid crystal if $\varepsilon_{\parallel} < \varepsilon_{\perp}$. The majority of liquid crystal materials used in LCD and phase retarder is positive LC, which is also used in this project. The positive LC molecules tend to align along the electric field direction, while for the negative LC, they tend to align perpendicularly to the electric field direction.

The cell structure of a typical LC phase retarder is shown in Fig. 2.3. Roughly it is a sandwiched structure with liquid crystal layer in between two parallel glass substrates. The two electrodes on both sides of LC layer are made of ITO (a mixture of indium oxide and tin oxide), ITO is a conductive and transparent material. Due to the anti-parallel rubbing treatment in the cell fabrication process, the two alignment layers align LC molecules in one direction with a small tilt angle (1~3) to the substrates. If there is any departure from this most stable alignment state, the LC molecule will experience a restore elastic force to pull it back to its original position.

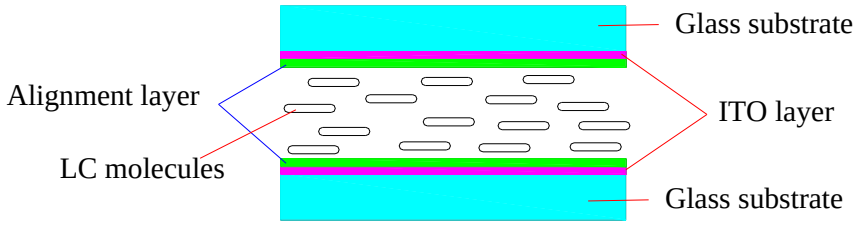

Fig. 2.3 Structure of LC phase retarder (no voltage applied to two ITO electrodes).

When there is no voltage applied to the cell, all the liquid crystal molecules align in one direction approximately parallel to the substrates. Assuming a light beam with wavelength of λ and polarization in the direction of the LC director incidents normally on the cell, it will be given a phase shift of $\frac{2\pi n_{\square} d}{\lambda}$ by the LC layer; where d is the thickness of the LC layer. When a voltage above the threshold voltage of LC is applied to the cell, due to the permittivity anisotropy, the LC molecules tend to turn to align along the electric field direction. Since the elastic force existing in between LC molecules resists this turning, as a

result, the LC molecules stay in a balanced position with their directors in an angle of θ with respect to the light beam, and $0 < \theta < 90^{\circ}$. In this case, the refractive index $n_e(\theta)$ seen by the light beam is determined by $\frac{1}{n_e^2(\theta)} = \frac{\cos^2(\theta)}{n_\perp^2} + \frac{\sin^2(\theta)}{n_{\parallel}^2}$, the value of $n_e(\theta)$ is in between $n_{\parallel}$ and $n_\perp$. With the increasing of the voltage, the force exerted on LC molecule by the electric field takes the advantage, eventually the θ decreases to near zero when the voltage applied is high enough, as shown in Fig. 2.4. The phase shift seen by the light beam changes into $\frac{2\pi n_\perp d}{\lambda}$. Thus, by changing the voltage applied to the LC cell, the polarized light beam experiences a phase shift changing from $\frac{2\pi n_{\parallel} d}{\lambda}$ to $\frac{2\pi n_\perp d}{\lambda}$.

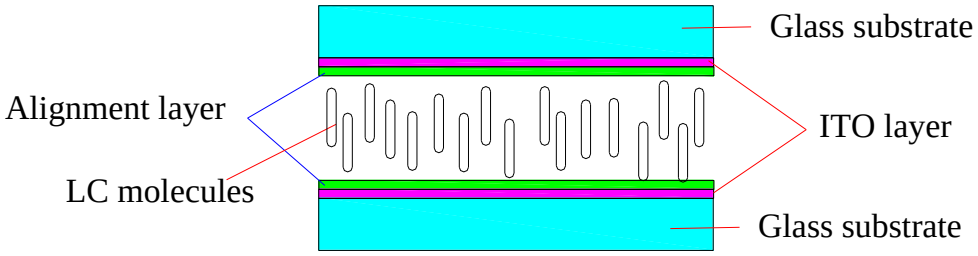

Fig. 2.4 Structure of LC phase retarder (voltage applied to two ITO electrodes).

Apparently, if we wish to make a spiral phase plate with topological charge number up to m, the equation $d\Delta n/\lambda > 2m\pi$ should be satisfied. To obtain the topological charge number as big as possible, $d\Delta n$ should be as large as possible, Δn is determined by LC

material, normally, it has a range of about 0.05~0.25. E48 from Merck is used in this project, with Δn of 0.23. The cell gap d is controlled by spacer material, normally 5~7 μm for LCD, particularly large spacer up to 18 μm is used in the fabrication of LC SPP. With this combination of LC and spacer, it should be able to obtain up to 6 topological charges for 0.6328μm He-Ne laser beam.

2.4 Phase shift of liquid crystal spiral phase plates

The function of a spiral phase plate is to impress helical phase shift on the light beam passing through it. A 3D diagram of a spiral phase plate made of silica is shown in Fig. 2.5. It is composed of many slices, the thickness of the slices are increased piecewise in the same step height when starting from the thinnest slice and circling clockwise around the center. Generally, for a spiral phase plate with topological charge of l and total slices number of s, the phase shift $R(n)$ of No. n slice can be expressed as:

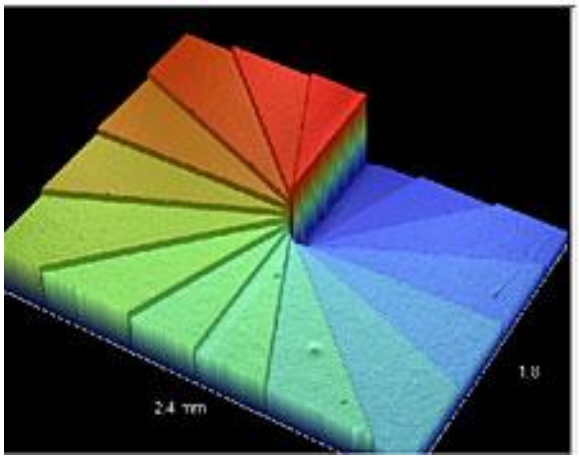

Fig. 2.5 Schematic illumination of a spiral phase plate [37].

$$R(n) = \frac{2\pi l(n-1)}{s-1} \tag{2.6}$$

The phase shift is linearly increased with the increasing of slice number.

However, as shown in Fig. 2.6, since the phase shift of a LC retarder responds nonlinearly to the driving voltage, to obtain linearly increased phase shift across the slices, the voltage applied to each slice can not be linearly increased. This aspect should be taken into consideration in the design of LC SPP. It should be mentioned that the curve shown in Fig. 2.6 was measured by the method that will be discussed in detail in chapter 4, and the LC material used is MLC-15800-000 from Merck.

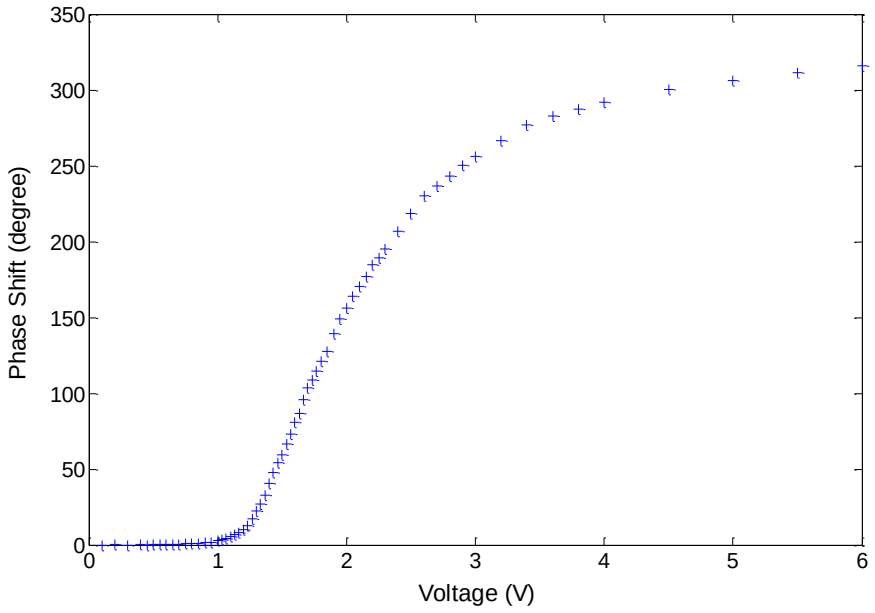

Fig. 2.6 The curve of phase shift versus applied voltage of a typical LC retarder.

Chapter 3 Structures and characterizations of three types of LC spiral phase plates fabricated

3.1 Structures of the three types of LC spiral phase plates (SPPs) fabricated

Three types of LC SPP have been fabricated. They were actually designed and fabricated one by one in time sequence, and each type is to overcome the limitations of former type. The structures of the three types of LC SPP are described in follows.

3.1.1 Structure of the first type LC SPP

Fig. 3.1 (a) and (b) show the diagram of the mask for ITO lithography and the photo of the device fabricated, respectively.

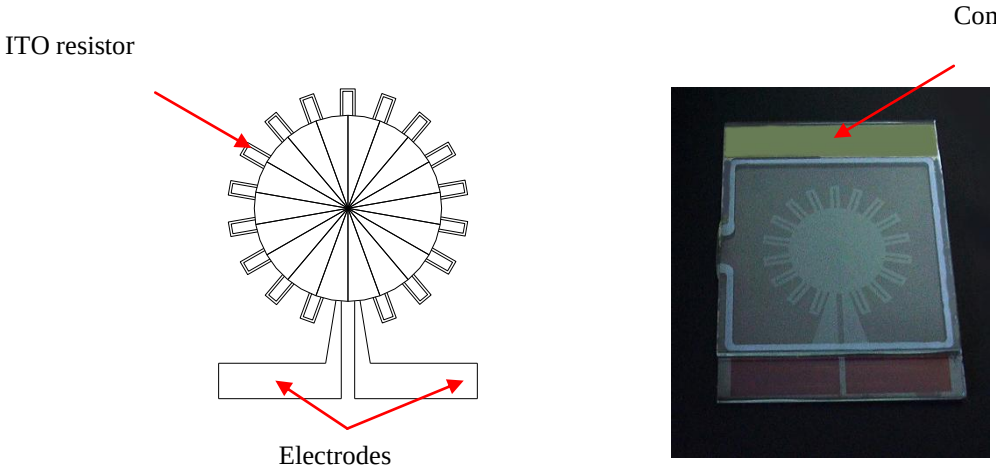

(a) (b)

Fig. 3.1 (a) Diagram of mask for the first type of LC SPP; (b) Photo of the first type LC SPP device fabricated.

Table 3-1 tabulates the parameters of the first type LC SPP. All the ITO resistors connecting adjacent slices are the same length and have the same resistance, they act as voltage dividers. Thus the voltage applied to the two electrodes is evenly distributed across the slices.

Table 3-1 Parameters of the first type of LC SPP.

Total slices number	18
Gap between adjacent slices	25 μm
Δn of LC (MLC-15800-100)	0.16
Cell gap	7 μm and 20 μm

The gap between adjacent slices is 25 μm. Since the gap is large, the economic plastic film mask was employed for the lithography.

Comparing with the LC SPP published in reference 26, the ITO resistors designed in the first type LC SPP help to distribute the voltage to each slice more evenly, and the thicker cell gap enables the generation of optical vortices with higher topological charges.

A voltage source which can generate square wave of 150~500Hz and amplitude from 0 to 10 V is used to drive this LC SPP. The two terminals of the output of the voltage source are connected to the two electrodes indicated in Fig. 3.1(a). The common electrode, which is the blank ITO film on the opposite substrate and indicated in Fig. 3.1(b), is connected to ground.

3.1.2 Structure of the second type LC SPP

One of the improvements of this version comparing with the former one is to compensate the nonlinear response of the retardation versus driving voltage. In the first type of LC SPP, the phase shift is not linearly increased slice by slice. To solve this problem, the ITO resistors connecting adjacent slices were designed with the same width but different lengths, so as to obtain the linearly increased phase shift at each slice for a certain topological charge. The resistances of these ITO resistors are determined by the curve of phase shift versus driving voltage. Fig. 3.2 (a) shows the mask designed for ITO lithography. Fig. 3.2 (b) shows the photo of the device fabricated.

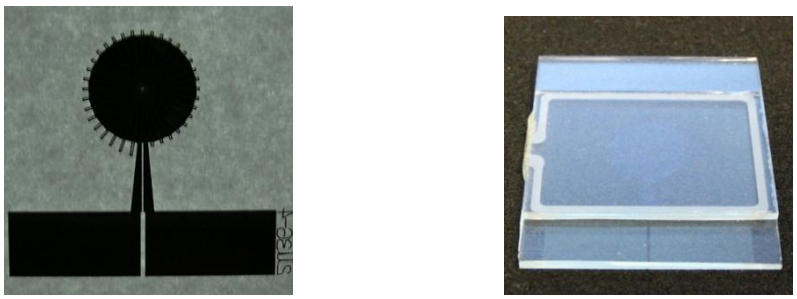

(a) (b)

Fig. 3.2 (a) Photolithography mask for the second type of LC SPP; (b) Photography of the second type LC SPP device fabricated.

Besides, the 25 μm gap between adjacent slices of the first type LC SPP is too large, it causes considerable energy loss due to the scattering. (For detail, see section 3.7) Thus, for

the second type LC SPP, the gap is reduced to 5 μm. Since this dimension is beyond the resolution of the plastic film mask, a Chrome mask was used for the ITO lithography.

Moreover, it has been found that large slice number will improve the quality of the optical vortex generated (For detail, see section 3.5). Therefore, in the second type LC SPP, the total slice number is increased to 36. The parameters of the second type of LC SPP are shown in Table 3-2. The driving for this type of LC SPP is the same as that for the first type LC SPP.

Table 3-2 Parameters of the second type of LC SPP.

Total slices number	36
Gap between adjacent slices	5 μm
Δn of LC (MLC-15800-100)	0.16
Cell gap	18 μm

3.1.3 Structure of the third type LC SPP

The second type LC SPP can only generate optical vortices with a certain topological charge for a certain wavelength. To overcome this limitation, the third type LC SPP is designed and fabricated.

So long as the voltage applied to each slice can be controlled individually, it is possible to realize a LC SPP that can be used for any visible wavelength and to generate optical vortices with different topological charge. However, to control the voltage applied to each slice individually, each slice has to be connected to an individual voltage output,

and it is too much even for a multi-channel analogue voltage output card. In practice, we used a special designed ITO pattern such that one 16 channel voltage output card is sufficient to drive the LC SPP with 46 slices.

By dividing the whole dynamic region of the phase shift versus voltage curve evenly, the phase shift can be approximated to be linearly dependent on driving voltage in each region. Therefore, the linearly distributed voltage across slices can be applied in each region, which can be realized by connecting adjacent slices with ITO resistors of the same length, to form a linear voltage divider. Similar to the previous types of LC SPP, these resistors can be fabricated by patterning ITO layer into long narrow wires. By doing so, the 15 linear retardation regions with 46 slices can be driven by only one multi-channel output card with 16 channels.

Special attentions were paid to the resistance values of ITO resistors. The resistance value should be much bigger than that of the wires connecting slices to terminal, so as to minimize voltage drop on the connecting wire. Because of this, the ITO pattern connecting the adjacent slice should be designed long and narrow. As shown in Fig. 3.3, the width and the length of the wire of each ITO resistor is 20μm and 8mm, respectively, so the square number of ITO pattern is 200, the ITO glass used is about 100Ω/□, hence the resistor is about 20kΩ. On the other hand, the wires connecting slices to lead should be designed as thick as possible.

To facilitate the connection between the ITO electrode and voltage output card, the anisotropic conductive rubber (zebra rubber) was used to connect the ITO electrodes in the panel to a printed circuit board (PCB) which was connected to a 16-channel voltage output card installed in a computer.

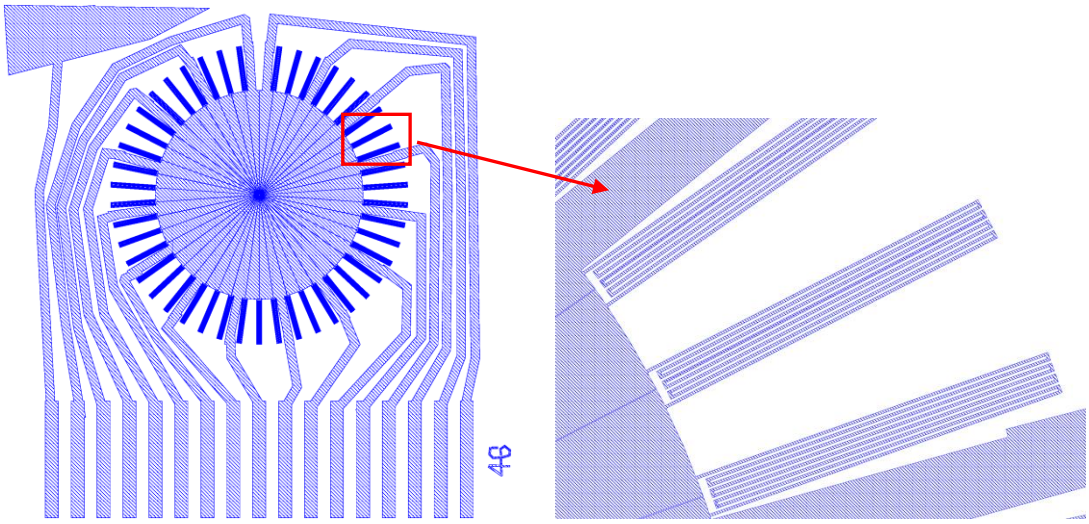

(a) (b)

Fig. 3.3 (a) ITO pattern of the third type LC SPP; (b) Close-up of the ITO wire resistor.

The voltage applied to each slice for generating optical vortices with certain topological charge is determined according to the phase shift versus driving voltage curve, the measurement of this curve will be introduced in chapter 4. The driving program is shown in Appendix A.

Fig. 3.4 (a) and (b) show the photographs of the third type of LC SPP cell and module, respectively. The common electrode on the blank ITO glass substrate is

transferred to the ITO patterned substrate through a dot of conductive carbon paste, which is shown in Fig. 3.4 (a), and then is connected through the most left electrode shown in Fig. 3.3 (a). The parameters of the third type LC SPP are shown in Table 3-3.

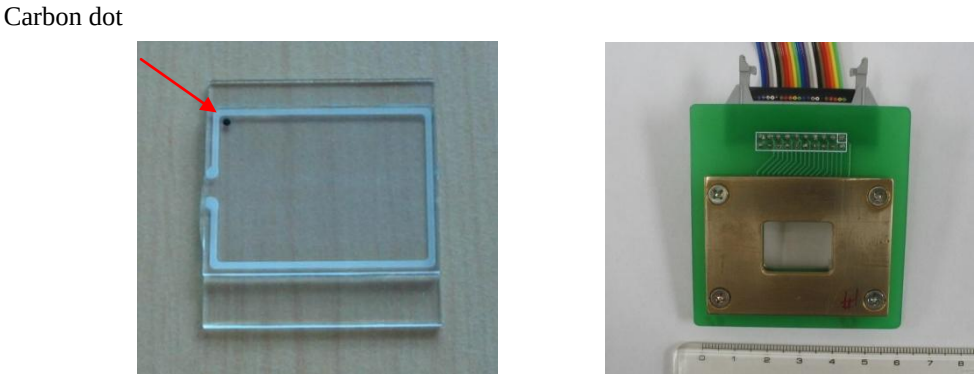

(a) (b)

Fig. 3.4 (a) Photograph of the third type LC SPP; (b) Photograph of the third type LC SPP module.

Table 3-3 Parameters of the third type LC SPP.

Total slices number	46
Gap between adjacent slices	5 μm
Δn of LC (E7)	0.225
Cell gap	18 μm

3.2 The interference patterns between optical vortices and their coherent Gaussian beams

The direct method to verify an optical vortex is to interfere it with a coherent Gaussian beam [38]. The experiment setup is actually a Mach-Zehnder interferometer, which is shown in Fig. 3.5. With a beam expander formed by two lenses (LENS1 and LENS2), the diameter of the laser is expanded from 0.9 mm to 7 mm. A 50% beam splitter, BS1, is used to split the laser into two beams: one of the beams directly passes through the LC spiral phase plate, and reflected by a mirror (M2) towards the beam splitter BS2; another beam is reflected by another mirror (M1) and goes towards the beam splitter BS2 as well. These two beams are recombined at beam splitter BS2, and their interference pattern is magnified by LENS3 and projected on a screen.

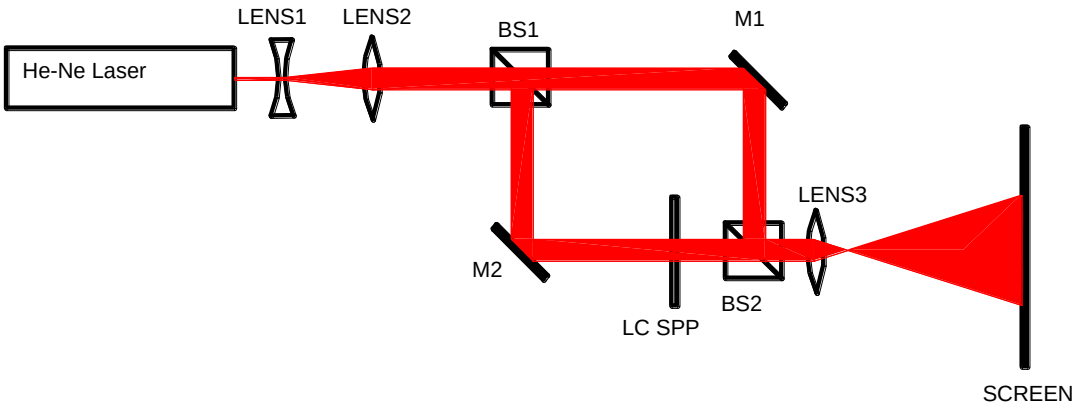

Fig. 3.5 The setup for verification of optical vortices.

3.2.1 Interference patterns generated by the first type LC SPP

Fig. 3.6 (a) and (b) show the interference patterns between optical vortices with topological charge 3 and topological charge 4 and slightly inclined coherent Gaussian beams, respectively. Fig. 3.6 (c) and (d) show the interference patterns between the optical vortices with topological charge 3 and topological charge 4 with coaxial coherent Gaussian beams, respectively. Fig. 3.6 (e), (f), (g) and (h) are corresponding simulation results. The experimental results are consistent with the simulations. Through the interference patterns, the topological charge number of the optical vortices can be ascertained [38].

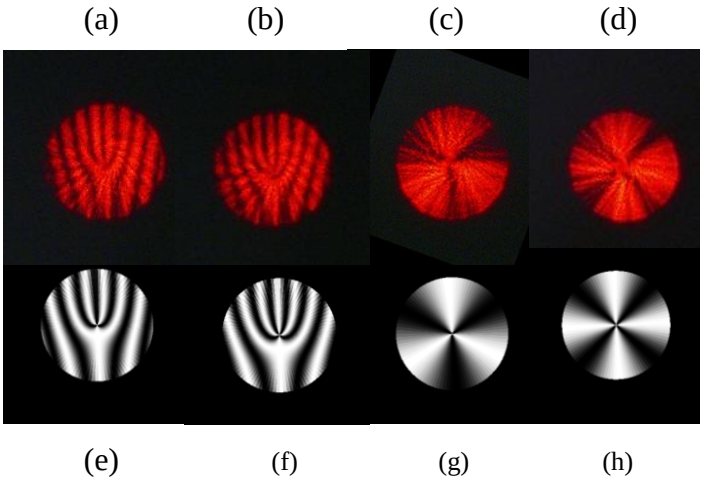

Fig. 3.6 The experimental and simulation interference patterns between optical vortices and their coherent Gaussian beams.

By rotating a glass plate inserted in one arm of the Mach-Zehnder interferometer, the rotation of the fan-like interference pattern was observed. The recorded interference patterns are shown in Fig. 3.7. Fig. 3.7 (a), (b), (c) and (d) correspond to four different

orientations of the glass slide. The bright spots in top left corner provide a reference to show the rotation of the vortex.

The rotating spiral interference pattern has been applied to rotate optically trapped microscopic particles by hologram method [39], but the power conversion efficiency is low.

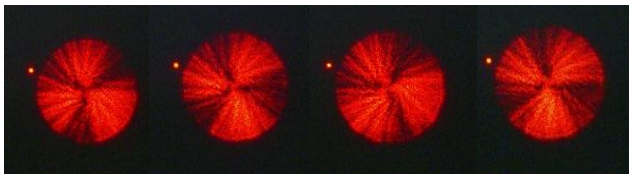

(a) (b) (c) (d)

Fig. 3.7 The rotating interference pattern generated by the optical vortex of topological charge 3 and a coaxial plane wave. The bright dots in the pictures are deliberately added as a reference to indicate the rotation.

3.2.2 Interference patterns generated by the second type LC SPP

The interference pattern of the optical vortex with topological charge 3 generated by the second type LC SPP is shown in Fig. 3.8. The quality of the interference pattern is significantly improved comparing with the first type LC SPP.

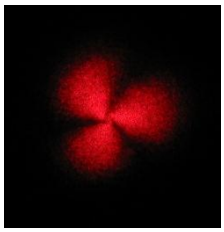

Fig. 3.8 The interference pattern of the optical vortex with topological charge 3 generated by the second type LC SPP.

3.2.3 Interference patterns generated by the third type LC SPP

By applying different voltages to the third type LC SPP, optical vortices with topological charges from 1 up to 6 were obtained. Figure 3.9 (a) shows the fork like interference patterns corresponding to optical vortices with different topological charges. A fork like interference pattern is formed when the two interference beams are at a small angle with each other. If the two beams are coaxial, the interference pattern will turn into a radial spokes pattern, which is shown in Fig. 3.9 (b).

By properly coding the driving program, the dynamic switching between optical vortices with different topological charge was observed [40]. However, due to the thick cell gap and high viscosity LC used, the switching between optical vortices with different topological charge took about one second.

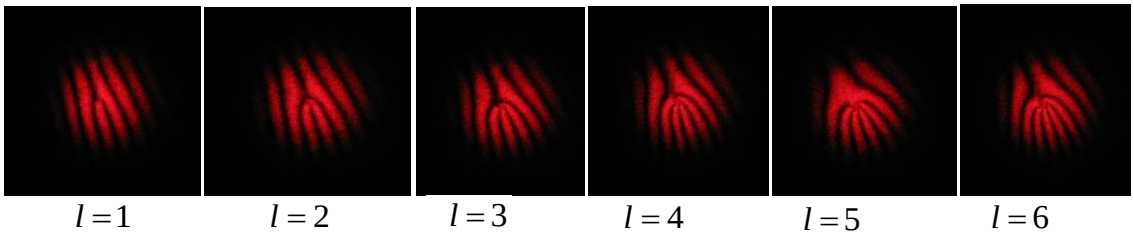

(a)

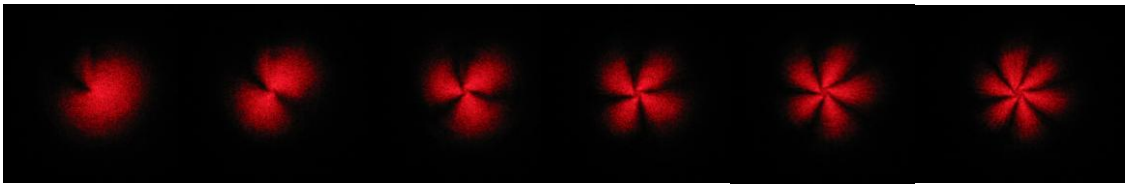

(b)

Fig. 3.9 Interference patterns of optical vortices with topological charge from 1 to 6 generated by the third type LC SPP. (a) Fork-like interference patterns; (b). Radial spokes interference patterns.

3.3 The Fraunhofer diffraction patterns of LC SPP

The apparatus shown in Fig. 3.10 is the setup for observing Fraunhofer diffraction patterns. LENS 3 and LENS 4 are convex lenses with long focus length (50cm), so as to generate the Fraunhofer diffraction. Fig. 3.11 shows the diffraction patterns observed with the first type LC SPP.

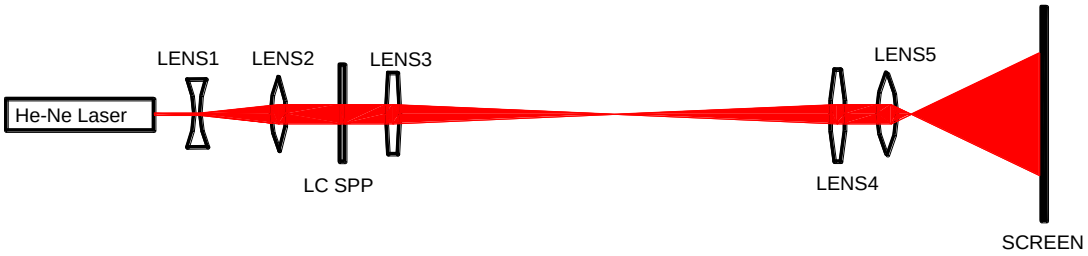

Fig. 3.10 Setup for observing Fraunhofer diffraction patterns of a Gaussian beam passing through the LC SPP.

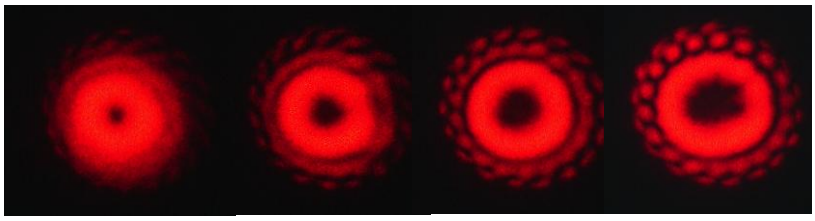

Fig. 3.11 Optical vortices with different topological charge generated by the first type LC SPP.

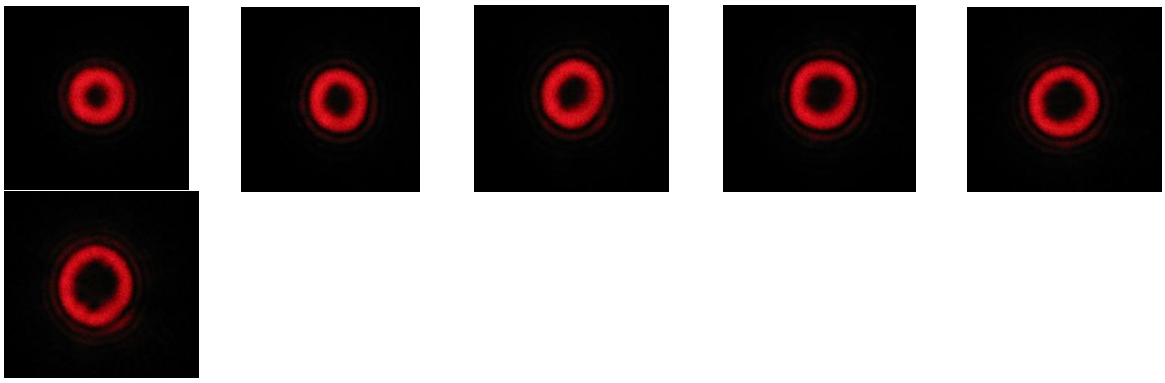

Fig. 3.12 Fraunhofer diffraction patterns of Gaussian beam passing through SPP of topological charge number from 1 to 6.

The Fraunhofer diffraction patterns of Gaussian beams passing through the third type LC SPP are illustrated in Fig. 3.12. All these images were taken at the same distance. The improvement of the Fraunhofer diffraction patterns generated by the third type LC SPP is significant.

3.4 Generation of optical vortices with high topological charge by stacking LC SPP [41]

Generation of optical vortices with high topographic charge can be realized by stacking multiple LC spiral phase plates. The modulation process of LC spiral phase plate stacks can be understood qualitatively as follows. When a plane laser beam with field U_0 passes though a $2\pi l$ spiral phase plate, the emerging beam becomes

$$U = U_0 \exp(il\theta) \tag{3.1}$$

Where l is the number of 2π phase change on any closed circle around the beam axis, it is the azimuthal index of the emerging doughnut beam, θ is the polar coordinate in the plane perpendicular to the beam propagation direction. In Eq. (2.2), the term $\exp(il\theta)$, is introduced by the $2\pi l$ spiral phase plate. By stacking n layers of LC spiral phase plates with $2\pi l_1$, $2\pi l_2$, ……, $2\pi l_n$ spiral phase changes respectively, the emerging ray becomes

$$U = U_0 \exp(i\ l_1\theta)\exp(il_2\theta)\cdots\cdots\exp(il_n\theta) = U_0 \exp(i\theta\sum_i l_i) \tag{3.2}$$

where *i* ranges from 1 to *n*. From Eq. (3.2), it can be seen that the azimuthal index of the emerging beam is the sum of all the azimuthal indices of each individual spiral phase plates.

The stacking of LC spiral phase plates is done in the way that the rubbing directions of all the LC cells stacked are parallel (Fig. 3.13). Ideally, the LC spiral phase plates should be glued with index-matched epoxy to reduce reflection loss. In this experiment, they are just loosely positioned together. The polarization direction of the input laser beam should be parallel to this rubbing direction as well.

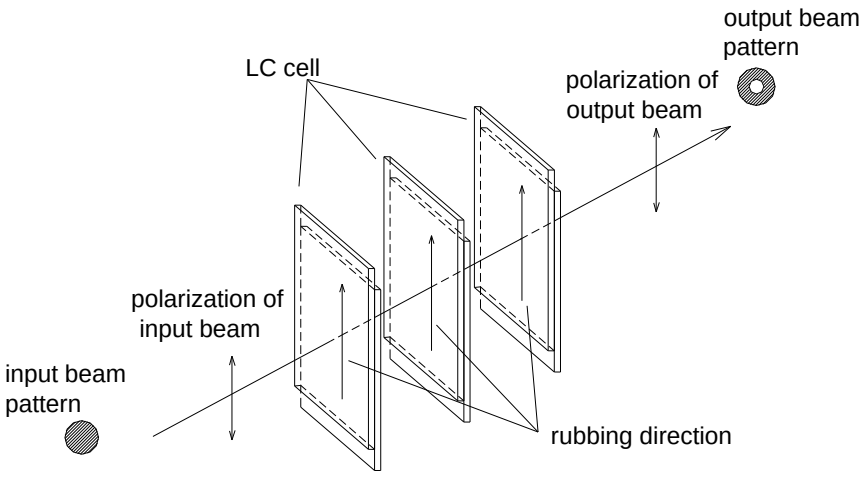

Fig. 3.13 Illustration showing the stacking of the LC spiral phase plates. The rubbing directions of all LC SPPs should be parallel and the polarization of the input laser beam should be parallel to the rubbing direction as well.

Fig. 3.14 shows the Optical vortices with topological charges from 5 to 8 (l = 5, 6, 7 and 8) generated by stacking two first type LC SPP. It can be observed that the ring of the optical vortex becomes discrete with the increasing of the topological charge, this phenomenon will be further studied in section 3.6.1.

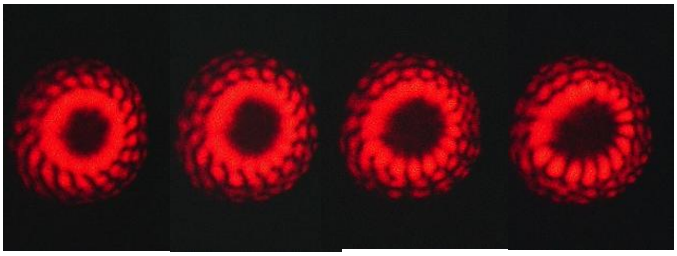

l = 5 l = 6 l = 7 l = 8

Fig. 3.14 Optical vortices with topological charges from 5 to 8 (l = 5, 6, 7 and 8) generated by stacking two first type LC SPPs.

3.5 Relationship between beam purity and slice number

Multi-level SPP, comprising limited number of phase slices, is using discrete phase steps to imitate a continuous phase ramp. Apparently, it is an approximation. Using Fourier method, the relationship between beam purity and the total slice number can be shown as follows.

Denoting s as the total slice number of SPP, ϕ as the azimuthal angle, then the effect of SPP with topological charge m can be represented by:

$$f(\phi) = e^{i \cdot \mathrm{Int}(\frac{s\phi}{2\pi}) \cdot \frac{2m\pi}{s}} \tag{3.3}$$

where "$\mathrm{Int}(\frac{s\phi}{2\pi})$" refers to the maximum integer less than $\frac{s\phi}{2\pi}$, and $0 \le \phi \le 2\pi$. According to the Fourier transformation theory, $f(\phi)$ can be written as $f(\phi) = \sum_{n=-\infty}^{+\infty} c_n \exp(jn\phi)$, where *n* is an integer, $-\infty < n < +\infty$, and

$$c_n = \frac{1}{2\pi}\int_0^{2\pi} f(\phi)\exp(-jn\phi)d\phi = \frac{1}{2\pi}\int_0^{2\pi} e^{i \cdot \mathrm{Int}(\frac{s\phi}{2\pi}) \cdot \frac{2m\pi}{s}} \exp(-jn\phi)d\phi \tag{3.4}$$

Assuming a laser beam with an electric field of $F(\rho, z)$ incident on the SPP, the electric field of the emerged beam immediately after the SPP can be written as

$$u(\rho, \phi, z) = F(\rho, z)\sum_{n=-\infty}^{+\infty} c_n \exp(jn\phi) \tag{3.5}$$

This is a combination of infinite Fourier components, each component represents an optical vortex with certain topological charge, c_n is the amplitude of the topological charge *n* component. For a SPP with topological charge *m*, only the component $c_m \exp(jm\phi)$ is desired, the others are unwanted. The percentage of all those unwanted components, *R*, can be written as

$$R = 1 - \left|c_m\right|^2 \tag{3.6}$$

Assuming R < 6% (Such a ratio should be good enough for most application, such as optical tweezers and cold atom guiding), from Eqs. 3.4 and 3.6, the minimum requirement

of the total slice number for a certain topological charge can be calculated. The calculation results are tabulated in Table 3-4.

Table 3-4 Minimum slice number of a SPP and the corresponding topological charge of a vortex beam generated with over 94% purity.

SPP's topological charge	1	2	3	4	5	6	7	8
Minimum Slice number	8	15	22	30	37	44	52	59

3.6 The phenomena of discreteness and distortion of optical vortices

3.6.1 Discreteness of optical vortices

The phenomena, that the ring of the optical vortex becomes discrete with the increasing of the topological charge as shown in Fig. 3.14, is actually caused by the limited total slice number. This conclusion is sustained by the simulation results.

The number of the discrete parts of the optical vortex shown in Fig. 3.14 is 18, which is exactly equal to the total slice number of the LC SPP. This fact implies the relationship between the discreteness phenomenon and the total slice number of LC SPP.

Simulations taking into consideration of the limited total slice number (18) were carried out, and the results are shown in the lower row of Fig. 3.15. The experiment results in Fig. 3.14 are shown in the upper row of Fig. 3.15 for comparison. It can be seen that the simulation results also show the discreteness trend with the increasing of the topological charge, which is consistent with the experiment results.

In conclusion, both experiment and simulation results show that: the ring of an optical vortex with high topological charge generated by a SPP with small total slice number is

discrete, and the number of the separated parts is equal to the total slice number. This mechanism may find application in optical ratchets [42].

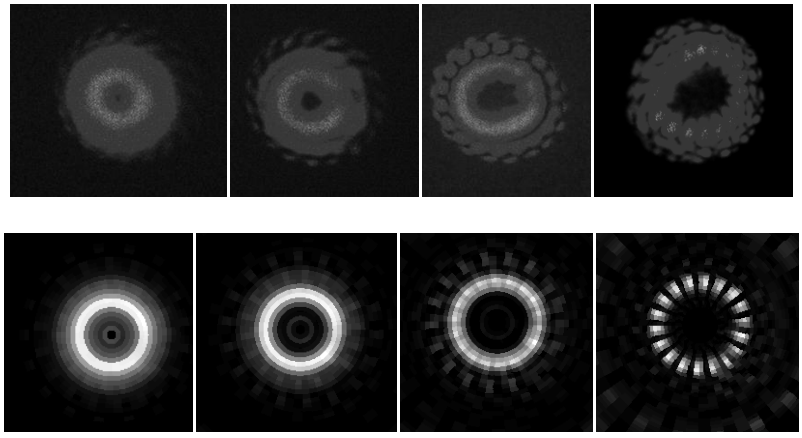

l=1 *l*=2 *l*=4 *l*=8

Fig. 3.15 Fraunhofer diffraction patterns generated from the first type LC SPP, upper row are experiment results, lower row are simulation results.

3.6.2 Distortion of central dark region

If the phase shift of the SPP is not linearly dependent on the azimuthal angle, the central dark region will be distorted. This conclusion has been theoretically simulated and experimentally verified.

Fig. 3.16 shows the phase shift versus driving voltage curve of the third type LC SPP. If a linearly increased voltage is applied to the SPP, and make it work in the retardation region between 2.6μm and 3.8656μm, it will be a SPP with topological charge 2, and since

it is working in the nonlinear region of the curve, the phase shift is not linearly dependent on the azimuthal angle.

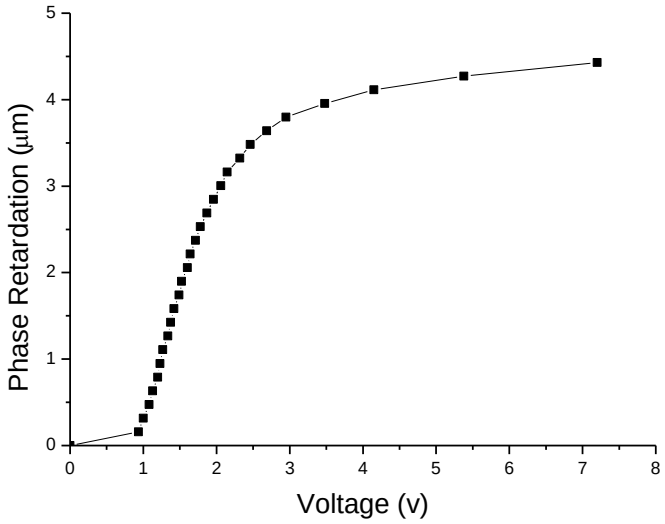

Fig. 3.16 Phase shift versus driving voltage of the third type LC SPP.

The Fraunhofer diffraction pattern of such a SPP has been investigated. The experimental result is shown in Fig. 3.17 (a). On the other hand, Fig. 3.17 (b) shows the simulation result of such a SPP.

Both experimental result and simulation result show clearly that the SPP with nonlinear phase shift versus azimuthal angle results a distorted optical vortex pattern, and the central dark region is split into two for the optical vortex with the topological charge of 2. Because of this, this sort of SPP is not suitable for most applications such as optical tweezers, cool atom guiding, edge contrast enhancement in microscopy and optical vortex coronagraph etc. Therefore, the distortion should be avoided. It is worth mentioning that the splitting of the central dark region for high order optical vortices have also reported by

I. V. Basistiy *et al*., however in that case it was due to the existence of a background Gaussian beam [43].

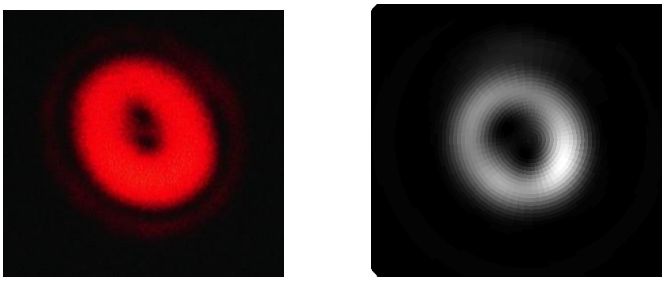

(a) (b)

Fig. 3.17 Both the experimental result (a) and the simulation result (b) show the existence of the splitting of central dark region for a second order optical vortex generated by a LC SPP with nonlinear dependence of phase shift on the azimuthal angle.

3.7 Conversion efficiency of LC SPP

In reference 26, the conversion efficiency of LC SPP is simply asserted as 100% without any experimental sustention. To experimentally verify the conversion efficiency of LC SPP, the conversion efficiency of the first type LC SPP was measured. The results are tabulated in Table 3-5. The input power is 3.2 mw from a 632.8 nm polarized He-Ne laser. Transparency is the percentage ratio of the output power without voltage applied over the input laser power. The conversion efficiency is the percentage ratio of the output power with voltage applied over the output power without voltage applied. The power was measured in far field.

It can be seen in Table 3-5 that the transparency of one 7 μm cell and one 18 μm cell are 89.7% and 89.1% respectively. The loss of the dynamic state (with voltage applied) is mainly caused by the scattering of LC molecules in the gaps between ITO slices. The loss of the static state (no voltage) is mainly due to the interface reflections between the air-glass and glass-LC. The transparency of a single cell is not sensitive to the LC cell gap. So does the conversion efficiency, which is 79.4% and 79.6% for one 7 μm cell and one 18 μm cell respectively. Moreover, this conversion efficiency is independent of the topological charge number generated by a single LC plate.

Table 3-5. The Gaussian beam to optical vortices conversion efficiency of single and stacked first type LC SPP. The total input power is 3.20 mW from a He-Ne laser operating at 632.8 nm. Transparency is the percentage ratio of the output power without (w/o) voltage applied over the input laser power. The conversion efficiency is the percentage ratio of the output power with (w) voltage applied over the output power without voltage applied. The power is measured in far field.

	1 plate (7 μm)	2 plates stacked (7 μm)	3 plates stacked (7 μm)	1 plate (18 μm)	2 plates stacked (18 μm)
Output power w/o voltage applied	2.87 mW	2.52 mW	2.26 mW	2.85 mW	2.55 mW
Output power w voltage applied	2.28 mW (Charge 1)	1.70 mW (Charge 2)	1.22 mW (Charge 3)	2.27 mW (Charge 4)	1.73 mW (Charge 8)
Transparency	89.7%	78.8%	70.6%	89.1%	79.7%

Conversion Efficiency	79.4%	67.5%	54.2%	79.6%	67.8%

Stacking more LC spiral phase plates, a slight steady decrease in transparency and conversion efficiency is observed. By stacking two 7 μm cells and three 7 μm cells, correspondingly, the transparency reduces to 78.8% and 70.6%, the conversion efficiency reduces to 67.5% and 54.2%. By stacking two 18 μm cells to generate a optical vortex with topological charge 8, the conversion efficiency is 67.8%, which is almost the same as that by stacking two 7 μm cells to generate a optical vortex with topological charge 2. So the transparency and conversion efficiency is dependent on the number of LC cells stacked, but not the topological charge number of the optical vortices.

It is worth mentioning that, the reduction in transparency could be reduced with index-matched epoxy to glue LC cells and anti-reflection coating at the air-glass interface.

(a) (b) (c)

Fig.3.18. (a) The laser beam impinged on the gap between two adjacent slices of the first type LC SPP (the diameter of the laser beam is about 1.5mm). (b) Pattern of the diffraction beam without any voltage applied to the LC SPP. (b) Pattern of the diffraction beam with a voltage above threshold voltage applied to the LC SPP.

If the liquid crystal molecules align inhomogeneously in the gap between slices, light beam will be scattered, and this results in the loss in dynamic state and the degradation of conversion efficiency. This conclusion is supported by experiments.

As shown in Fig. 3.18 (a), a laser beam is impinging on the gap between two adjacent slices of the first type LC SPP. The pattern of the diffraction beam is shown in Fig. 3.18 (b) when there is no voltage applied to the LC SPP. When the voltage above the threshold is applied to the LC SPP, the pattern of the diffraction beam is shown in Fig. 3.18 (c), which clearly shows that the beam is seriously scattered comparing with the former case.

Table 3-6. The Gaussian beam to optical vortices conversion efficiency of the second and third type LC SPP. The total input power is 3.20 mW from a He-Ne laser operating at 632.8 nm. Transparency is the percentage ratio of the output power without (w/o) voltage applied over the input laser power. The conversion efficiency is the percentage ratio of the output power with (w) voltage applied over the output power without voltage applied. The powers were measured in far field.

	The second type LC SPP	The third type LC SPP
Output power without voltage applied	2.87 mW	2.86 mW
Output power with voltage applied	2.45 mW (Topological charge 1)	2.33 mW (Topological charge 4)

Transparency	89.5%	89.3%
Conversion Efficiency	92.3%	91.4%

Due to this fact, the conversion efficiency of the first type LC SPP can be improved by reducing the gaps between adjacent slices. Table 3-6 shows the experimental results of conversion efficiency of the second type and the third type LC SPP (5μm cell gap), which shows a improvement comparing with the first type LC SPP.

Chapter 4 Measuring phase shift versus driving voltage of LC SPP

As shown in previous chapter, the voltage applied to the third type LC SPP for generation of different topological charge optical vortices and the length of the ITO wire resistor used in the second type LC SPP, can only be determined based on the phase shift versus voltage curve of the LC SPP. In this chapter, the measurement system developed for the measurement of the phase shift versus driving voltage of LC SPP is described in detail.

4.1 Measurement using the conventional Michelson interferometer

4.1.1 Introduction to the methodology

Fig. 4.1 shows an apparatus with a Michelson interferometer configuration, which was initially used for the measurement of the phase shift versus driving voltage of LC SPP.

To start the measurement, we need to adjust the directions of the two mirrors so as to obtain 3~5 parallel interference lines on the screen. With the changing of the driving voltage, the phase shift of the LC cell changes, and the interference lines move. If the bright lines have moved a distance of half pitch of the equidistant fringe, corresponding

phase shift of LC cell should be $\lambda_0 / 4$ =0.1582 μm, where λ_0 is the wavelength of the He-Ne laser, and $\lambda_0 = 0.6328$ nm. By recording the driving voltage for every half-pitch movement of the equidistant fringe, the curve of the phase shift versus driving voltage of the LC SPP can be obtained, which is shown in Fig. 3.16.

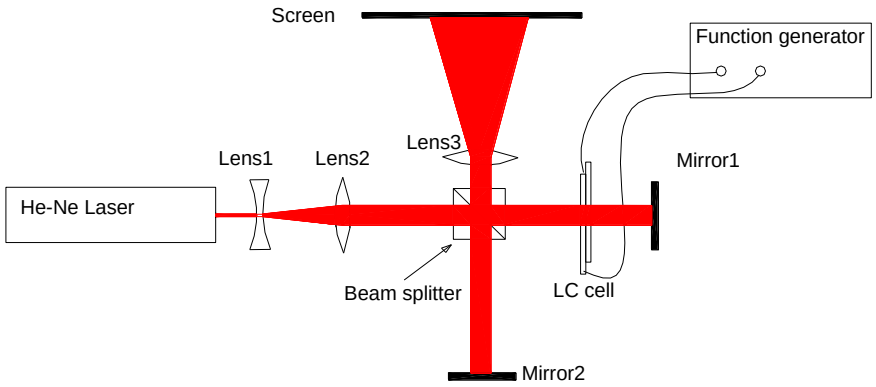

Fig. 4.1 The apparatus of conventional Michelson interferometer for measuring phase shift versus driving voltage of LC SPP.

The data obtained by this method are inevitably discrete (Fig. 4.2). By curve fitting, a polynomial formula can be obtained to approximate the function of phase shift versus any driving voltage.

4.1.2 Problems existed

1. Low efficiency

As described in the previous section, the measurement is manually performed, and the efficiency is low. Normally, it takes about 15 minutes to measure one LC cell.

2. Low accuracy

Firstly, since the position of the equidistant fringe lines is determined by human eye, the accuracy is low (human errors).

Secondly, since the process last about 15 minutes, the drift of the equidistant fringe is considerable during this period. The drift is mainly caused by change of temperature. For example, the coefficient of linear thermal expansion of steel is $1.3\times10^{-5}/k$ [44]. Assuming the length of the arm of Michelson interferometer is 10 cm, if there is a temperature difference of 0.01 ^{o} between two arms of the Michelson interferometer, there is a length difference of 0.013 μm between the two arms, which corresponds to a phase shift of 14.8 ^{o} for a 632.8 nm wavelength beam. According to the experiment result, the infrared radiated from the person carrying out the measurement is more significant than the temperature fluctuation in the air-conditioned room. The longer it takes for the measurement, the larger the drift caused by the temperature change.

4.2 Measurement using the improved Michelson interferometer

4.2.1 Introduction

As shown in previous section, there are some problems existing in the measurement of phase shift versus driving voltage of LC SPP using conventional Michelson interferometer. To solve these problems, an automatic measurement system was set up; it was made up of existing items in our laboratory, including oscilloscope, function generator, computer, and a self-setup Michelson interferometer with a linear photo detector array (LPDA) as the detector, working seamlessly like a virtual instrument

through a program developed. With this system, the measurement of the phase shift-voltage curve (defined by 30 data) of a LC SPP can be completed within one minute; this greatly reduced the measurement error caused by the drift of the system. Moreover, it has been proved experimentally that the measurement uncertainty (standard deviation) as good as 0.1° can be obtained with this system.

Though the major motivation of this work is to achieve accurate and efficient measurements of phase shift versus driving voltage of LC SPP, It also provides a new and cost effective measurement method in our laboratory, which may meet other phase shift measurement requirements except for LC SPP. For instance, for the phase shift versus driving voltage measurement of the liquid crystal on silicon (LCoS) spatial phase modulators, which have found applications in wave-front correction or wave front shaping [45~49], and also for the measurement of polymer dispersed liquid crystal (PDLC) device.

Besides, we applied a new methodology for extracting phase information from equidistant fringes, different from those used by other researchers. Previously several data processing methods for extracting phase information from equidistant fringe have been reported, such as, the Fourier transform method [63, 64], peak position method [65] and using the image matching algorithm [66] etc. In our measurement system, a trough position method is employed for extracting phase information from the equidistant fringe obtained from LPDA.

The technical details of this phase shift measurement system employing the trough position method will be presented in following sections, including ① the theoretical substantiation about the trough position method; ② the detailed description of the

measurement system employing this method; ③ the observation and discussion of thermal drift and non-thermal drift; ④ the experimental study of the system accuracy in the measurement of displacement of piezoelectric actuated mirror (PZT mirror); ⑤ the experimental results in the measurement of displacement of PZT mirror, phase shift versus driving voltage of anti-parallel aligned nematic liquid crystal and polymer-dispersed liquid crystal (PDLC) cells.

4.2.2 Trough position method

The working principle of the measurement of phase shift using the equidistant fringe, which is obtained through a Michelson interferometer with LPDA detector, has been described in detail in reference 65. Here we will focus on a new data processing method, i.e., the so called trough position method.

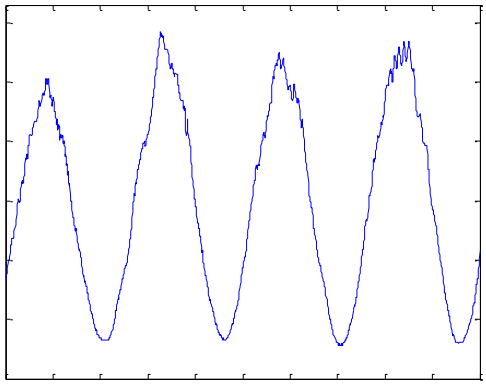

Fig. 4.2 A typical equidistant fringe curve obtained from a real system.

A typical equidistant fringe curve obtained from a real system is shown in Fig. 4.2. We can see that the bottom of the equidistant curve has less distortion than the top part of the curve. In fact, this phenomenon is intrinsic.

In a real Michelson interferometer measurement system, the reference beam (R beam) and the object beam (O beam) are unavoidably mixed with some noise beams due to the reflections from the surface of optical components. Assuming $A(x)\exp(i\omega t)$ and $B(x)\exp[i(\omega t + fx)]$ represent the R beam and O beam, respectively, where A and B are functions of the coordinate value x in the direction of the linear photo detector array, f represents the spatial frequency of O beam. Similarly, let $C(x)\exp[i(\omega t + \xi x) + \Delta]$ represents the noise beam, where ξ denotes spatial frequency, Δ denotes the initial phase, then the intensity of the synthesized beam can be written as

$$\begin{aligned} I(x) &= A^2 + B^2 + C^2 + 2AB\cos(fx) \\ &\quad + 2AC\cos(\xi x + \Delta) + 2BC\cos[(\xi - f)x + \Delta] \end{aligned} \tag{4.1}$$

The minimum of R and O synthesized beam occurs when $x = (2n+1)\pi / f$, and the maximum occurs when $x = 2n\pi / f$, where n is an integer. The derivative of $I(x)$ at the position of $x = (2n+1)\pi / f$ and $x = 2n\pi / f$ can be obtained from Eq. (4.1) as

$$\begin{aligned} \left.\frac{dI}{dx}\right|_{x=(2n+1)\pi/f} &= 2(A'-B')(A-B) + 2CC' - 2BCf\sin(\xi x+\Delta) - 2C(A-B)\xi\sin(\xi x+\Delta) \\ &\quad + 2C(A'-B')\cos(\xi x+\Delta) + 2C'(A-B)\cos(\xi x+\Delta) \\ \left.\frac{dI}{dx}\right|_{x=2n\pi/f} &= 2(A'+B')(A+B) + 2CC' - 2AC\xi\sin(\xi x+\Delta) + 2BC(f-\xi)\sin(\xi x+\Delta) \\ &\quad + 2C(A'+B')\cos(\xi x+\Delta) + 2C'(A+B)\cos(\xi x+\Delta) \end{aligned} \tag{4.2}$$

Since $A \approx B$, and C is the amplitude of noise beam, so both $(A-B)$ and C are small. Since A, B and C are slow changing functions, thus A', B' and C' are all small. Denoting these small value items as δ, we have

$$\begin{aligned}\left.\frac{dI}{dx}\right|_{x=(2n+1)\pi/f} &= 2\delta^2 + 2\delta^2 - 2\delta Bf\sin(\xi x+\Delta) - 2\delta^2\xi\sin(\xi x+\Delta) \\ &\quad + 2\delta^2\cos(\xi x+\Delta) + 2\delta^2\cos(\xi x+\Delta) \\ \left.\frac{dI}{dx}\right|_{x=2n\pi/f} &= 2\delta(A+B) + 2\delta^2 - 2\delta A\xi\sin(\xi x+\Delta) + 2\delta B(f-\xi)\sin(\xi x+\Delta) \\ &\quad + 2\delta^2\cos(\xi x+\Delta) + 2\delta(A+B)\cos(\xi x+\Delta)\end{aligned} \tag{4.3}$$

Comparing the right hand sides of above two equations, it can be found that $\left|\left.\frac{dI}{dx}\right|_{x=(2n+1)\pi/f}\right| << \left|\left.\frac{dI}{dx}\right|_{x=2n\pi/f}\right|$. This means using minimum point of the fringe curve to represent the anti-phase point of R and O beams is a better approximation than using maximum point of the curve to represent the in-phase point of R and O beams.

Intuitively, Fig. 4.3 shows a simulation to illustrate this point. In the simulation, the intensity of the noise beam C^2 is assumed to be 0.5% of A^2 and B^2 , and f is 3 mm^{-1}, ξ is 10 mm^{-1}. $\Delta = \frac{1}{4}\pi$ and $\Delta = \pi$ are used in Fig. 4.3 (a) and (b), respectively. The red dashed lines show the curve without the noise beam, and the blue solid lines show the curve including the noise beam. It can be seen clearly that there is only a small discrepancy between the blue and red curve at the minimum position, while there is considerable large discrepancy at the maximum position.

Therefore, it is substantiated that the top part of the fringe curve is much more distorted than the bottom part in a real system. In our trough method, only the part near

the trough position of the equidistant fringe curve is used for extracting the phase information.

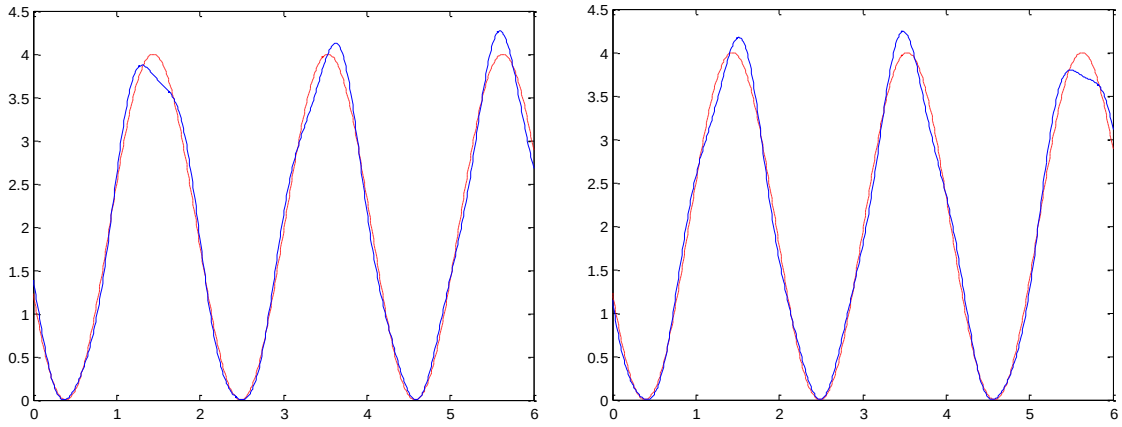

(a) (b)

Fig. 4.3 Simulation results of the synthesized waveform of R, O and noise beams. Here the noise beam is assumed to be 0.5% of the R, O beam in intensity. Red dashed lines are the synthesized waveforms without the noise beam; blue solid lines are the synthesized waveforms with the noise beam. (a) $\Delta = \frac{1}{4}\pi$, (b) $\Delta = \pi$, where Δ represents the initial phase of noise beam.

4.2.3 Experiment setup and methodology of data processing

The schematic diagram and photo of the experiment setup are shown in Fig. 4.4 (a) and (b), respectively. The laser used in the system is a 500:1 linearly polarized He-Ne laser from Newport co. with output power of 4mW, operating at 632.8nm wavelength. The magnification of the objective is 40; the pin hole is 25 μm in diameter. Lens1 is a flat-

concave lens with antireflection coating and a focus length of 20 cm. The broadband non-polarizing beamsplitting cube (model BS016 from Thorlab) is coated with antireflection layer.

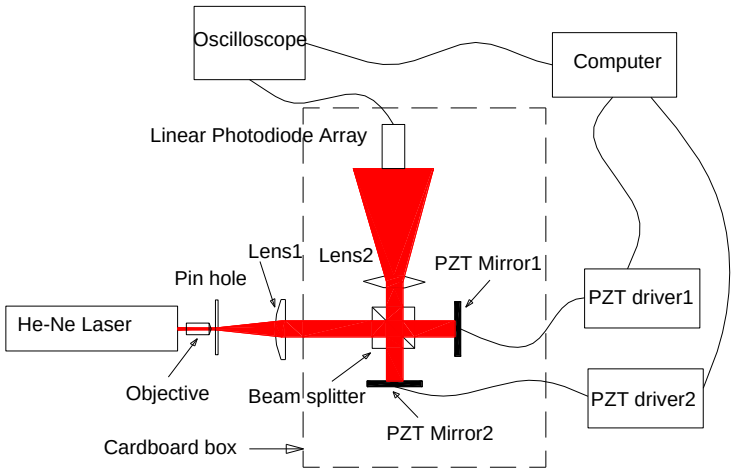

(a)

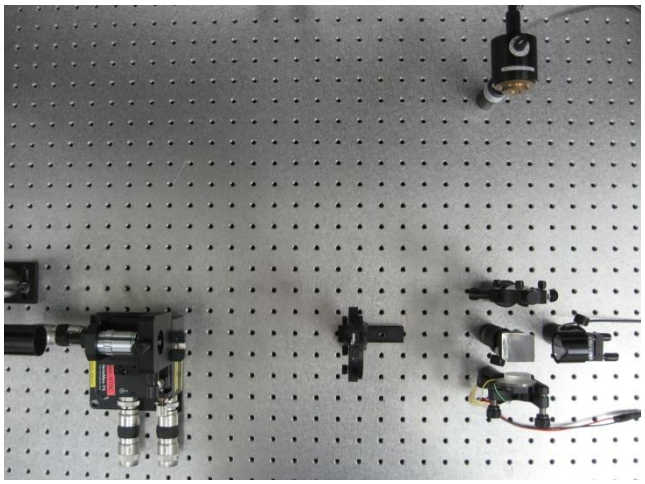

(b)

Fig. 4.4 (a) Diagram of the experiment setup. (b) Photo of the experiment setup.

The mirrors are broadband metallic mirror with λ/10 surface flatness (model 10D20 from Newport). One of the mirrors is actuated by a PZT from Newport (model FK-18515), which is driven by Agt33250A function generator (from Agilent co.). Another mirror is actuated by another PZT, which is driven by a voltage amplifier from Piezosystem Jena (Model NV40/3S).

Lens 2 is a concave lens with a focus length of 5 cm without antireflection coating. The LPDA have 1000 pixels; with a pitch of 7 μm. The scanning frequency of the LPDA is 362.3 Hz. The amplitude of the fringe signal is around 790 mV. The signal from LPDA is connected to Agt54641A oscilloscope (product of Agilent co.), which can work in average mode, i.e., averaging a number of waveforms acquired in sequence. The waveform data in the oscilloscope is then acquired by the computer through a GPIB port (NI USB GPIB).

The system was mounted on an optical table inside a 10,000 class clean room. During measurement, the air conditioner was shut down to reduce the vibration caused by air flow, and the interference parts (indicated with dashed line in Fig. 3(a)) were covered by a cardboard box.

The structure of the setup is similar to that used in reference 65. The only difference is the additional lens2 in our system, which is for magnifying the laser beam. Since laser beam possesses a Gaussian intensity profile and a spherical wavefront, lens2 ensures that only the central part of the laser beam, which is nearer to a plane wave, is acquired. It improves the uniformity of the pitches of the interference fringe shining on the LPDA and the intensity distribution.

The software for the measurement system is composed of two parts. The first part written in Visual Basic is for operation control, including the setting of parameters of oscilloscope, PZT driving signal generation and waveform data acquisition. As an example, the source code of this part for the measurement of Fig. 4.9 (c) is shown in Appendix B (a). The second part written in Matlab is dedicated to data processing for extracting the phase shift data, as an example, the source code of this part for the measurement of Fig. 4.9 (c) is shown in Appendix B (b).

The trough position method is applied in this system. The oscilloscope is set to show the trough part only, a typical waveform acquired is shown in Fig. 4.5 (a). At least two troughs should be included in the waveform so as to know the period of the fringe.

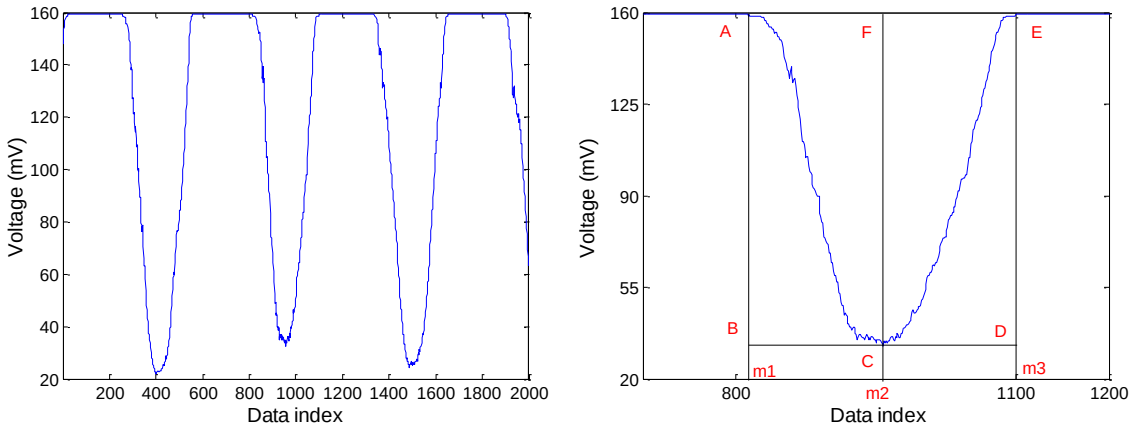

Fig. 4.5 (a) The waveform acquired in the trough position method. (b) A part of the waveform including only one trough for examination.

To determine the position of a trough, we have to make sure there is only one trough existing in the range of examination. As shown in Fig. 4.5 (b), where *A* and *E* are the start point and the end point of the trough, respectively; *C* is the minimum point of the

trough; m1, m2 and m3 are the sensing element indices on the LPDA corresponding to A, C and E, respectively. Then the index corresponding to the sensing element of the LPDA of trough position is calculated as

$$\text{Index of trough position} = \left[m1 + \frac{S_{ABC}}{S_{ABCF}}(m2 - m1) + m2 + \frac{S_{CFE}}{S_{FCDE}}(m3 - m2) \right] / 2 \qquad (4.4)$$

where S_{ABC} and S_{CFE} represent the areas of the triangle-like shape ABC and CFE respectively; S_{ABCF} and S_{FCDE} represent the areas of the rectangles of $ABCF$ and $FCDE$, respectively.

After the index of trough position is determined, the shift of the trough position between two consequent waveforms can be determined, and the phase shift in degree can be calculated as

$$\text{Phase shift } (^{\circ}) = \frac{d}{p} \times 180 \qquad (4.5)$$

Where d represents the difference between the indices of trough position in two waveforms acquired in tandem; p represents the period of the fringe curve.

Obviously, the trough position method can avoid to a certain extent the error arisen from truncation of the waveform, high distortion in the top of the fringe curve and nonlinear response of the detector. Moreover, different from other methods where more than ten periods of fringes are required, only three fringes are needed in our method. Thus more pixels on LPDA can be available for one period of the fringe, and this is another merit to the precise determination of the trough position.

4.2.4 Experimental results

This system was used to measure the displacement of the piezoelectric actuated mirror (model FK-18515 from Newport). Fig. 4.6 shows the measurement result. The hysteresis of the PZT can be clearly seen. The average number of the oscilloscope is set as 32, which means the waveform displayed on oscilloscope is an average of 32 scans from the LPDA; the duration of the measurement is 45 seconds. This experiment result shows the accuracy of the system has reached a certain level. However, to evaluate the accuracy of the measurement methodology, the thermal drift and non thermal drift of the system cannot be ignored.

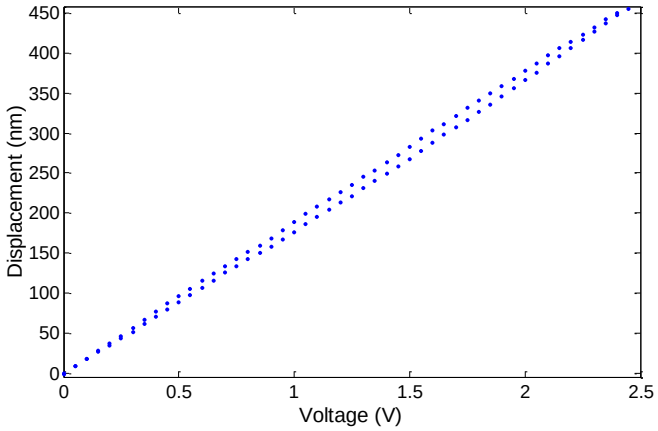

Fig. 4.6 Displacements measured clearly show the hysteresis of PZT.

4.2.4.1 Observation of thermal drift and non thermal drift

The measurement of the drift is carried out without any driving signal applied to the PZT mirrors. Fig. 4.7 (a) shows the drift of the system measured in a period of 10 hours. The room temperature was recorded at the same time using a temperature monitor from Instec co. (model STC 200), as shown in Fig. 4.7 (b). It can be seen clearly that the phase drift is following a similar pattern of the temperature fluctuation.

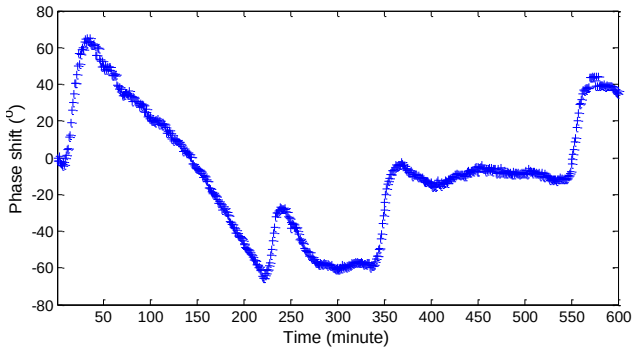

(a)

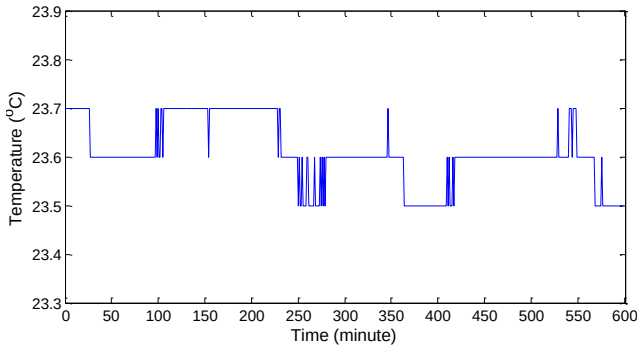

(b)

Fig. 4.7 (a) Drift measured in a period of 10 hour; (b) Temperature profile recorded synchronously.

Besides the existence of the thermal drift, non thermal drift also exists, which mainly comes from the flow and creep of materials under mechanical stresses. In the experiment setup, since all components are fixed by screws, so the stress undoubtedly exists. Fig. 4.8 (a) shows the measurement immediately after aligning the optical system. Since all the screws were locked shortly before the measurement, a remarkable drift speed in the beginning was observed, it then decayed slowly. The drift speed affected by the

temperature fluctuation can also be clearly seen by comparing with the temperature profile as shown in Fig. 4.8 (b).

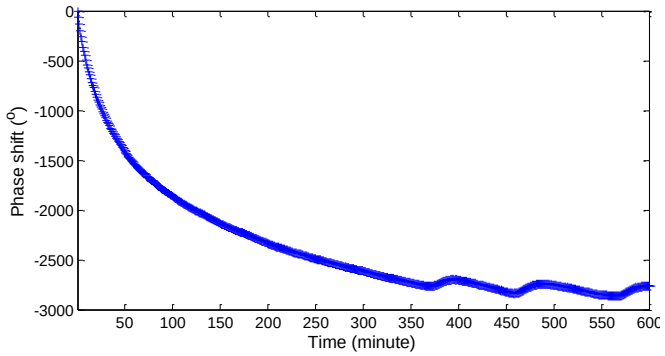

(a)

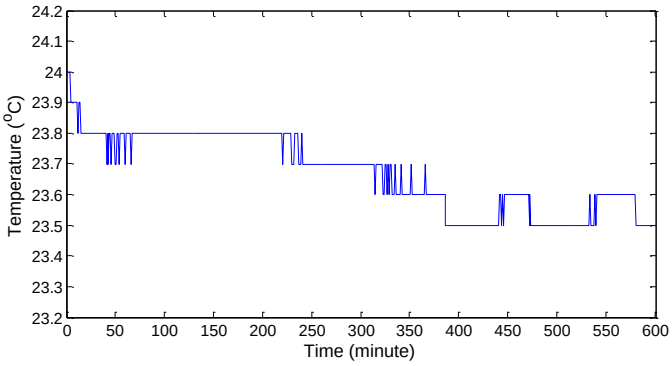

(b)

Fig. 4.8 (a) Drift measured in a period of 10 hour shortly after the alignment of optical system; (b) Temperature profile recorded synchronously.

4.2.4.2 Evaluation of the measurement accuracy

From above observations, it can be seen that it is not easy to control the drift speed within a very low level, because superior precision temperature control and special design in mechanics have to be involved. On the other hand, with the existing thermal drift and non thermal drift, it is still possible to evaluate the accuracy of the measurement method.

This is because in a short time interval, for example, less than one minute, both the thermal drift and non thermal drift can be approximately regarded as changing linearly with time, and thus the measurement deviation caused by drift can be deducted through linear curve fitting.

To evaluate the accuracy, the same PZT mirror in the hysteresis measurement was used, but the measurement was carried out in a smaller displacement range. The measurement results with the oscilloscope setting in different average number are shown in Fig. 4.9. The duration of the measurement shown in each figure is 45 seconds.

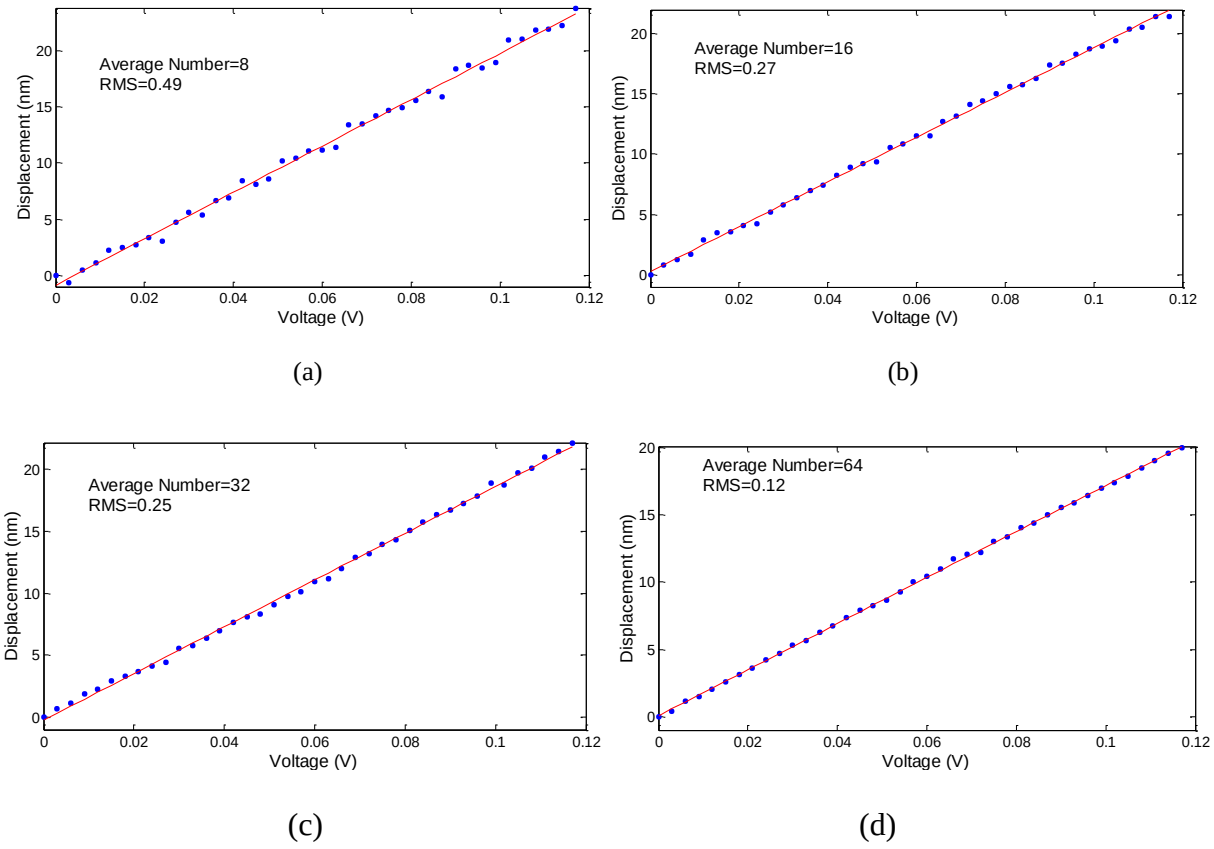

Fig. 4.9. The displacement versus driving voltage of Newport FK-18515 PZT mirror measured in the condition of different average number of the oscilloscope. (a) Average number=8; (b) Average number=16; (c) Average number=32; (d) Average number=64;

It can be seen that with the increase of average number, the standard deviation of the measured data (RMS values shown in the figures) is decreased. No explicit improvement of standard deviation was observed when further increasing the average number above 64.

In this experiment, the Agt33250A function generator is used to drive the PZT, each voltage increment is 3 mV. As the specification of this function generator indicates that the output voltage precision is ±1 mV, to avoid any deviation caused by the driving voltage, another PZT mirror with smaller displacement/voltage ratio was investigated. However, no explicit improvement of standard deviation was observed, therefore the deviation caused by the driving voltage in the experiments shown in Fig. 4.9 should be small.

4.2.4.3 Measurement of phase shift versus driving voltage of LC and PDLC

The system is used to measure the phase shift versus driving voltage of LC SPP. The phase shift versus voltage curve of LC SPP with cell gap of 5 μm and 18 μm measured with this system are shown in Fig. 4.10 (a) and (b), respectively. When doing this measurement, the LC cell is inserted in one of the arms of the interference system, with the rubbing direction of unti-parallel rubbed LC cell in parallel with the polarization of the laser beam.

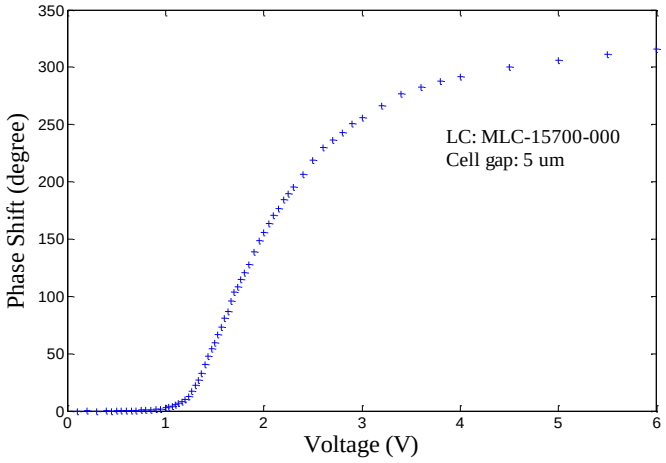

(a)

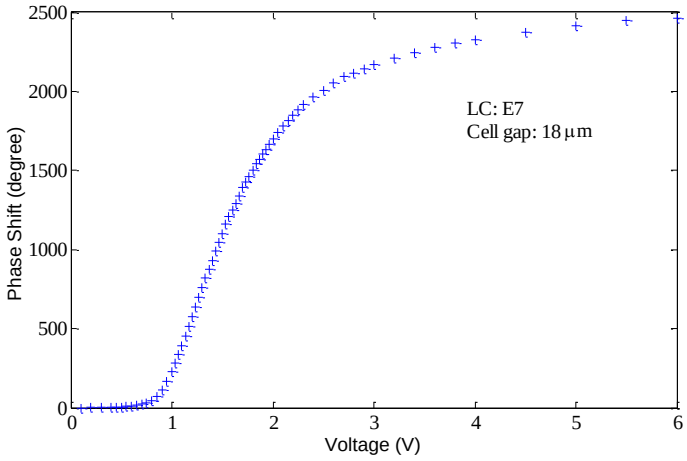

(b)

Fig. 4.10 (a). Phase shift versus voltage measured for 5 μm cell gap LC SPP.

(b). Phase shift versus voltage measured for 18 μm cell gap LC SPP.

A polymer-dispersed liquid crystal (PDLC) cell sample fabricated in our lab was also investigated by this system. The phase shift of PDLC cell can not be measured by any retardation measurement systems, such as polarimeter etc, because optical path of PDLC

cell are isotropic in different polarization directions. The measurement result for the PDLC cell is shown in Fig. 4.11. It can be seen that the deviation of the measured data is much bigger than normal LC cell. This should be caused by the strong scattering of the LC droplets inside the PDLC cell. Despite the strong noise, the threshold voltage and saturation voltage can still be estimated.

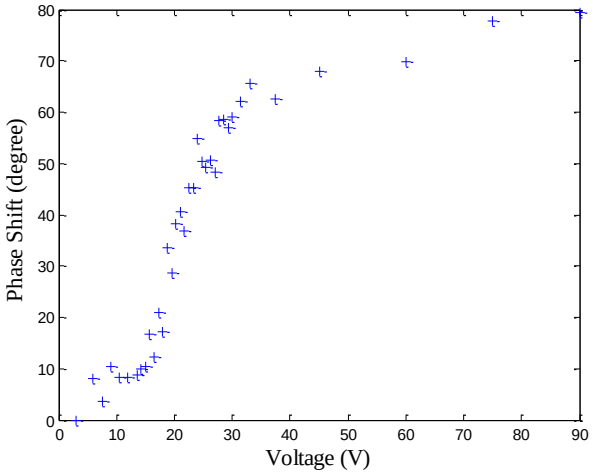

Fig. 4.11 The phase shift versus driving voltage of a PDLC cell measured.

4.2.5 Approaches to further improve the measurement accuracy

Though good experimental results have been obtained with the system using the trough position method, there is still room for further improving the measurement accuracy. One approach is to control the drift speed. This can only be achieved through ultra-precision temperature control and special designed mechanical parts. Another approach is to reduce the multi-reflection noise beam. Since the existence of the noise beam still affects the precise determination of the trough position, so reduction of the noise beam will help to further improve the accuracy. The third approach is to use USB

port LPDA with larger pixel number and higher scan frequency. This will help to determine the trough position more precisely, and shorten the measurement time.

4.3 Conclusions

For measuring the phase shift versus driving voltage of LC SPP, A high accuracy phase shift measurement system based on Michelson interferometer and a linear photo detector array was developed. This system uses a new data processing method, which extracts phase information from the trough part of the equidistant fringe. The advantage of this method is substantiated theoretically, and experimental results showed good accuracy. The thermal drift and non-thermal drift of the system were observed. After deducing the error caused by drift, 0.12nm standard deviation was achieved in displacement measurement of a piezoelectric actuated mirror.

The phase shift versus driving voltage of LC SPP was precisely measured using this system.

Chapter 5 Introduction to the fabrication process of LC SPP

The methodology and principle of the fabrication process of LC SPP are introduced in this chapter. The third type LC SPP is used as an example for the introduction. The fabrication flow chart is shown in Fig. 5.1. Each process will be introduced in detail in following sections.

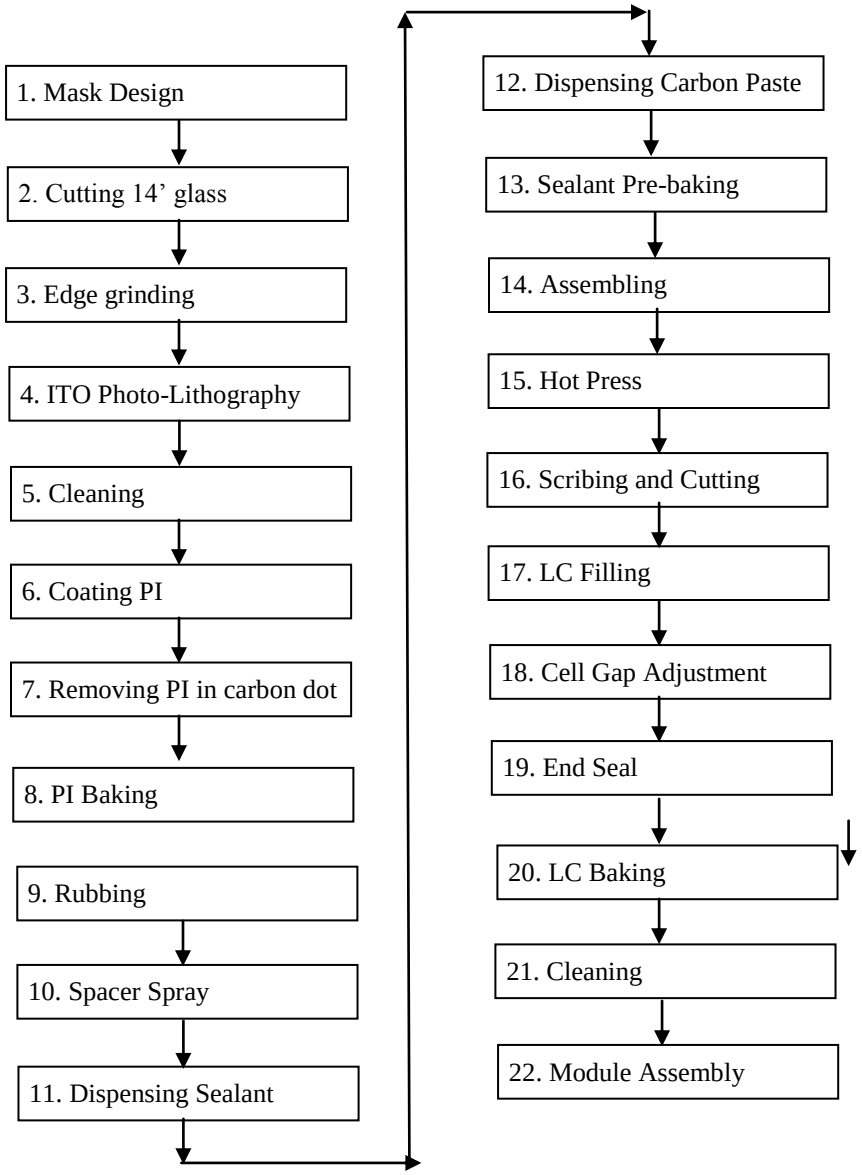

Fig. 5.1 The flow chart of the fabrication of the third type LC SPP.

5.1 Mask design, scribing and breaking of 14” glass, Edge grinding

1. Mask design

The mask was drawn by Virtuoso layout editor of Cadence design software. To fully utilize the mask space, several kinds of LC SPPs were integrated in one mask as shown in Fig. 5.2. The central column is for the third type LC SPP. The mask substrate is 5” x 5”x 0.09” Soda Lime Glass covered with chromium film. There are two small rings at the left and right sides, which are used as orientation marks in the fabrication process.

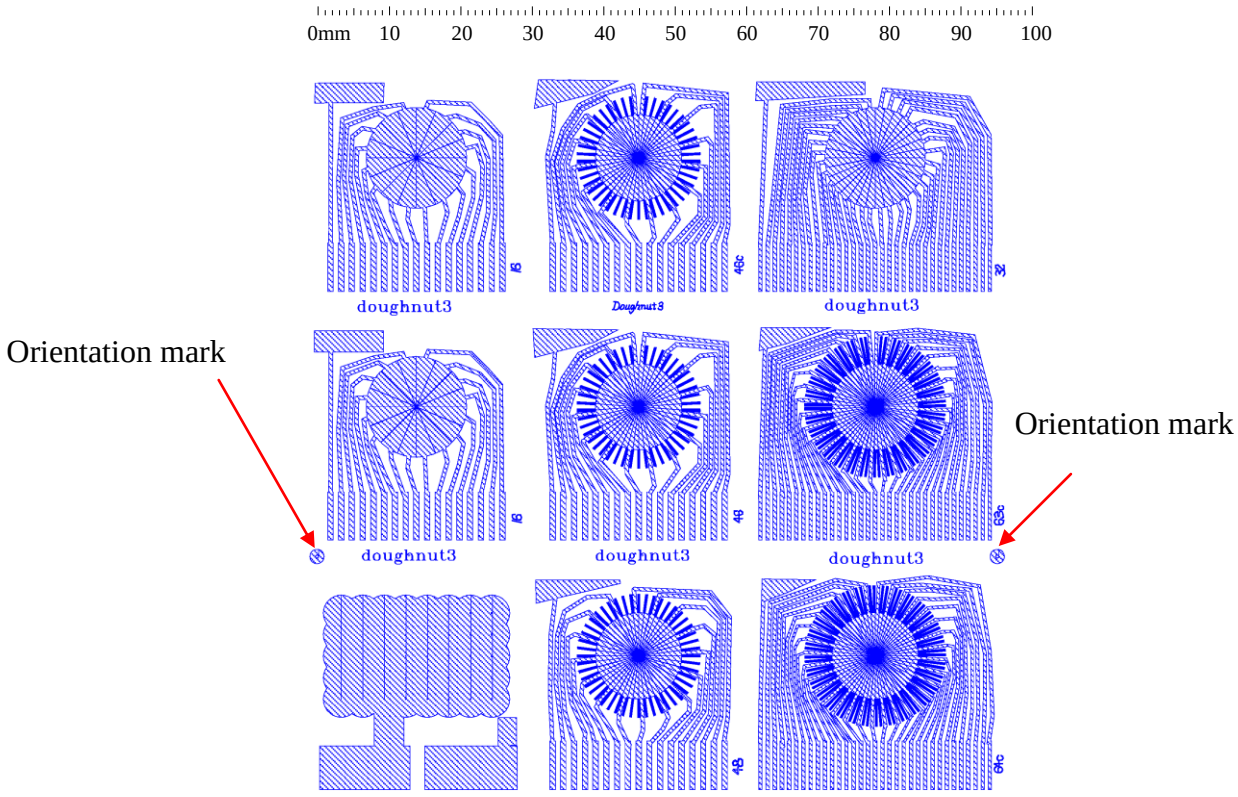

Fig. 5.2 The mask for making the third type SPP.

2. Scribing 14” ITO glass

The size of the raw ITO glass is 14”x14”, the square resistance of ITO film is 100Ω/□. The glass substrates need to be cut into 6”x6”, which is the standard substrate

size for the processing in the LC cell fabrication line. Glass-scribing machine was employed for this process. Any friction of ITO film must be avoided, or the glass debris generated in scribing will damage the ITO film. In most cases, such damage can be as fine as 20 μm in width, which can't be identified by naked eye, however, it may cause open circuit of ITO lines.

3. Breaking 14" ITO glass

As shown in Fig. 5.3, the hard rubber breaking head impacts the glass substrate to separate the substrate into two along the scribing line.

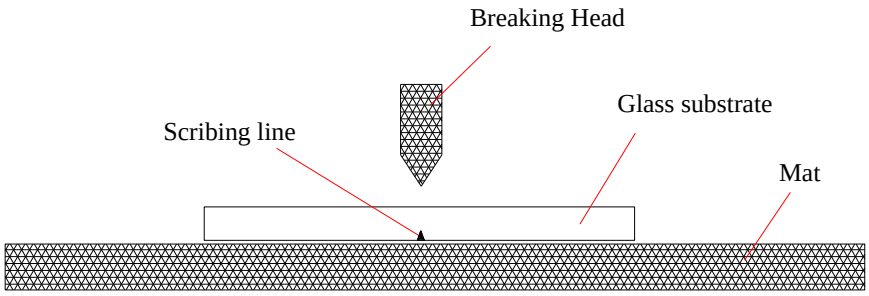

Fig. 5.3 The breaking process.

4. Edge grinding

The edges of the 6"x6" glass substrates were grinded by a grinder. The main purpose of this process is to avoid any glass debris generated from the edge of glass substrates in succeeding processes and to avoid any harm to operators. This process is illustrated in Fig. 5.4. The water is for lubrication purpose.

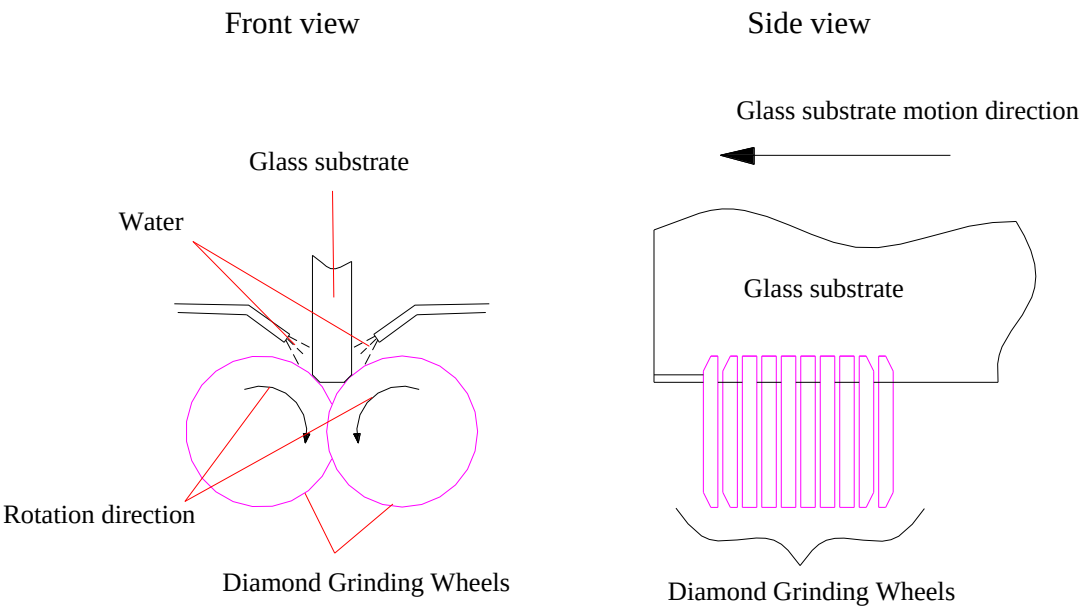

Fig. 5.4 Edge grinding process.

5.2 ITO Photo lithography

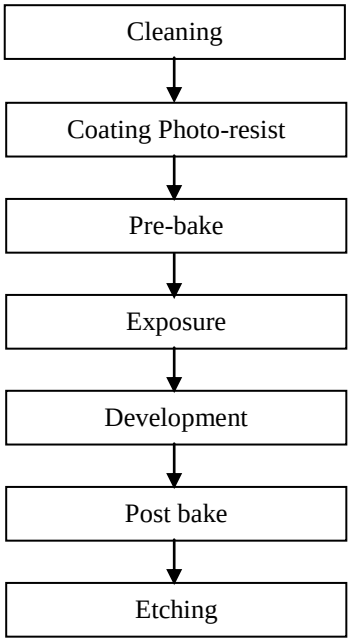

Fig. 5.5 Flow chart of ITO photo lithography.

The process flow chart of photo lithography of ITO layer is shown in Fig. 5.5. Followings are the detailed description to each process.

1. Cleaning

The 6”x6” ITO glasses were first loaded into a stainless steel or plastic basket, which was then dipped into 60℃ 2% DECONEX 12 PA detergent and was ultrasonically cleaned for 20 minutes. Then the glasses were rinsed in deionized water. After swinging it several times in deionized water, it was moved into a deionized water ultrasonic bath. After 15 minutes ultrasonic cleaning, it was moved into the second ultrasonic bath with warm deionized water (about 55℃), and ultrasonically cleaned for another 15 minutes. After that, the basket was put into 125℃ oven for 30 minutes to dry the glass substrates, and then it was cooled down on a class 100 laminar flow table for further processing.

2. Coating Photo-resist

Spin coater was used in this process. The type of the photo-resister is SPR2-FX-1.3 (Shipley, positive photo-resist), acceleration 3000rps, 2000rpm, 25 seconds. The temperature of glass substrates should be reduced to room temperature before coating photo-resist, otherwise the thickness of the photo-resist film will be uneven.

3. Pre-baking

The condition for pre-baking was 100℃, 15 minutes for oven baking or 100℃, 2 minutes for hot plate baking. If the pre-baking is not enough, the photo resist film will be

too soft when doing development, and the fine lines separated with narrow gap tend to be shorted. If it is over pre-baked, the photo resist film exposed to UV light is difficult to be dissolved in the solution for development.

4. Exposure

The glass substrate was exposed to UV light with the chromium film side of the mask contacting with photo-resist film side. The intensity of the UV light was 10mW/cm^2 and the exposure time was 10 seconds.

5. Development

In this process, the photo resist film exposed to UV light is dissolved in solution. The solution for developing can be bought from company, and it can also be self prepared. The solution I used was self-prepared, which was composed of water/tri-sodium phosphate/sodium hydroxide=4.2liter/1.25g/12.5g. The developing time was about 30 seconds. During this period, the glass substrate should be kept vibrating to prevent the residue of photo-resist dissolved in the solution from adhering to the substrate. After that, the glass substrate was rinsed with water thoroughly and dried with air gun.

6. Post baking

The purpose of this process is to make the photo resist film to withstand the acid corrosion in the following etching process. The condition for post baking was 120℃, 25 minutes for oven baking or 120℃, 2~3 minutes for hot plate baking.

7. Etching

The solution for etching ITO is water : hydrochloric acid=1 : 1. The temperature of the etching solution was 40±1℃, the etching time was 2~2.5 minutes. Since the etching speed is sensitive to the temperature, that's the reason to control the solution temperature within a range of ±1℃. After etching, the glass substrate was rinsed with water thoroughly, and then dried with air gun.

8. Photo-resist stripping

The remaining photo-resist can be cleaned away by acetone or dipping into 5% sodium hydroxide water solution.

5.3 Coating polyimide (PI), removing PI under the carbon paste dot and PI baking

1. Coating polyimide (PI)

Before coating PI, the ITO substrates must be cleaned again; the cleaning process is the same as that in section 5.2. The PI solution (which is actually polyamic acid) is SE-130 from Nissan Co. PI layer were coated on both the ITO patterned substrate and the blank ITO substrate using spin coater. The parameters of spin coater were 3000 rps (acceleration), 2500 rpm, 20s. The two substrates would be assembled together in the assembly process. After coating, the substrate should be put into 80℃ oven 15 minutes for drying the solvent.

2. Removing PI under the carbon paste dot

As the PI layer is an insulator, it can depress the conductivity of carbon paste spot, which is used for transferring the ground electrode to opposite substrate. So the PI layer at the place for carbon paste spot must be removed by cotton stick dipped with acetone. The areas with blue color shown in Fig. 5.6 represent the positions where the PI layer is removed.

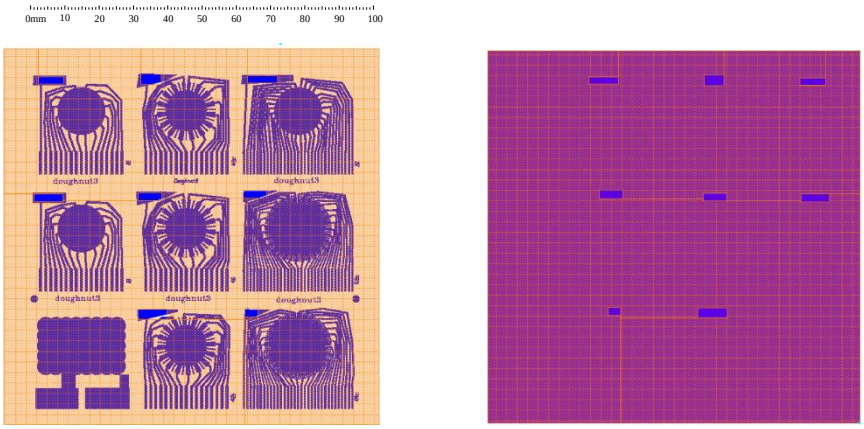

Fig. 5.6 PI layer should be removed in the places indicated in blue color for dispensing carbon paste.

3. PI Baking

As mentioned previously, the PI coated on glass substrates is actually polyamic acid. To get the polyimide film, the polyamic acid needs to be dehydrated by keeping the coated substrates in 250℃ oven for 60 minutes.

5.4 Rubbing, Spacer Spray, Dispensing Sealant and Conductive Paste

1. Rubbing

The purpose of this process is to form micro grooves on the PI film so as to orient LC molecules in a specific direction. Fig. 5.7 shows the relationship between the rubbing direction and the director of LC molecules. The pretilt angle shown in the Fig. 5.7 (b) normally is 1 ~3 °. The grooves are made by rubbing on the PI film with a velvet-like cloth with its fiber upright.

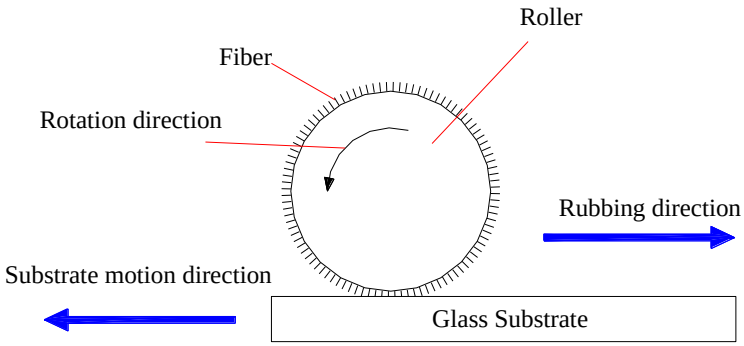

(a)

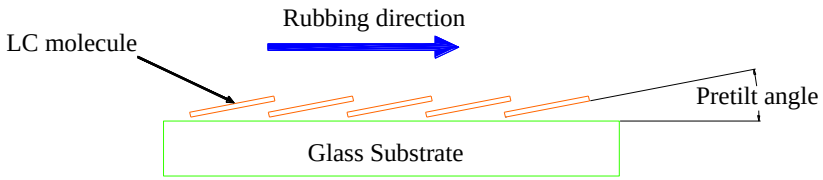

(b)

Fig. 5.7 (a) Illustration of rubbing process. (b) The relationship between the rubbing direction and the director of LC molecules.

The rubbing is carried out in this way: The velvet-like cloth is wound on a cylindrical roller. When the roller is rotating, a stage carried with the substrate is slowly passing through the roller from the beneath. The height of the stage is properly set so that the fiber of the velvet-like cloth will rub the surface of the substrate.

The rotational speed of the roller is 800 rpm, the speed of the stage is 5 m/minute. The fiber of rubbing cloth is compressed about 0.2 mm to 0.3 mm during rubbing.

Two substrates to be assembled are rubbed in anti-parallel direction, which means the angle of the rubbing directions of the two substrates is 180 ^{o} after assembling. Since the speed of stage is much slower than that of the roller, no matter which direction the stage is moving, the rubbing direction is determined by the rotation direction of roller.

2. Spacer Spray

Spacers for common applications are micro spheres made of plastic material. They are distributed inside the LC cell to maintain a uniform cell gap. The spacers are only sprayed on one of the two substrates, normally the blank substrate. The working principle of the spacer spray machine is illustrated in Fig. 5.8.

When the compressed air flowing through the vacuum ejector, the spacers are sucked into the tube due to the principle of hydromechanics, and then sprayed out from the nozzle. Since the spacers are very small, they tend to suspend in the air for a while before falling down to the bottom. This period may last several minutes if there is no extra force applied to them excepting the gravity.

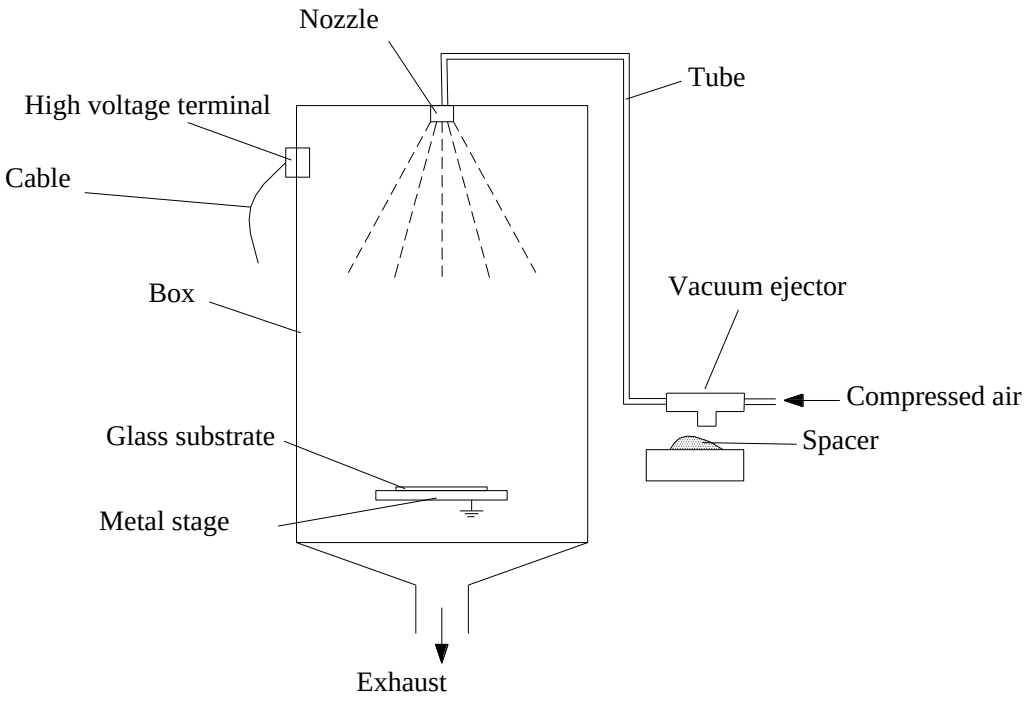

Fig. 5.8 The working principle of spacer spray machine.

The high DC voltage (3~5 kv) generated from a high DC voltage generator is applied to a terminal fixed on the box. As the box is made of electrically conductive plastic, the whole box is charged with high DC voltage, either positive or negative, which can be controlled by a switch. The electric field is established between the wall of the box and the glass substrate which is placed on a grounded metal stage. On the other hand, the spacer made of dielectric material tend to carry static charges, normally, the polarity of the static charge carried is determined by the spacer material. If the polarity of the DC high voltage matches, the spacers will drift to the glass substrate in the force of the electric field until

they reach it. Otherwise, most of the spacers would drift to the box, and there will be little spacers reaching the substrate.

The distribution of the spacer can be investigated under a microscope, normally, for spacer of 6μm, the proper density should be 80~100 spacers per square millimeter. The larger the spacer diameter, the lower the density needed. For spraying the 18μm spacer for the third type LC SPP, the spray air pressure was 3.5 atm, the spray time lasted 10 seconds, the voltage was –5.5 kV. The density of the spacer was about 15~25 spacers per square millimeter.

The reason for spraying spacer on the un-patterned substrate is that, the patterned ITO layer causes the non-uniform distribution of the electric field near the surface of the substrate, and this results the difference of the distribution of spacers between the areas covered with ITO and that without ITO.

In the case when spraying smaller size spacers after spraying larger size spacers, the larger size spacers may mix into the smaller size spacers and affect the cell gap uniformity. Therefore, if a new size spacer is to be sprayed, the tube and vacuum ejector have to be cleaned thoroughly. However, using a dedicated tube and vacuum ejector for each kind of spacer is a more efficient and reliable way.

3. Dispensing Sealant

The purpose of this process is to dispense peripheral sealant for sealing the two glass substrates together so as to form a LC cell. The main composition of the sealant material is epoxy.

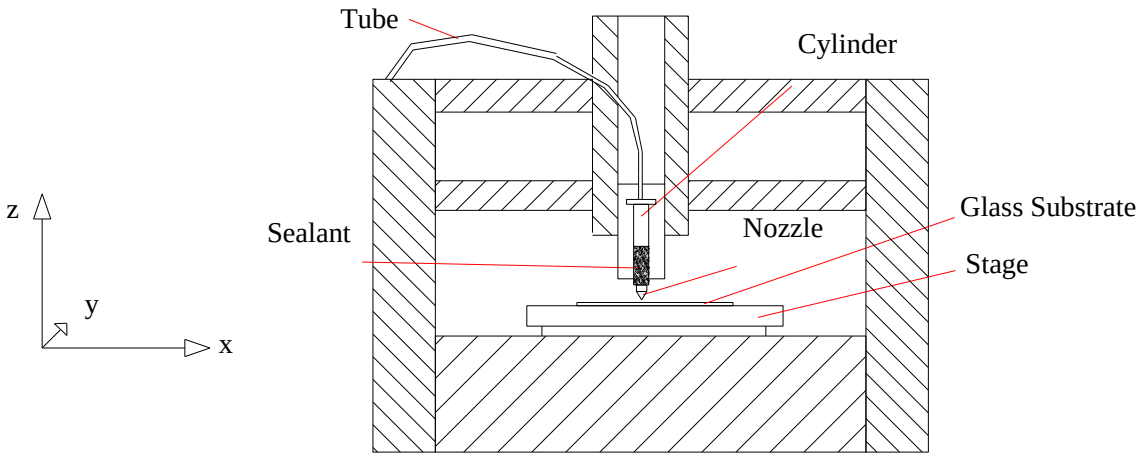

Fig. 5.9 Sealant drawing machine.

The sealant drawing machine is schematically shown in Fig. 5.9. The nozzle can move in x, z axes, and the stage can move in y axis. The motion repeatability is within ±10 μm. The dispensing of the sealant is controlled by the compressed air. The moving of the stage and the nozzle as well as applying compressed air are program controllable.

The type of the sealant used is XN-21-S. As the SPP cell gap is much larger than normal LCD cell, a nozzle with a hole of 0.2 mm in diameter was used to dispense sealant. The gap between the nozzle and the substrate was 70 μm, which was checked by an insert

ruler. The moving speed of the nozzle was 5 mm/sec. Fig. 5.10 schematically shows the substrate after dispensing sealant.

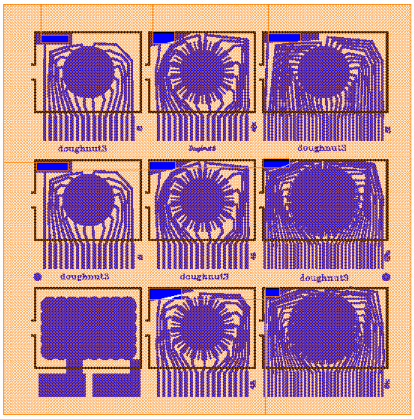

Fig. 5.10 The substrate after dispensing sealant.

4. Dispensing Conductive Paste

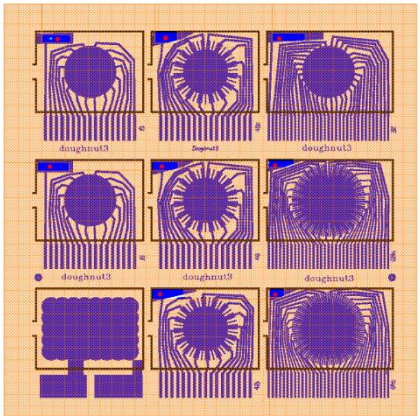

Fig. 5.11 The substrate after dispensing carbon paste.

The carbon conductive paste, a mixture of carbon powder and thermal curable epoxy, is used in this process. This process is the same as dispensing sealant. Fig. 5.11 shows the carbon dots, which are represented by those small dots with red color for clear view.

5.5 Sealant Pre-baking, Assembling, Hot Press, Scribing and Breaking

1. Sealant Pre-baking

The solvent in the sealant should be evaporated first to avoid any cavity after thermal curing. Therefore, the substrate drawn with sealant must be put into 80 ℃ oven for 15 minutes before assembling.

2. Assembling

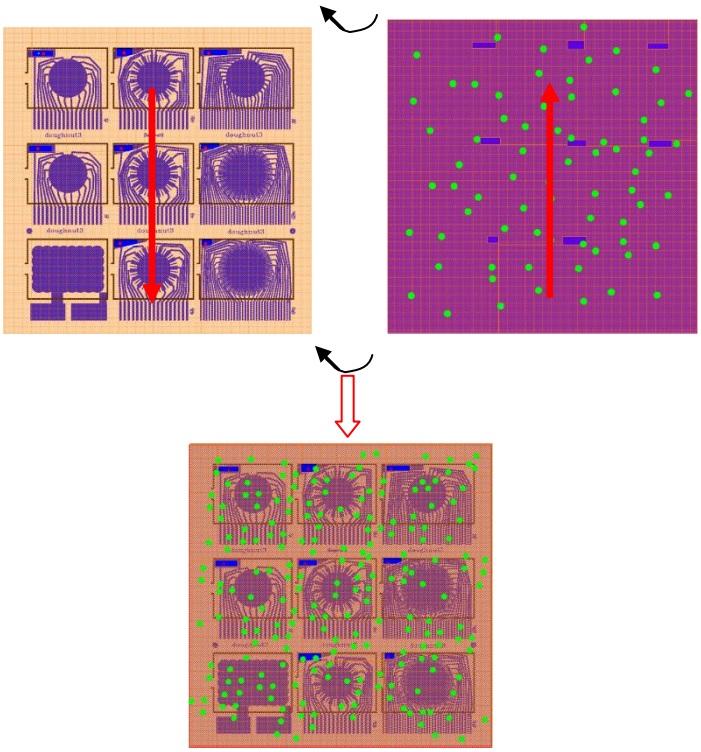

Fig. 5.12 A pair of substrates are assembled together with their rubbing direction anti-parallel aligned.

After the pattered ITO substrate with sealant drawn and the blank ITO substrate with spacer distributed are ready, they are assembled together using hands on a laminar flow table, with the rubbing directions of two substrates in anti-parallel as shown in Fig. 5.12.

3. Hot Press

Fig. 5.13 illustrates the hot press process. The purpose of the silicon rubber sheets is to evenly distribute the press applied to the whole LC substrate. Heat resistant paper is for preventing the glass substrates to be contaminated by the silicon rubber. Teflon sheet acts as a support for the whole stack before it is inserted in between the upper and bottom plate. The pressure is applied through a pneumatic cylinder. The heater for controlling the temperature is inside the upper plate and the bottom plate.

The temperature for the hot press process used was 150 ℃, the time for the whole process was 90 minutes. After hot press, the width of sealant expanded from about 0.4mm to about 1mm.

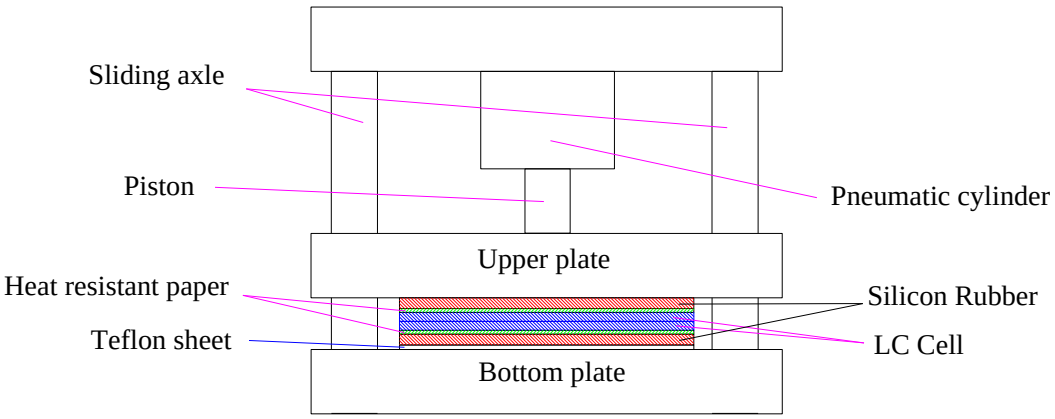

Fig. 5.13 Hot press process.

4. Scribing

In this process, the 6”x 6” glass substrate is scribed, so as to obtain single cells in succeeding breaking process. As shown in Fig. 5.14, the blank ITO substrate is in front of the ITO patterned one. The green horizontal lines represent the scribe line on the back

substrate, and the orange lines represent the scribe lines on the front substrate, the pink vertical lines represent there are scribe lines on both substrates. Several improvements have been done with this process, which will be described in chapter 6.

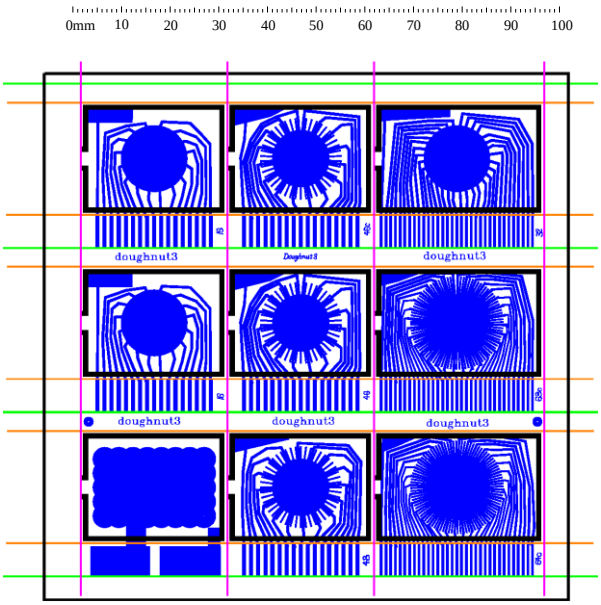

Fig.5.14 Scribing lines.

5. Breaking

In this process, the scribed substrate is broken into single cells. The principle is the same as that shown in section 5.1. It should be noted that the two substrates should be broken separately.

5.6, LC filling, Cell gap adjustment and end seal, LC Baking, Cleaning and Module Assembly

1. LC filling

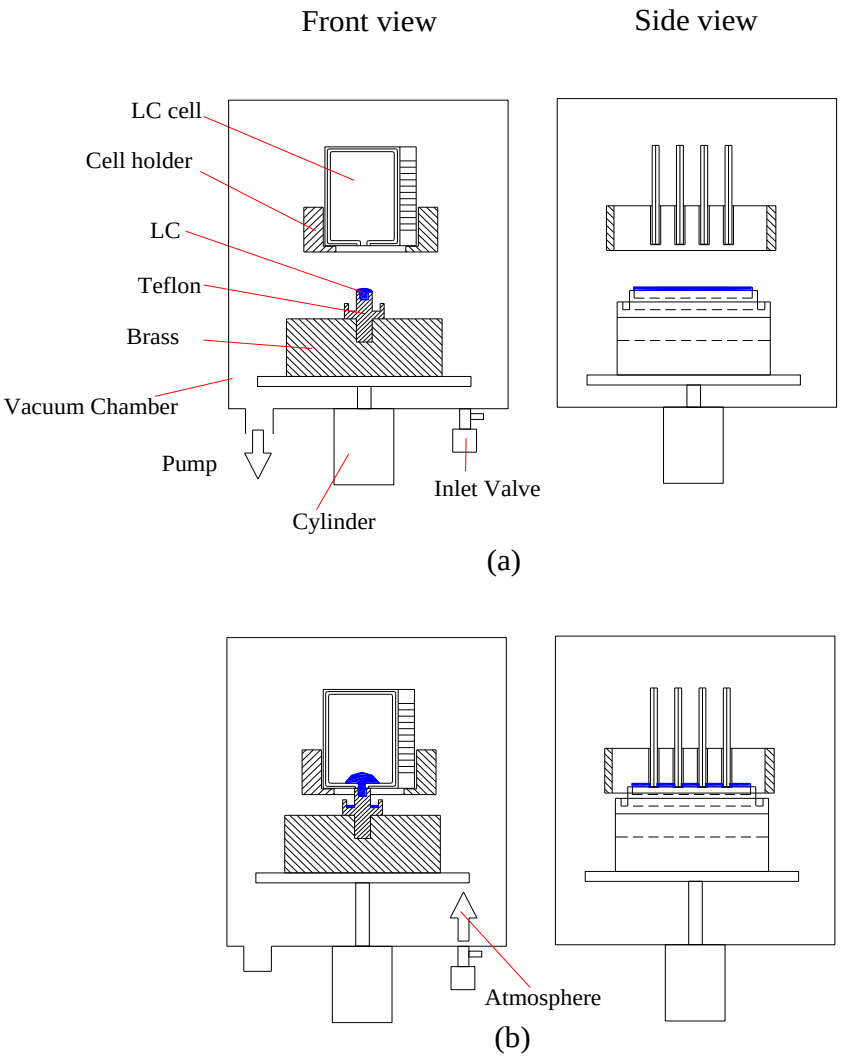

Fig. 5.15 LC filling process.

In this process, the single cells will be filled with LC. The LC filling process is illustrated in Fig. 5.15. Before LC contacting the filling hole of LC cell, the chamber is vacuumized to around 1 Pa, which is realized by a mechanical pump followed by a Roots pump. Then the LC container is lifted up to contact with the LC cell by the cylinder, after that, the pump is shut down, and the chamber is filled with air through the inlet valve. The LC is pushed by the atmospheric pressure to fill the whole cell.

It is wroth mentioning that the air pressure inside the chamber should not be higher than 2×10^4 Pa before the LC reaching one-fourth of the whole cell, so as to avoid the damage to the alignment layer by the fast flowing LC. After that, the air pressure can be increased to one atmosphere to accelerate the filling process.

2. Cell gap adjustment and end seal

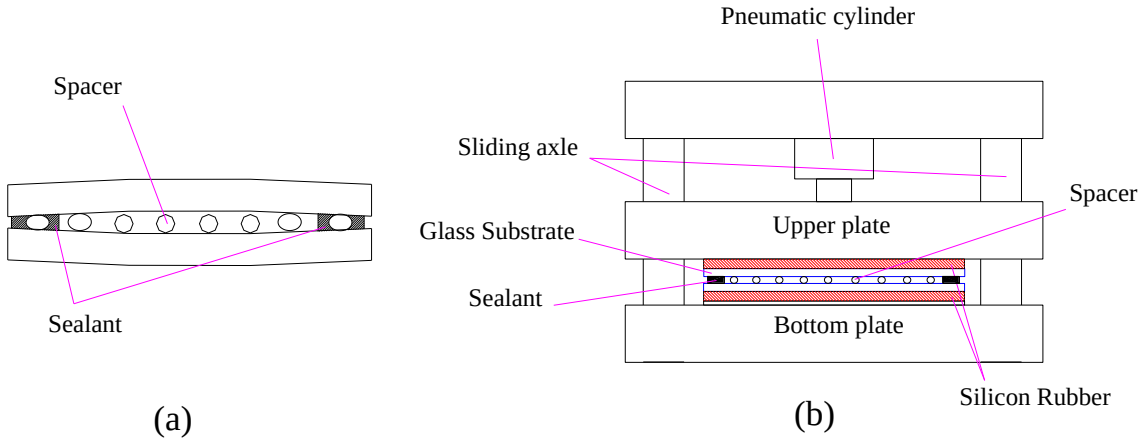

Fig. 5.16 (a) Diagram of the bulged cell after hot press; (b) Illumination of cell gap adjustment.

After hot press process, the cell will be bulged as shown in Fig. 5.16 (a). The mechanism of bulging is introduced in detail in section 6.4. As shown in Fig. 5.16 (b), to flatten the bulged cell, an uniform pressure of about 0.3 kg/cm^2 is applied to the whole substrate. After keeping the pressure for 1 to 2 minutes, some LC is squeezed out from the filling hole. After wiping away the squeezed LC away, the UV glue is applied to seal the filling hole. Then the pressure is reduced to 0.25 kg/cm^2, after two minutes, to cure the glue using a UV light source.

Since the spacers are elastic, the final cell gap is determined by many factors, such as pressure and spacer density, size, material of spacers.

3. LC Baking

In this process, the LC cell is baked in an oven of 115 ℃ for 15 minutes. The temperature is slightly higher than the clear point of the LC material. The purpose of this process is to eliminate the stress existing on the surface between LC and the alignment layer so as to form more uniform and stable alignment.

4. Cleaning

Now the fabrication of the LC SPP cell has been finished. There is some LC contamination on the panel, which can be cleaned by tissue paper dipped with acetone or plunging the cell into an acetone ultrasonic bath for 20 seconds (longer time may damage the seal of filling hole).

5. Module Assembly

The module assembly is shown in Fig. 5.17, the connection between LC cell and PCB is using a zebra rubber connector.

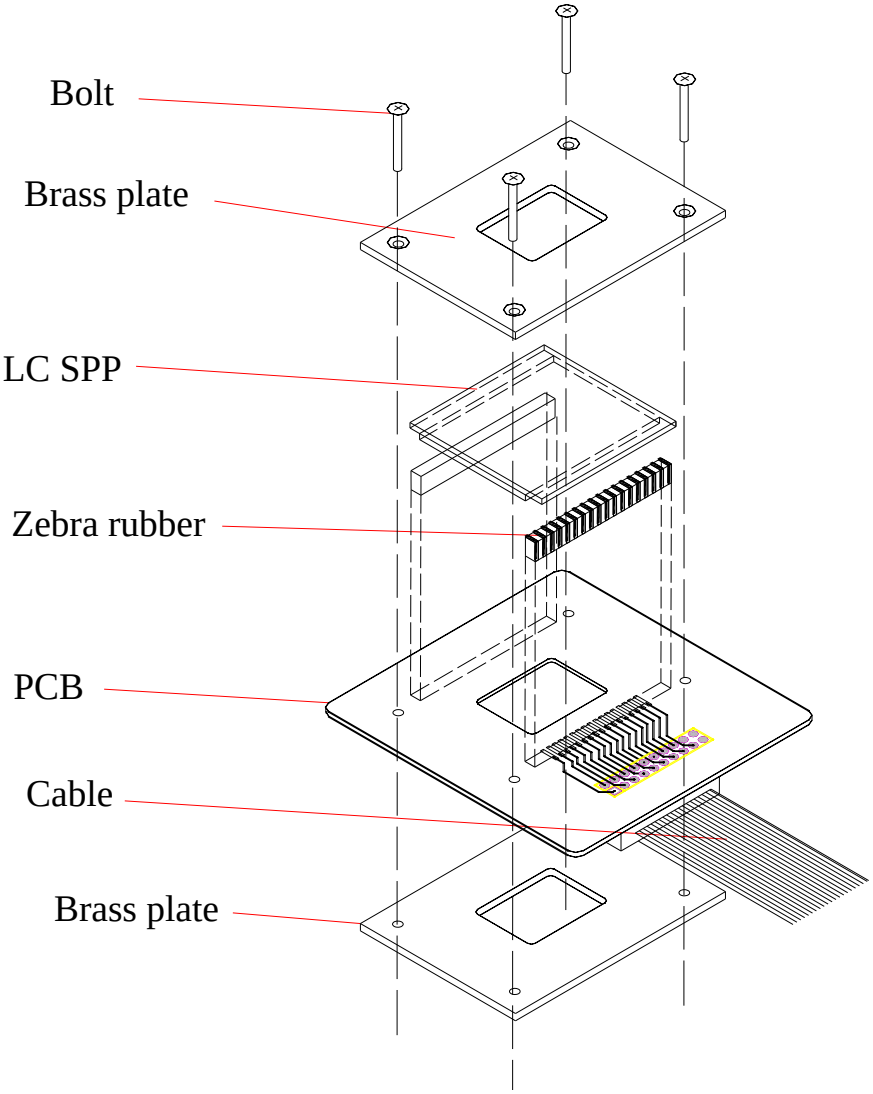

Fig. 5.17 Module assembly of the third type LC SPP.

Chapter 6 Major improvements to the LC cell fabrication process

Some improvements to the LC cell fabrication process have been done. These improvements not only benefited the fabrication of LC SPP, but also benefited the fabrication of other kinds of LC cells as well.

6.1 Improvements to the glass scribing process

6.1.1 Developing a CCD alignment system to align the glass substrate

To scribe the line accurately, the glass substrate should be aligned precisely. Initially, we used the method of aligning the sealant line along two orthogonal directions scribed on the machine stage, however, this method is not convenient in operation and not accurate. To solve this problem, an imaging system using CCD camera, which is shown in Fig. 6.1, is designed for the orientation of ITO patterned glass substrates. Since the cutting head robot move around above the stage, there is no space for placing the image system above the stage. The only place to house the image system is beneath the stage. However, the space beneath the stage is only 70 mm height, thus a 45 ^{o} mirror is used for saving the space.

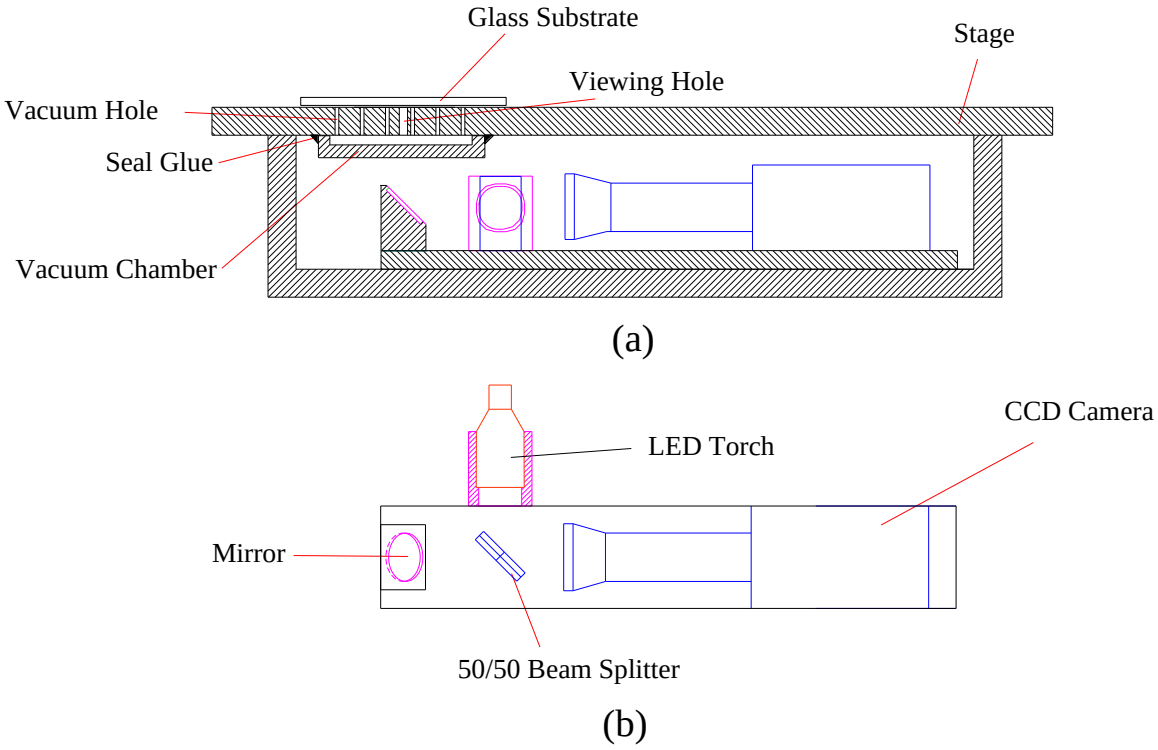

Fig.6.1 CCD imaging system. (a) Side view; (b) Top view with stage removed to allow the visibility.

Since the ITO layer is transparent (normally, the transparency is around 90%), it is only visible under reflected light beam. Thus, the coaxial illumination is indispensable. An economic 50/50 beam splitter is used for coupling the coaxial illumination beam. A torch with five white LED is used as the illuminator; this kind of torch has more uniform illumination and longer lifetime than normal bulb torch. The torch is driven by a 3V DC voltage source. Special attention was paid during the design of the focus length of the CCD lens, which should be compatible with the space and the image magnification required.

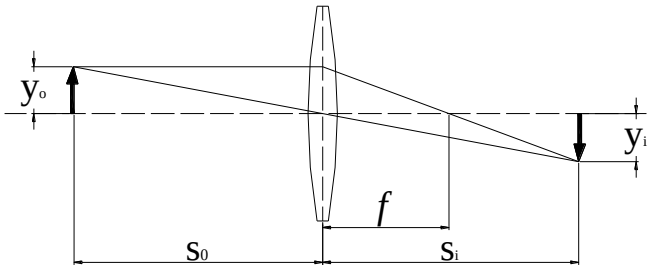

(a)

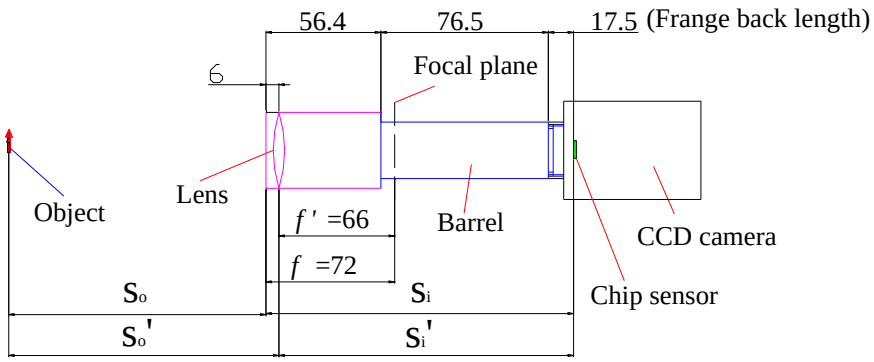

(b)

Fig. 6.2 (a). Object and image locations for a thin lens. (b). Dimensions of the camera system.

Fig. 6.2 (a) shows the object and image location for a thin lens. Since the alignment marks on glass substrates are usually small, the transverse magnification $M_T \equiv \frac{y_i}{y_o} = \frac{s_i}{s_o}$, should be large. As s_o is fixed to be around 150 mm due to the space limitation, to get large M_T, we must increase s_i. On the other hand, since $\frac{1}{f} = \frac{1}{s_0} + \frac{1}{s_i}$, and $f = 1/\left(\frac{1}{s_o} + \frac{1}{s_i}\right)$,

increasing s_i results in the increasing of f, thus lens with long focus length should be chosen. Based on this analysis, the commercial lens with 75 mm focus length was chosen. The barrel extender kit with total length of 76.5 mm, which includes 0.5 mm, 1 mm, 5 mm, 10 mm, 15 mm and 40 mm spacers, is used for extending s_i. Additionally, the flange back length, which is indicated in Fig. 6.2 (b), is equal to 17.526mm, which is the standard value for any C-mount CCD ("C-mount" is the most common interface between CCD and lens, it was chosen for our system). These dimensions are shown in Fig. 6.2 (b), so $s_i = 145$ mm, and $M_T \approx 1$, the alignment mark is about 1.5 mm in diameter, and the diameter of the image on the CCD chip sensor is also around 1.5 mm, assuming the CCD chip size is 1/3 inch (width=4.8 mm, height=3.6 mm), the image of the mark is supposed to occupy nearly half of the screen width.

Though the nominal measure of the focus length is 75 mm, the actual measurement is a little bit different, as shown in Fig. 6.2 (b). The height of LCD screen is 120 mm, the height of the object for the experiment is 1 mm. The calculated values of the object distance and the transverse magnification are shown in Table 6-1 and Table 6-2 for s_o, s_i, f and $s_o^{'}$, $s_i^{'}$, f', respectively. The experimental results show that the calculation based on s_o, s_i and f is much more accurate than that based on $s_o^{'}$, $s_i^{'}$ and f'. This is possible due to the reason that the lens group can't be treated simply as a thin lens. However, when the datum plane moves from the center of the lens to the edge of the lens barrel, the error by simply applying the thin lens equation to the actual lens group of CCD can be well corrected, as shown in Table 6-2.

Table 6-1 Comparison of experimental value and calculation based

on $s_o^{'}$, $s_i^{'}$ and f' shown in Fig.6.2 (b).

	Calculated value (mm)	Measured value (mm)	Proportional error
Object distance $S_o^{'}$	121.6	147	17%
Transverse magnification M_T	40.3	35	15.3%

Table 6-2 Comparison of experimental value and calculation based

on s_o , s_i and f shown in Fig. 6.2 (b).

	Calculated value (mm)	Measured value (mm)	Proportional error
Object distance S_o	138.1	141	2.1%
Transverse magnification M_T	36.3	35	3.7%

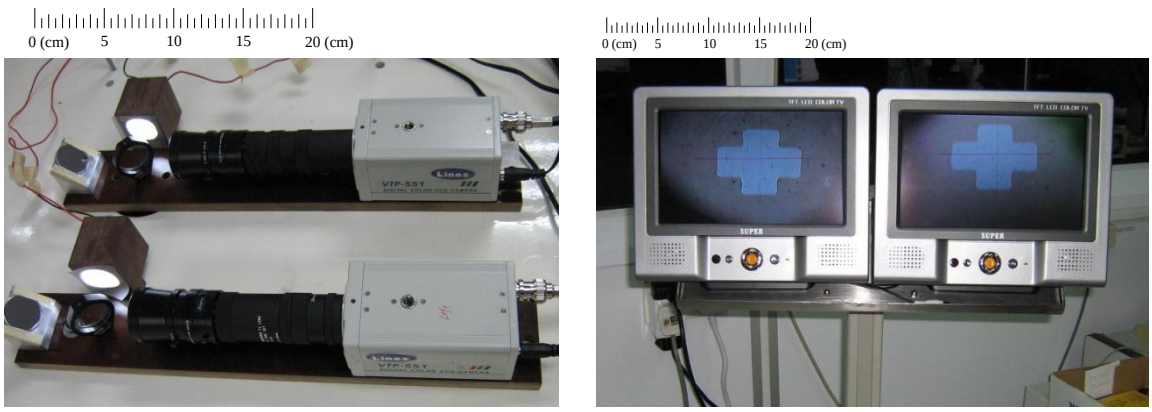

(a) (b)

Fig. 6.3 (a) Photograph of the CCD imaging system. (b) Photograph of the ITO alignment marks on LCD monitors.

The photos of the CCD imaging system and the ITO alignment marks on LCD monitor are shown in Fig. 6.3 (a) and (b), respectively.

6.1.2 Developing control program for automatic scribing

Initially, when scribing one line on a glass substrate, it was carried out in following sequence: (1). Measure the dimension for scribing; (2). Key in the dimension from the front panel; (3). Press “write” button six times to write this datum; (4). Press the “start” button to execute the scribing; (5). Press the “reset” button to reset the machine. When scribing another line, this procedure has to be repeated. For scribing the third type LC SPP, this procedure has to be repeated many times. This is not an efficient way. To solve this problem, a new program coded with Ladder-X language was developed to control the motion of the machine robot, all the scribing dimensions can be set in the program at one time, and the machine operates automatically following the program. In this way, scribing one LC SPP panel only takes no more than two minutes. The source code of the program is shown in Appendix C.

6.1.3 Using vacuum suck to hold the glass substrate when scribing

Initially, the glass substrates were fixed on the stage by use of adhesive tape during scribing, which was not convenient in operation, and the fixing was not very stable. Now a vacuum chamber as shown in Fig.6.4 (a) has been designed and fabricated for holding glass substrates instead of using adhesive tape when scribing. To fix or remove the glass substrate, only need to turn on or off a switch. Not only this method is more convenient than that using adhesive tape, but also glass substrates can be held more stable when

scribing. Two vacuum chambers have been fabricated for holding 14’’ and 6’’ glass substrates, separately. The holes for conducting vacuum were drilled on the stage as shown in Fig. 6.4 (b).

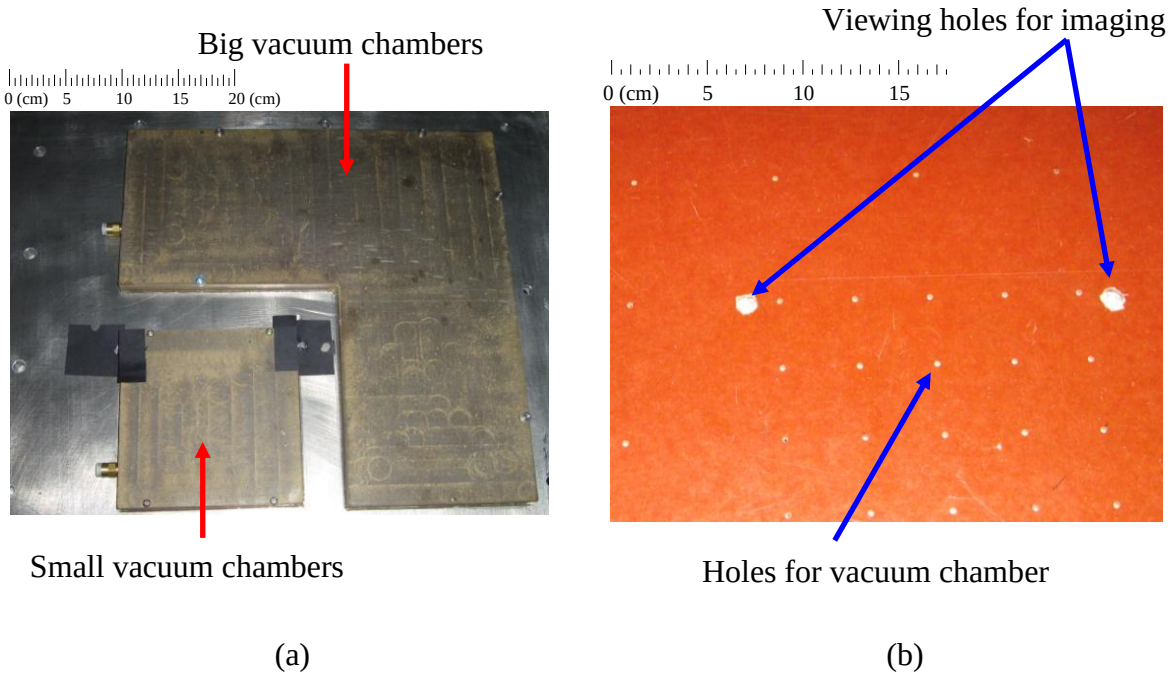

Fig. 6.4 (a) Photography of the big vacuum chamber and small vacuum chamber; (b) Photography of the stage.

6.1.4 Reducing glass debris by using scribing wheel with larger cutting angle

Initially, there was quite a lot of glass debris generated during scribing. As mentioned in section 5.1, the glass debris tends to damage the ITO film. After carrying out a series of experiments, it was found that the problem was caused by improper cutting angle of the scribing wheel. After replacing the original glass scribing wheel with a cutting angle of 115 º with another one with a cutting angle of 135 º, this problem was greatly alleviated. The cutting angle is schematically shown in Fig. 6.5.

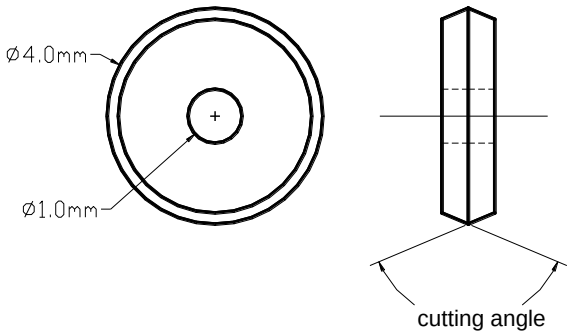

Fig. 6.5 Drawing of the scribing wheel.

6.1.5 Summary

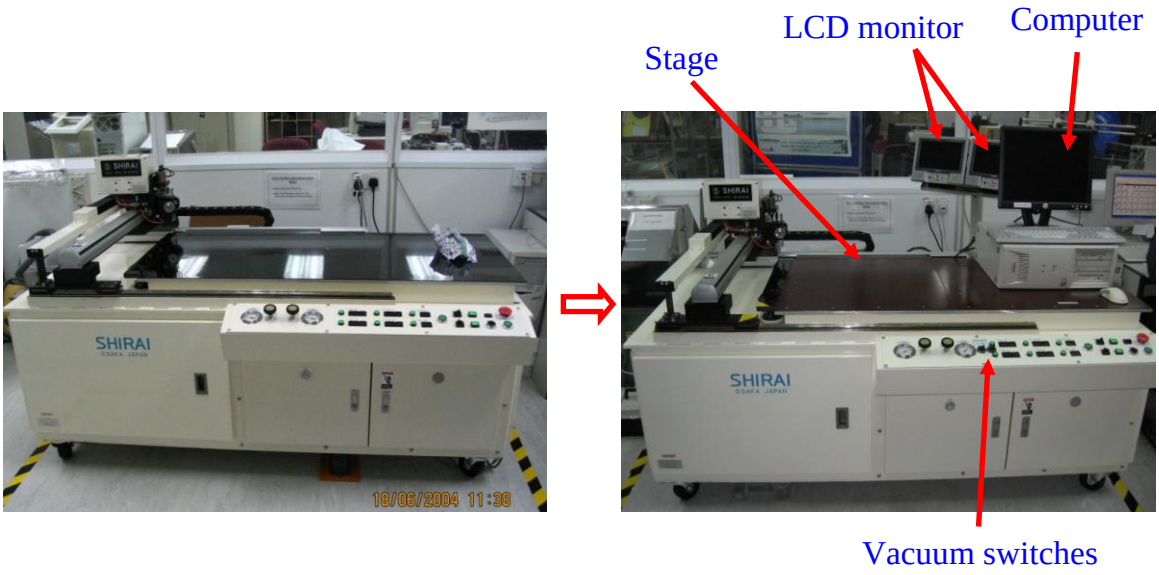

(a) (b)

Fig. 6.6 (a) Photography of the glass scribing machine before changing;

(b) Photography of the glass scribing machine after changing;

A CCD imaging system and vacuum chambers were created to the glass scribing machine for the precise alignment of the glass substrates, a program was developed for the

control of the automatic batch scribing. The glass debris problem was greatly alleviated by using scribing wheel with proper cutting angle.

Fig. 6.6 shows the comparison of the glass scribing machine before and after changing. The computer shown in the figure is for the editing and selection of glass scribing programs.

6.2 Improvement to the sealant drawing process

Several problems existed in sealant drawing process have been solved. The first problem is the orientation problem. Since the sealant drawn should precisely match the ITO pattern on the glass substrate, the orientation of the glass substrate must be precise. This problem is solved by pilot dispensing procedure. First, two orientation marks are designed on the mask as shown in Fig. 5.2. After lithography, these two marks are changed into ITO pattern which can be seen visually. When drawing sealant, we can dispense one spot of sealant near each mark respectively before the formal drawing, then the misalignment between the sealant spots and the marks can be offset by changing the coordinate data in the dispensing program. The process is repeated until the spots and the marks are precisely matched before starting the formal drawing.

The second problem is to control the dispensing speed of the sealant. The dispensing speed of the sealant is crucial to the width of peripheral sealant after assembly, which not only affect the out-looking, but also critically affect the yield of the breaking process. Many factors influence the dispensing speed of the sealant, such as diameter of the nozzle hole, pressure of compressed air, moving speed of nozzle, distance between nozzle and

substrate, viscosity of sealant and even the quantity of sealant in the dispensing container, etc. The relationships between these factors and the dispensing speed are not linear. Moreover, some of these factors are difficult to control, such as the viscosity of sealant and the quantity of sealant in the dispensing container, as they keep on changing from time to time. Because of this, it is not possible to control the sealant dispensing speed by fixing all these factors.

To find an approach to measure the sealant dispensing speed is necessary. A simple yet effective method is adopted to solve this problem. A simple program is developed to make the nozzle dispense sealant continuously on a piece of glass for 100 seconds, the dispensed sealant can be weighted by a balance with resolving power of milligram, and thus the sealant dispensing speed can be easily calculated. Now that the sealant dispensing speed is known, the width of the peripheral sealant after hot press can be calculated. It has been proved that, so long as the specific gravity of the sealant and the vaporization of the solvent in the sealant are taken into consideration, the calculation result can be in good agreement with the experiment result.

The third problem is that, after finishing drawing, the sealant remained in the nozzle must be cleaned by ultrasonic bath in acetone several times. After that, the acetone remained in the nozzle was blown away by air gun. If this process is not done carefully, the nozzle would tend to be blocked, that means it is spoiled, as it is not possible to clean it and to use it again. All these troublesome can be avoided by using a simple method. This method is that, instead of dismantling the nozzle from the cylinder, just let the nozzle and the sealant cylinder be after using, and put them together into the refrigerator, and it can be directly used for the next time.

6.3 Improvement to the LC container used in LC filling process

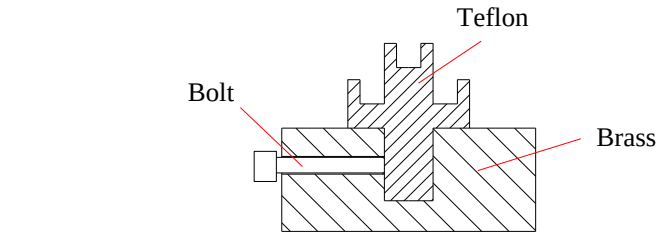

(a)

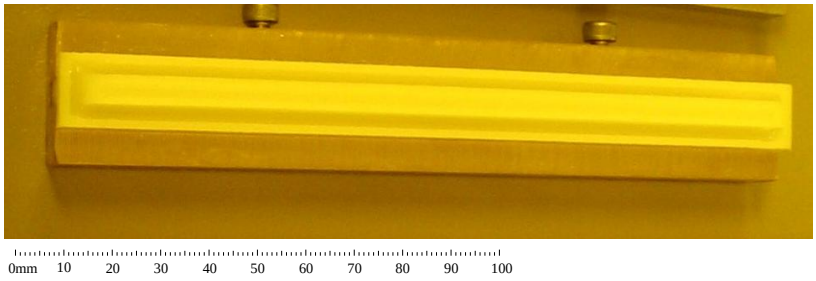

(b)

Fig. 6.7 (a) Cross section view of the new version LC container; (b) Photograph of the new designed LC container.

A special LC container as shown in Fig. 6.7, which was designed and machined by the author, was used in the LC filling process. The material for the LC container is Teflon, which has the advantages of perfect chemical-resistant property, easy to clean, and it will not damage glass due to its intrinsic softness. However, because of its intrinsic softness, it is difficult to remain its shape during machining and application. To solve this problem, it is designed to be fixed on a brass base using bolts.

In the process of LC filling, during the vacuum pumping period, the air melted in LC becomes bubbles and pushes LC to flow around. This causes the waste of LC material and the contamination of the facility. To solve this problem, another slot is designed surrounding the slot containing LC, and the overflowed LC can be reused.

6.4 Study of the bulge problem in cell gap control

6.4.1 Background and objectives

Liquid crystal cell gap is an important parameter for various kinds of liquid crystal devices. To obtain a uniform and desired cell gap is critical in the fabrication. Bulge of LC cells is a frequently encountered problem after hot press process. This problem seriously deteriorates the uniformity of cell gap. In this study, it is shown that the bulge problem of LC cell originates from the elastic deformation of spacers, rather than from the shrinkage of the sealant during temperature change or curing process. Based on this mechanism, several approaches to alleviate the bulge problem are studied experimentally. Experimental results show these approaches are effective, which further confirm the correctness of the proposed mechanism.

This study uses the normal fluorescent light to observe the cell gap uniformity. Comparing with using cell gap measurement instrument, the approach using fluorescent light is proved to be more intuitive and effective in the observing cell gap uniformity. Unlike sunlight or incandescence light, the line spectrum of fluorescent light is very narrow, indicating a longer coherence length. In fact, it is much longer than a normal LCD cell gap. This makes it possible to observe the cell gap uniformity through interference fringes formed by reflected beams from the two LC/glass interfaces. One can judge the cell gap uniformity by observing the number and density of the interference lines.

Though cell gap control can be well done nowadays, however, technologies related to cell gap control, such as the bulge problem discussed here, are seldom discussed in literatures.

6.4.2 Experiment Results

Fig. 6.8 shows the bulge problem of LC cell after hot press process. The spacers distributed in this LC cell are polymer spacer with diameter of 6 μm. The size of the whole substrate is 150 mm square. The hot press condition is 0.65 kg/cm^2, 150 ℃. This picture was taken under fluorescent lamp with black background. To improve the clarity of the interference lines, the contrast of the picture has been adjusted by an image process software.

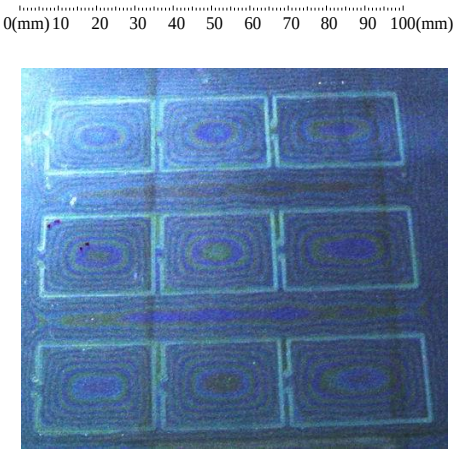

Fig. 6.8 LC cell without spacer mixed in sealant.

The interference lines clearly show that the cell is severely bulged. There are about 4 blue color interference lines from the peripheral sealant to the cell center. Assuming the wavelength of blue color is 0.45 μm, according to the principle of interference, it can be roughly estimated that the cell gap difference between cell center and peripheral sealant is about $4\times0.45/2=0.9$ μm. Using cell gap measurement instrument, it is measured that the cell gap at the filling hole is about 5.5 μm. From the distribution of interference lines shown in Fig. 6.8, it is ascertained that the cell gap at the filling hole is equal to the cell

gap at peripheral sealant. Therefore the cell gap at peripheral sealant is smaller than 6 μm, which is the diameter of the spacer used.

Based on these facts, the mechanism of the formation of LC cell bulge can be hypothesized, which is schematically shown in Fig. 6.9.

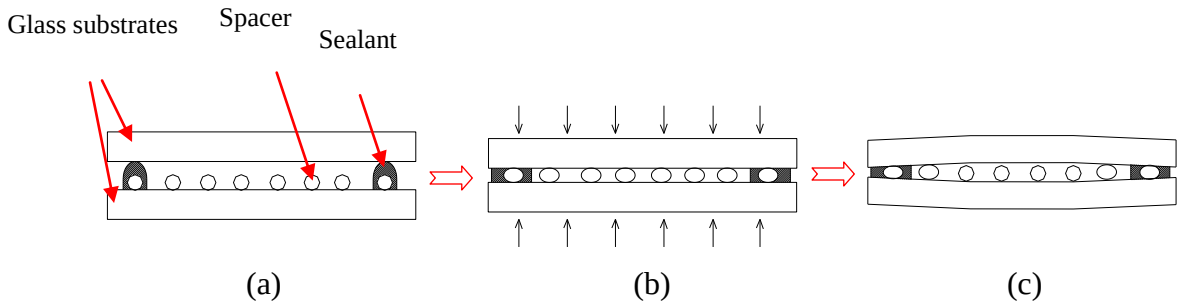

Fig. 6.9 (a) Before hot press; (b) During hot press; (c) After hot press.

Fig. 6.9(a) shows the assembled cell before hot press. Because spacers are uniformly dispensed on the whole substrate in the spacer dispensing process, there must be spacers in sealant as well. Fig. 6.9(b) depicts the situation during hot press process. During hot press process, the spacers are deformed into ellipsoid due to the external pressure. After hot press is completed, the external pressure exerted on substrates is released, and the spacers distributed in cell center resume their former shape, the cell gap becomes bigger after releasing the pressure. However, the cell gap within and near the peripheral sealant keeps unchanged due to the rigidity of the cured sealant. As the result, the cell gap at sealant position is smaller than spacer diameter, and the cell gap is larger than spacer diameter at cell center, which is depicted in Fig. 6.9(c).

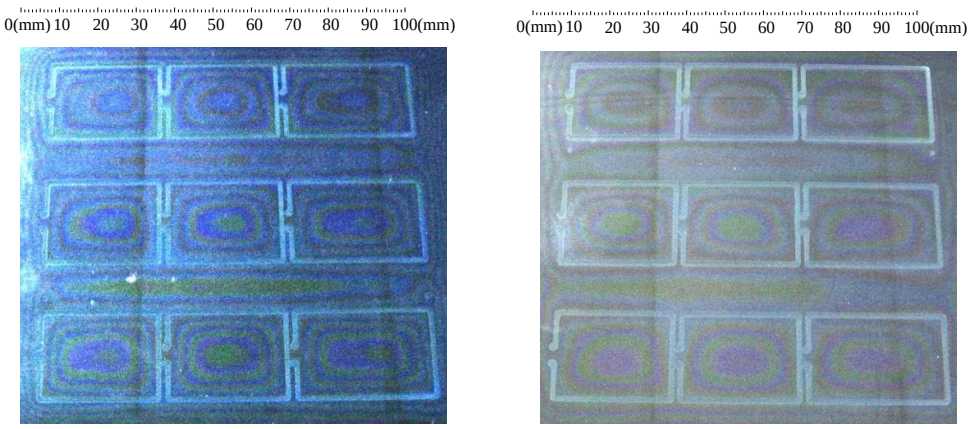

(a) (b)

Fig. 6.10 (a) LC cell with 2.5% 6 μm polymer spacer mixed in sealant curing at 150℃; (b) LC cell with 2.5% 6 μm polymer spacer mixed in sealant curing at 100℃.

Based on above assumption, several approaches to alleviate the bulge problem were tried. These approaches are: (1) Increasing spacer density in sealant by mixing spacer into sealant. This will reduce the deformation of spacer at peripheral sealant due to external pressure. The experiment result is shown in Fig. 6.10 (a), where the spacer mixed into sealant is the same type as the spacer distributed in cell center. The weight concentration is 2.5%. (It should be noted that all the spacers distributed in LC cell in following experiments is polymer material with diameter of 6 μm.) (2) As spacers become softer at high temperature, lower hot press temperature will reduce the deformation of spacers. After the external pressure is released, the cell can be put into oven to fully cure the sealant without applying any external pressure. In this approach, the temperature cannot be too low, or the sealant cannot lubricate well with substrate, and bubble will be generated between substrate and sealant. Here we reduce the temperature from the

standard 150℃to 100℃. The experiment result is shown in Fig. 6.10 (b), it can be seen that there is an improvement in uniformity comparing with Fig. 6.10 (a). (3) If the sealant is mixed with the same size glass fiber spacer, in the same condition of hot press, the cell uniformity would be better than mixing with the same size polymer spacer. This is because the rigidity of glass material is much higher than polymer material. The experiment result is shown in Fig. 6.11(a). (4) The polymer spacers mixed in sealant is a slightly larger than those distributed in cell. We mixed 2.5% 6.4 μm polymer spacers into sealant. Fig. 6.11 (b) shows the experiment result. (5) UV sealant can cure at room temperature, so the spacer in this case will be more rigid compared to hot press. Fig. 6.11 (c) shows the LC cell using UV curing sealant. Though there is no spacer mixed in sealant. The uniformity of the cell gap is quite good.

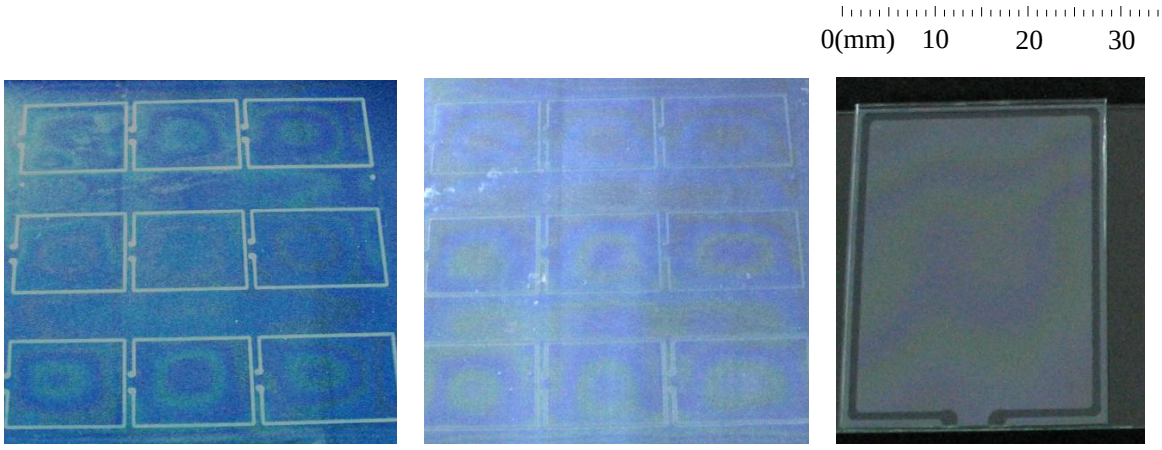

(a) (b) (c)

Fig. 6.11 (a) LC cell with 6 μm glass fiber mixed in sealant; (b) LC cell with 6.4 μm polymer spacer mixed in sealant; (c) LC cell using UV curing sealant.

6.4.3 Discussion

The above experimental results show that approaches (3), (4) and (5) can greatly improve the cell gap uniformity, while approaches (1) and (2) can also alleviate the bulge problem to some extent. All these approaches have value in practical applications. It is quite natural to think that reducing the external pressure during hot press process should also be an approach to alleviate the bulge problem. In fact, smaller pressure than 0.65 kg/cm^2 has been tried, but it is found that too small pressure is not enough to flatten the substrates. It should be mentioned that the glass substrates used in the experiments are for TN, so they are not as flat as those for STN.

It can be seen that the cell gap is still not perfect even utilizing the approaches of (3), (4) or (5). But in most cases, it is good enough. After filling liquid crystal, the cell gap uniformity will be further improved due to surface tension of liquid crystal [52]. Usually, for LC devices with high requirements in uniformity and stability of cell gap, an evenly distributed external force should be exerted on LC cell during end seal process. The absolute cell gap value will be affected by this force [53]. This process will further improve the uniformity and stability of cell gap.

6.4.4 Conclusion

To obtain a uniform and desired cell gap is critical in the fabrication of LC cells. Bulge of LC cells is a frequently encountered problem after hot press process. The mechanism of the formation of bulge is analyzed in this study. Several approaches are proved to be effective in alleviating the bulge problem experimentally. These approaches are practically

useful in the fabrication of LC cell. Moreover, the fluorescent light were used in observing cell gap uniformity. This interesting method is proved to be intuitive and effective.

Chapter 7 Studies of rotational frequency shift and orbital angular momentum with the help of LC SPP

7.1 Previous approaches to observe and measure the rotational frequency shift

Rotational frequency shift (RFS) arises from the relative rotational movement between optical vortices and the observer. As schematically shown in Fig. 7.1, the frequency observed by the observer is different from the emitted frequency of the optical vortex, this frequency difference is named rotational frequency shift.

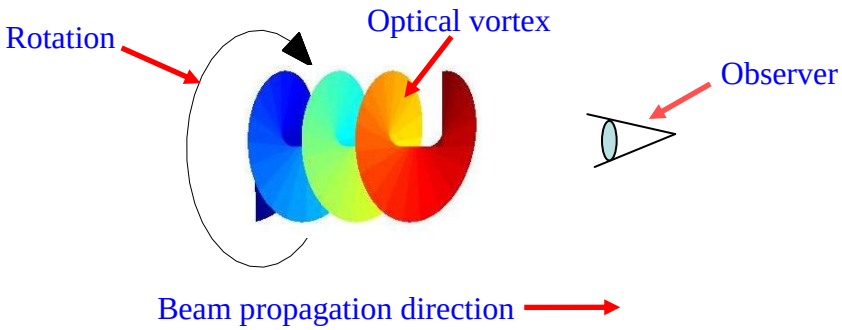

Fig. 7.1 RFS arises from the relative rotational movement between an optical vortex and the observer.

In reference 54, the RFS was first observed and measured in mm-wavelength, where the rotation of an optical vortex was realized by rotating a dove prism, and RFS was measured to be the scalar product of the frequency of the rotation and the topological

charger of the optical vortex, i.e., $\mathrm{RFS} = \frac{l\Omega}{2\pi}$, where Ω is angular frequency of the rotating vortex beam, and l is the topological charge of the optical vortex. However, due the intrinsic limitation in mechanical precision, the experiment setup in reference 54 can not be used in optical wavelength. In reference 55, a computer generated hologram was used to observe and measure RFS in optical wavelength, where the rotation of the optical vortex is realized by rotating a right angle prism.

7.2 Observation and measurement of RFS using the interference patterns of optical vortices generated by a LC SPP

The interference patterns between optical vortices and their coherent Gaussian beams were used to determine the topological charges of optical vortices previously [38]. This sort of interference pattern was also used to rotate optically trapped particles [39]. It is found that this interference pattern is actually a manifestation of RFS.

The experiment setup built to observe the interference patterns between optical vortices and their coherent Gaussian beams is the same as Fig. 3.5. And the interference pattern obtained for optical vortices with topological charges ranging from 1 to 6 are shown in Fig. 3.9(b), it can be seen clearly from the figure that, the radial spokes number of the interference pattern is equal to the topological charge of the optical vortex.

When a detector with a small off-axis aperture is rotating around the interference beam axis, the signal frequency detected should be the product of the rotational frequency of the detector $\Omega/2\pi$ and the radial spokes number ℓ, i.e., the topological charge of the optical vortex. Fig. 7.2 shows the diagram of the experiment setup to measure RFS of a

vortex beam and its coherent Gaussian beam using a detector with a small off-axis aperture. The beam diameter in the plane of aperture was measured to be 10 mm, the diameter of the aperture was 50 μm, which was 2 mm away from the center of the beam. The off-axis aperture was set into rotation with an angular velocity of 25 rpm.

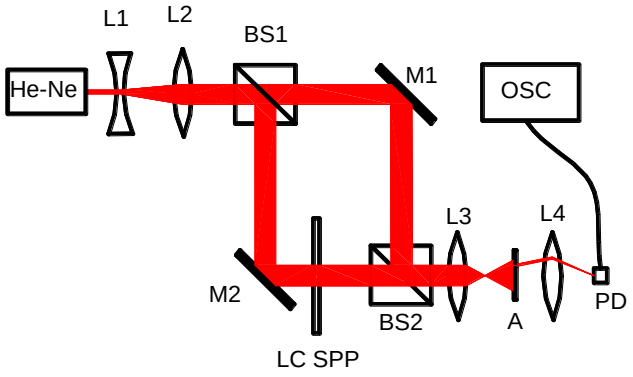

Fig. 7.2 Experimental setup for measuring RFS. PD is a photo detector; A is a rotating off-axis aperture; OSC is an oscilloscope;

Fig. 7.3 shows the photographs of the experiment setup. The mechanical parts of the rotational pin hole are designed and machined by the author. Fig. 7.4 shows the measured results. It can be seen clearly that the frequencies of the detected signal are equal to $\frac{l\Omega}{2\pi}$.

The frequency detected by the rotational detector with a small off-axis aperture should be the frequency difference between the optical vortex and the Gaussian beam. Since the Gaussian beam is symmetrical to rotational movement around its axis, its frequency seen by the rotational detector does not change, so it can be ascertained that the rotational frequency shift of the optical vortex beam is equal to $\frac{l\Omega}{2\pi}$, i.e. the product of

relative rotational frequency of the detector and topological charge of the vortex beam. Thus the interference patterns observed in Fig. 3.9(b) are actually the manifestation of rotational frequency shift.

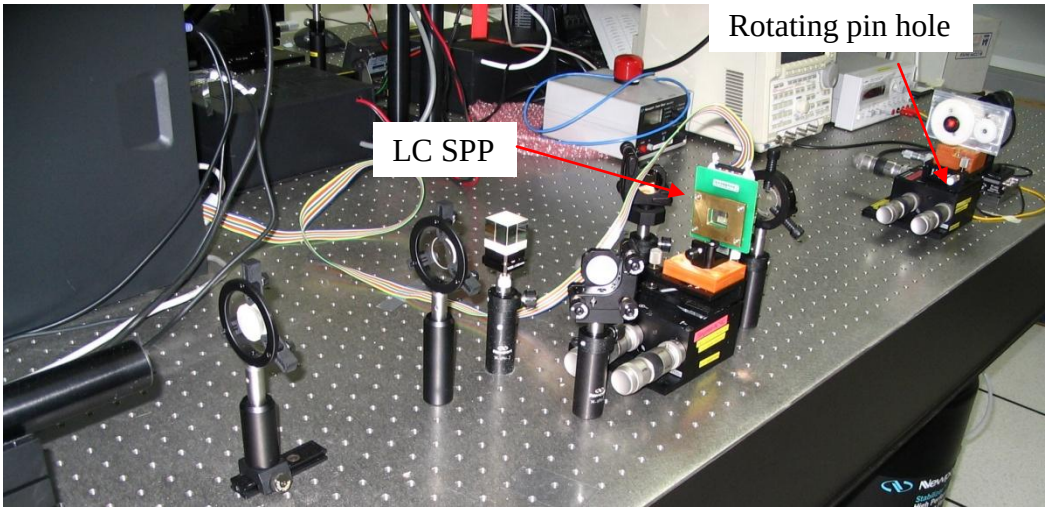

(a)

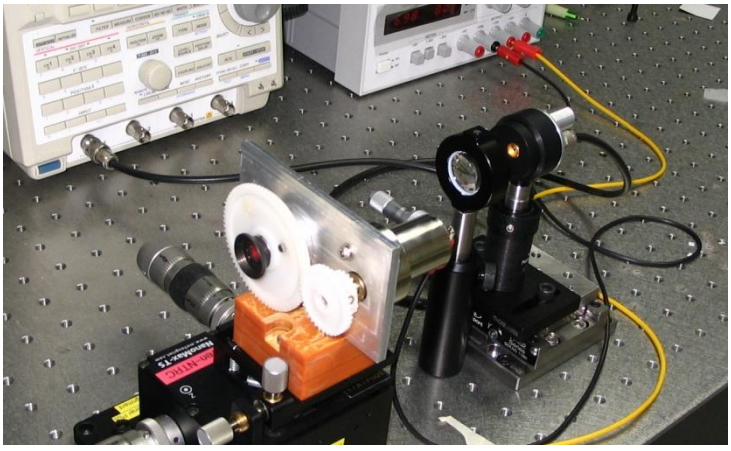

(b)

Fig. 7.3 (a) Photograph of the experimental setup for measuring RFS. (b) Close-up of the rotating pin hole and detector.

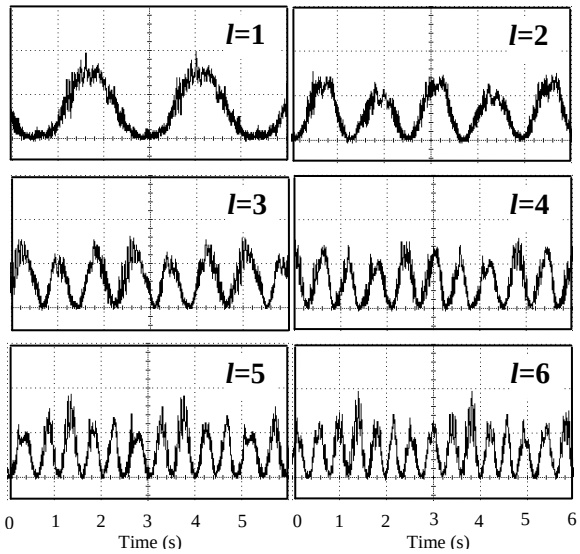

Fig. 7.4 Waveforms obtained for different topological charges ranging from 1 to 6.

Comparing with other experimental manifestations of RFS [54, 55], the experimental scheme described here is more straightforward for verification of RFS, as recording of the time progress of signal is not necessary for making the judgment. It is worth mentioning that, this result is obtained by rotating detector and keeping light beam still rather than rotating light beam and keep the detector still in other experiments, so from the other side, it is ascertained that rotational frequency shift arises from the relative rotational movement between light beam and observer.

7.3 Determination of OAM of the photon of optical vortices through RFS

It has been theoretically deduced by Allen *et al.* that a Laguerre-Gaussian (LG) beam, an optical vortex, possesses a well defined OAM of $l\hbar$ per photon [32] where l is the topological charge, as shown in the reference, the deduction process is a long story. A way

to verify that the OAM of LG beam is equal to $l\hbar$ experimentally has been proposed, which is similar to Beth's experiment [56], i.e., using a precise torsion balance to measure the torque exerted on a pair of cylindrical lenses [32]. In fact, instead of using cylindrical lenses, there are other choices, such as using a spiral phase plate or simply a mirror, so long as it can change OAM of an incident light beam. However, due to the high precision requirements to the experiment, this verification is extremely challenging [57]. So far, actually, no quantitative measurement of the exerted torque has been reported. Although some experiments have been successfully carried out in observing the transformation of OAM to matter [58], the quantitative relationship between photon and the torque exerted is almost impossible to be determined precisely in these experiments. Leach *et al.* reported the measurement of the OAM of a photon [59], where the OAM spectrum of a photon rather than the OAM was determined.

In this section, a simple method to determine the OAM from RFS is proposed. Since the existence of RFS, the energy of a photon of the optical vortex detected by the rotational detector is changed; and the energy change of each photon is equal to the product of Plank's constant and the RFS, i.e. $h(\frac{l\Omega}{2\pi})$. So there must be energy exchange between the light beam and the rotational detector. On the rotational detector side, we assume there are n photons being detected during a time interval Δt, during which the detector rotated by an angle of $\Delta\theta$ $(\Delta\theta = \Omega\Delta t)$. If the OAM of each photon is M, the change of the angular momentum of the detector is nM, and the external torque exerted on the detector (the rate of change of angular momentum [60]) is $\frac{nM}{\Delta t}$. When this torque

acts on the detector that undergoes an angular displacement, the torque does work on the detector; and the work can be expressed as the product of the torque and the angular displacement, i.e. $\frac{nM}{\Delta t}\cdot\Delta\theta = nM\Omega$. On the other hand, according to energy conservation law, the work done to the detector should be equal to the energy change of the photons, which is $nh(\frac{l\Omega}{2\pi})$. So we have

$$nh(\frac{l\Omega}{2\pi}) = nM\Omega \tag{7.1}$$

Then $M = l\hbar$ can be easily obtained. It is worth mentioning that this result is based on the measurement result of RFS and the energy conservation law. In a certain point of view, this approach can be regarded as an experimental verification of OAM.

7.4 Generally existing relationship between the momentum and the frequency shift of a photon

The idea introduced in previous section is found applicable to other kinds of frequency shift, i.e., the Doppler frequency shift and the frequency shift arises from the rotation of a circularly polarized light beam.

In fact, it is easy to verify that the observed frequency of Doppler shift is

$$f' = \frac{c + v_r}{c} f \tag{7.2}$$

where f' is the observed frequency, f is the emitted frequency, c is the velocity of the light beam, v_r is the velocity of the observer, here the velocity of the light source is

assumed to be zero. Assuming the momentum of each photon is M , and during a time interval of Δt , n photons are received by the observer, and the work done by the photons to the observer in Δt is $\frac{nM}{\Delta t} \cdot v_r \cdot \Delta t$. Considering Eq. 7.2, the change of the energy of those photons is $nh\frac{v_r}{c} \cdot \frac{c}{\lambda}$. According to the energy conservation law, we have

$$\frac{nM}{\Delta t} \cdot v_r \cdot \Delta t = nh\frac{v_r}{c} \cdot \frac{c}{\lambda} \tag{7.3}$$

Then it is easy to obtain $M = \frac{h}{\lambda}$, and this result is consistent with quantum theory and electromagnetic theory.

In the case of rotational circularly polarized light, the frequency shift was measured in the experiment shown in reference 67, by applying the same idea introduced above, the angular momentum of the photon of the circularly polarized light can be determined as $\hbar$.

From above results, it can be seen that there is an intrinsic and well defined relationship existing between the momentum and frequency shift of a photon, and from this point of view, any frequency shift arising from a motion is always accompanied by a momentum of the photon in that motion direction, and the quantity of the frequency shift and the momentum can be mutually determined.

7.5 Summary

In summary, it is discovered that the interference patterns between optical vortices and their coherent Gaussian beam are actually a sort of manifestation of rotational frequency shift (RFS). Furthermore, based on the value of RFS obtained in experiment,

and by use of the energy conservation law, it can be ascertained that the OAM of a photon of optical vortices is equal to $l\hbar$. This approach is different and simpler then the hitherto existed ways to determine the OAM of the photon of optical vortices. This idea is also applicable to the cases of Doppler frequency shift and frequency shift caused by rotational circularly polarized light beams. This further implies a generally existing relationship between the momentum and the frequency shift of a photon, and from this point of view, any frequency shift arising from a motion is always accompanied by the work done by the momentum of the photons in that motion direction, and the quantity of the frequency shift and the momentum can be mutually determined.

Chapter 8 Conclusions and Recommendations

8.1 Conclusions

(1) Three types of LC SPP with improving performance have been designed, fabricated and tested. The third type of LC SPP has the best performance. The unique advantages of LC SPP such as generation and dynamic switching of OV with different topological charge, adaptability to any visible wavelength are realized.

(2) The mechanism of the conversion efficiency degradation of LC SPP was experimentally studied, and solution to this problem was proved effective. The phenomena of discreteness and distortion of the optical vortices generated by LC SPP were observed, and the explanations based on experimental and simulation results were given. The relationship between the total slice number and the purity of topological charge of optical vortices generated by multi-level SPP was found through Fourier analysis..

(3) A batch fabrication process of LC SPP was developed based on the existing LCD fabrication line. Some improvements are made to the existing machine and process, such as the glass scribing process, sealant drawing process etc.

(4). An automatic measurement system based on a Michelson interferometer with a linear photo detector array was developed to measure the phase shift versus driving voltage of LC SPP. A trough position method was used in the data processing, and the measurement standard deviation can reach 0.1 º. Besides, the thermal drift and non-thermal drift of the measurement system was observed, and this system was applied

to the measurement of micro-displacement of piezoelectric mirror and the phase shift versus driving voltage of a polymer dispersed liquid crystal cell.

(5). The rotational frequency shift (RFS) was observed and measured through the interference pattern of optical vortices generated by LC SPP. It is pointed out that the interference patterns between optical vortices and the coherent Gaussian beam are actually the manifestation of RFS, and the orbital angular momentum of the photon of optical vortices can be determined based on RFS and the energy conservation law. Further, it is found that any frequency shift arising from a motion is always accompanied by the work done by the momentum of the photons in that motion direction, and the quantity of the frequency shift and the momentum can be mutually determined.

8.2 Recommendations

8.2.1 Applications of LC SPP

Comparing with other kinds of SPP, the LC SPP has some unique advantages, such as capable to generate different topological charge and applicable to any visible wavelength and easy to realize high slice numbers for obtaining optical vortices with purer topological charge. To explore the applications of LC SPP in optical trapping, generating radially polarized beams, edge contrast enhancement in microscopy, optical vortex coronagraph and any other possible field is meaningful.

For example, the switchability between different topological charges may be found useful in following applications. (1). For optical tweezers, the size of dark center of

optical vortices can be adjusted to adapt to particles with different size; switching between optical vortices with different topological charge may change the rotating speed and rotating direction of a trapped particle. The short switching time between different topological charges will prevent the trapped particle from escape due to Brownian motion. (2). For the edge contrast enhancement in microscopy, it has been proposed that spiral phase with higher topological charge may enable microscopy more sensitive to small phase jump. (3). For the optical vortex coronagraph, through the switchability between different topological charges may get the optimized image for parent stars with different distance in between them. Besides, the optical vortices with fractional topological charge are multi-dimensional entanglement states which have attracted some research interests; LC SPP is especially convenient in generation optical vortices with various values of fractional topological charge, which may find application in this research area.

8.2.2 Other types of LC SPP

It is possible to get some other types of LC SPP with some unique advantages.

1. LC SPP have faster response time

By use of the structure in the third type LC SPP, optical vortices with high topological charge may be achievable by using thin cell gap LC cell, such as 7 μm. This can be explained as following: Assuming the whole azimuthal angle range is evenly divided into l parts, l is the topological charge of the optical vortex to be realized. For the azimuthal angle θ is within the arc of $\left(\frac{2\pi}{l}(n-1), \frac{2\pi n}{l}\right)$, where n is any positive

integer, and $n \le l$. If the phase shift in this range is $l\theta - 2\pi(n-1)$, then it is equivalent to $l\theta$. Since $l\theta - 2\pi(n-1)$ is actually changed from 0 to 2π within each arc, so the total dynamic range of phase shift of 2π is sufficient. Therefore LC cells with thin cell gap can be employed, and this will improve the response time.

On the other hand, this type of LC SPP has shortcoming, since the driving voltage value is not continuously across the interface of adjacent arcs, the fringe field effect will disturb the alignment of liquid crystal molecules, and they will scattering the light beam. This reduces the conversion efficiency and the beam quality of optical vortex to some degree.

2. Reducing gap between adjacent slices and increasing total slice number

As depicted in section 3.5, the purity of the optical vortex generated from SPP is determined by the total slice number. To get optical vortices with high purity, a large total slice number is indispensable. However, with the increase of total slice number, the null area in the center of SPP will also be increased. This problem can only be alleviated by reducing the gap between adjacent slices. If a modern semiconductor lithography procedure is employed to pattern the ITO layer, then sub-micrometer gap between adjacent slices can be realized, and a near perfect LC SPP with hundreds of slices may be fabricated. To reduce the connecting terminal for driving, the thin-film-transistor (TFT) may be employed to drive each slice.

Bibliography

[1] N. B. Simpson, K. Dholakia, L. Allen, and M. J. Padgett, "Mechanical equivalence of spin and orbital angular momentum of light: an optical spanner," Opt. Lett. **22**, 52 (1997).

[2] E. Santamato, A. Sasso, B. Piccirillo, and A. Vella, "Optical angular momentum transfer to transparent isotropic particles using laser beam carrying zero average angular momentum," Opt. Express **10**, 871 (2002).

[3] K. T. Gahagan and G.. A. Swartzlander, "Optical vortex trapping of particles," Opt. Lett. **21**, 827 (1996).

[4] Y. Song, D. Milam, and W. T. Hill, "Long, narrow all-light atom guide," Opt. Lett. **24**, 1805 (1999).

[5] X. Xu, K. Kim, W. Jhe, and N. Kwon, "Efficient optical guiding of trapped cold atoms by a hollow laser beam," Phy. Rev. A **63**, 3401 (2001).

[6] T. Kuga, Y. Tori, N. Shiokawa, T. Hirano, Y. Shimizu, and H. Sasada, **"**Novel Optical Trap of Atoms with a Doughnut Beam," Phys. Rev. Lett. **78**, 4713 (1997).

[7] I. Bialynicki-Birula and Z. Bialynicka-Birula, "Rotational frequency shift," Phys. Rev. Lett. **78**, 2539 (1997).

[8] J. Courtial, D. A. Robertson, K. Dholakia, L. Allen, and M. J. Padgett, "Rotational Frequency Shift of a Light Beam," Phys. Rev. Lett. **81**, 4828 (1998).

[9] J. Courtial, K. Dholakia, D. A. Robertson, L. Allen, and M. J. Padgett, "Measurement of the Rotational Frequency Shift Imparted to a Rotating Light Beam Possessing Orbital Angular Momentum," Phys. Rev. Lett. **80**, 013601 (1998).

[10] K. Dholakia, N. B. Simpson, and M. J. Padgett, "Second-harmonic generation and the orbital angular momentum of light," Phys. Rev. A **54**, 5 (1996).

[11] C. Tamm and C. O. Weiss, "Bistability and optical switching of spatial patterns in a laser," J. Opt. Soc. Am. B **7**, 1034 (1990).

[12] A. Mair, A. Vaziri, G. Weihs, and A. Zeilinger, "Entanglement of the orbital angular momentum states of photons," Nature **412**, 313 (2001).

[13] N. R. Heckenberg, R. G.. Mcduff, C. P. Smith, and A. G.. White, "Generation of optical phase singularities by computer-generated holograms," Opt. Lett. **17**, 221 (1992).

[14] J. Courtial and M. J. Padgett, "Performance of a cylindrical lens mode converter for producing Laguerre–Gaussian laser modes," Opt. Comm. **159**, 13 (1999).

[15] M. Harris, C. A. Hill, P. R. Tapster, and J. M. Vaughan, "Laser modes with helical wave fronts," Phys. Rev. A **49**, 3119 (1994).

[16] S. C. Tidwell, D. H. Ford, and W. D. Kimura, "Generating radially polarized beams interferometrically," Appl. Opt. **29**, 2234 (1990).

[17] S. Furhapter, A. Jesacher, S. Bernet, and M. Ritsch-Marte, "Spiral phase contrast imaging in microscopy," Opt. Express **13**, 689 (2005)

[18] G. Foo, D. M. Palacios, and G. A. Swartzlander, "Optical vortex coronagraph," Opt. Lett. **30**, 3308 (2005)

[19] M. W. Beijersbergen, R. P. C. Coerwinkel, M. Kristensen, and J. P. Woerdman, "Helical-wavefront laser beams produced with a spiral phase plate," Opt. Comm. **112**, 321 (1994).

[20] R. Oron, N. Davidson, A. A. Friesem, and E. Hasman, "Efficient formation of pure helical laser beams," Opt. Comm. **182**, 205 (2000).

[21] A. G. Peele, P. J. McMahon, D. Paterson, C. Q. Tran, A. P. Mancuso, K. A. Nugent, J. P. Hayes, E. Harvey, B. Lai, and I. McNulty, "Observation of an x-ray vortex," Opt. Lett. **27**, 1752 (2002).

[22] S. S. R. Oemrawsingh, E. R. Elie, J. P. Woerdman, E. J. K. Verstegen, J. G. Kloosterboer, and G. W. Hooft, "Half-integral spiral phase plates for optical wavelengths," J. Opt. A: Pure Appl. Opt. **6**, S288–S290 (2004).

[23] C. Rotschild, S. Zommer, S. Moed, O. Hershcovitz, and S. G. Lipson, "Adjustable spiral phase plate," Appl. Opt. **43**, 2397 (2004).

[24] X. C. Cheong, W. M. Lee, X. C. Yuan, and L. S. Zhang, "Direct electron-beam writing of continuous spiral phase plates sin negative resist with high power efficiency for optical manipulation," Appl. Phys. Lett. **85**, 5784 (2004).

[25] K. Sueda, G. Miyaji, N. Miyanaga, and M. Nakatsuka, "Laguerre-Gaussian beam generated with a multilevel spiral phase plate for high intensity laser pulses," Opt. Express **12**, 3548 (2004).

[26] K. Ganic, X. Gan, M. Gu, M. Hain, S. Somalingam, S. Stankovic, and T. Tschudi, "Generation of doughnut laser beams by use of a liquid-crystal cell with a conversion efficiency near 100%," Opt. Lett. **27**, 1351 (2002).

[27] M. Vasnetsov and K. Staliunas, *Optical Vortices*, Nova Science Publishers, Inc. (1999).

[28] A. E. Siegman, *Lasers*, chapter 16, (University Science Books, c1986).

[29] I. Kimel and L. R. Elias, "Relations between Hermite and Laguerre Gaussian modes," IEEE Journal of quantum electronics **29**, 2562 (1993).

[30] M. Abramowitz and I. A. Stegun, *Handbook of Mathematical Functions*, Dover, New York, 799-802, 1965.

[31] J. Hawkes and I. Latimer, *Lasers theory and practice*, (Prentice Hall International, UK, 1995).

[32] L. Allen, M. W. Beijersberjen, R. J. C. Spreeuw, and J. P. Woerdman, "Orbital angular momentum of light and the transformation of Laguerre Gaussian laser modes," Phys. Rev. A **45**, 8185(1992).

[33] M. J. Padgett and L. Allen, "The Poynting vector in Laguerre-Gaussian laser modes," Opt. Comm. **121,** 3640 (1995)

[34] E. Kaneko, *Liquid crystal TV displays : principles and applications of liquid crystal displays*, KTK Scientific Publishers (1987).

[35] D. K. Yang and S. T. Wu, *Fundamentals of liquid crystal devices*, John Wiley (2006).

[36] V. G. Chigrinov, *Liquid crystal devices : physics and applications*, Artech House (1999)

[37] On line http://pda.physorg.com/lofi-news-light-mask-optical_11286.html

[38] A. G. White, C. P. Smith, N. R. Heckenberg, H. Rubinsztein-Dunlop, R. McDuff, C. Weiss, and C. Tamm, "Interferometric measurements of phase singularities in the output of a visible Laser," J. Mod. Opt. **38**, 2531 (1991).

[39] L. Paterson, M. P. MacDonald, J. Arlt, W. Sibbett, P. E. Bryant, and K. Dholakia, "Controlled Rotation of Optically Trapped Microscopic Particles," Science **292**, 912 (2001).

[40] Q. Wang, X. W. Sun, P. Shum, and X. J. Yin, "Dynamic switching of optical vortices with dynamic gamma-correction liquid crystal spiral phase plate," Opt. Express **13**, 10285 (2005).

[41] Q. Wang, X. W. Sun, and P. Shum, "Generating doughnut-shaped beams with large charge numbers by use of liquid-crystal spiral phase plates," Appl. Opt. **43**, 2292 (2004).

[42] J. E. Curtis and D. G. Grier, “Structure of Optical Vortices,” Phys. Rev. Lett. **90**, 13901 (2003).

[43] I. V. Basistiy, V. Yu. Bazhenov, M. S. Soskin, and M. V. Vasnetsov, “Optics of light beams with screw dislocations,” Opt. Comm. **103**, 422 (1993).

[44] On line http://www.engineeringtoolbox.com/linear-expansion-coefficients-d_95.html

[45] K. Lu and B. E. A. Saleh, “Theory and design of the liquid crystal TV as an optical spatial phase modulator,” Opt. Eng. **29**, 240 (1990);

[46] D. Bonaccini, G. Brusa-Zappellini, S. Esposito, P. Salinari, P. Stefanini, and V. Biliotti, “Adaptive optics wavefront corrector using addressable liquid crystal retarders: II,” in Active and Adaptive Optical Components, M. A. Ealey, ed., Proc. SPIE **1543**, 133 (1991);

[47] G. D. Love, “Wave-front correction and production of Zernike modes with a liquid-crystal spatial light modulator,” Appl. Opt. **36**, 1517 (1997);

[48] L. Hu, X. Li, Y. Liu, Z. Cao, D. Li, and Q. Q. Mu, “Phase-only liquid-crystal spatial light modulator for wave-front correction with high precision,” Opt. Express **12**, 64043 (2004);

[49] A. Michalkiewicz, M. Kujawinskaa, T. Kozackia, X. Wang, P. J. Bosb, “Holographic three-dimensional displays with liquid crystal on silicon spatial light modulator,” Interferometry XII: Techniques and Analysis, edited by Katherine Creath, Joanna Schmit, Proceedings of SPIE Vol. 5531 (SPIE, Bellingham, WA, 2004);

[50] S. J. Hwang, “Precise Optical Retardation Measurement of Nematic Liquid Crystal Display Using the Phase-Sensitive Technique,” IEEE/OSA Journal of Display Technology **1**, No.1, 77 (2005);

[51] P. A. Williams, A. H. Rose, and C. M. Wang, “Rotating-polarizer polarimeter for accurate retardance measurement,” Appl. Opt. **36**, 6466 (1997)

[52] N. Koshida, H Miyagi, and S. Kikui, "Cell gap uniformity of large-area liquid crystal display devices," Oyo Buturi **51**, 1304 (1982).

[53] J. P. M. Damen, "Calculation and measurement of the cell gap in liquid-crystal displays subjected to an external pressure," Journal of the Society for Information Display **3**, 23 (1995).

[54] J. Courtial, K. Dholakia, D. A. Robertson, L. Allen, M. J. Padgett, "Measurement of the Rotational Frequency Shift Imparted to a Rotating Light Beam Possessing Orbital Angular Momentum," Phys. Rev. Lett. **80**, 3217 (1998).

[55] I. V. Basistiy, V. V. Slyusar, M. S. Soskin, and M. V. Vasnetsov, "Manifestation of the rotational Doppler effect by use of an off-axis optical vortex beam," Opt. Lett. **28**, 1185 (2003).

[56] R. A. Beth, "Mechanical detection and measurement of the angular momentum of light," Phys. Rew. **50**, 115 (1936).

[57] M. J. Padgett, "Orbital angular momentum, optical spanners and the rotational frequency shift," In Laser Resonators III, Alexis V. Kudryashov and Alan H. Paxton, eds., Proc. of SPIE **3930**, 130-143 (2000)

[58] H. He, M. E. J. Friese, N. R. Heckenberg, and H. Rubinsztein-Dunlop, "Direct observation of transfer of angular momentum to absorptive particles from a laser beam with a phase singularity," Phy. Rev. Lett. **75**, 826 (1995).

[59] J. Leach, M. J. Padgett, S. M. Barnett, S. Franke-Arnold, and J. Courtia1, "Measuring the Orbital Angular Momentum of a Single Photon," Phy. Rev. Lett. **88**, 257901 (2002).

[60] H. D. Young and R. A. Freedman, *University Physics* Pearson Education, Inc. 2004.

[61] On line http://www.crystec.com/joyscre.htm

[62] S. T. Wu, U. Efron, and L. D. Hess, "Birefringence measurements of liquid crystals," Appl. Opt. **23**, 3911 (1984).

[63] S. Nakadate, "Phase detection of equidistant fringes for highly sensitive optical sensing. I. Principle and error analyses," J. Opt. Soc. Am. A **5**, 1258 (1988).

[64] S. Nakadate, "Phase detection of equidistant fringes for highly sensitive optical sensing. II. Experiments," J. Opt. Soc. Am. A **5**, 1265 (1988).

[65] J. H. Yi, S. H. Kim, Y. K. Kwak, and Y. W. Lee, "Peak movement detection method of an equally spaced fringe for precise position measurement," Opt. Eng. **41**, 428 (2002).

[66] Z. Wang, M. S. Graca, P. J. Bryanston-Cross, and D. J. Whitehouse, "Phase-shifted image matching algorithm for displacement measurement," Opt. Eng. **35**, 2327 (1996).

[67] B. A. Garetz and S. Arnold, "Variable frequency shifting of circularly polarized laser radiation via a rotating half-wave retardation plate," Opt. Comm. **31**, 1 (1979).

Author's Publications

Journal Papers:

1. Q. Wang, X. W. Sun, and P. Shum, "Generating doughnut-shaped beams with large charge numbers by use of liquid-crystal spiral phase plates," Appl. Opt. **43**, 2292 (2004).
2. Q. Wang, X. W. Sun, P. Shum, and X. J. Yin, "Dynamic switching of optical vortices with dynamic gamma-correction liquid crystal spiral phase plate," Opt. Express **13**, 10285 (2005).
3. Q. Wang, X. W. Sun, and P. Shum, "High azimuthal index doughnut beam generated by liquid crystal spiral phase plate," ACTA OPTICA SINICA **23**, Supplement 859 (2003).
4. Q. Wang, X. W. Sun, P. Shum, and X. J. Yin, "Manifestation of rotational frequency shift and verification of orbital angular momentum through interference patterns of optical vortices," submitted to Journal of Modern Opt.
5. Q. Wang, X. W. Sun, and X. J. Yin, "Equidistant fringe phase shift measurement system using trough position data processing method," submitted to Appl. Opt.
6. Y. J. Liu, X. W. Sun, and Q. Wang, "A focus-switchable lens made of polymer-liquid crystal composite," Journal of Crystal Growth **288**, 192 (2006).
7. Y. J. Liu, X. W. Sun, Q. Wang, and D. Luo, "Electrically switchable optical vortex generated by a computer-generated hologram recorded in polymer-dispersed liquid crystals," Optics Express **15**, 16645 (2007)

Conference Papers:

8. Q. Wang and X. W. Sun, "Generalized optimization of reflective liquid crystal display for direct-view and single-panel projection applications," SID International Symposium 2005 (May 22-27, Boston, MA, U.S.A. 2005)
9. Q. Wang and X. W. Sun, "LC cell bulging after hot press process," Asia Display International Symposium 2007 (Mar. 12~15, ShangHai, China).
10. Q. Wang, X. W. Sun, and X. J. Yin, "Measurement of phase shift of LC retarder using Michelson interferometer with linear photodiode array detector," The 10th Asian Symposium on Information Display (ASID'07) 2007 (August 1-4, Singapore).

Appendix A: Program for driving the third type LC SPP

```
‘This program is written in Visual Basic 6.0.
---------------------------------------------------------------------------------------------------------
Option Explicit
Dim wInitialCode As Integer, CHN As Integer
Dim wRtn As Integer, n As Long
Dim wSelectBoard As Integer, k As Integer
Dim V(15) As Single, VI(1 To 6, 0 To 15) As Single
Dim stopclick As Boolean, timestop As Boolean
---------------------------------------------------------------------------------------------------------
‘to initialize PIODA-16 multi-voltage output card.
Private Sub Form_Load()
Dim wtotalboards As Integer
   wInitialCode = PIODA_DriverInit()
   If wInitialCode <> PIODA_NoError Then
      wRtn = MsgBox("Driver Open Error !!!")
      CmdStart.Enabled = False
      Exit Sub
   Else
      CmdStart.Enabled = True
   End If
   wRtn = PIODA_SearchCard(wtotalboards, PIO_DA)
   If (wRtn <> PIODA_NoError) Then
      MsgBox ("Search Card Error!!" + Chr(13) + "Error Code:" + Str(wRtn))
      CmdStart.Enabled = False
   Else
      CmdStart.Enabled = True
   End If
End Sub

---------------------------------------------------------------------------------------------------------
Private Sub CmdStart_Click()
```

```
Dim s As Integer, t As Integer
stopclick = False
timestop = False
CHN = Val(txtChannel.Text)   'The multi-output channel value

'To assign the driving voltage to an array VI for topological charge 1 to topological charge 6. The voltages are determined from the polynomial formula, which is obtained by the curve fitting of the retardation versus voltage curve.

VI(1, 0) = 2.1562
VI(1, 1) = 2.1913
VI(1, 2) = 2.2299
VI(1, 3) = 2.2715
VI(1, 4) = 2.3157
VI(1, 5) = 2.3617
VI(1, 6) = 2.4087
VI(1, 7) = 2.456
VI(1, 8) = 2.5036
VI(1, 9) = 2.5517
VI(1, 10) = 2.6014
VI(1, 11) = 2.6546
VI(1, 12) = 2.7141
VI(1, 13) = 2.7829
VI(1, 14) = 2.8645
VI(1, 15) = 2.9615

VI(2, 0) = 1.5351
VI(2, 1) = 1.5687
VI(2, 2) = 1.6006
VI(2, 3) = 1.6301
VI(2, 4) = 1.6578
VI(2, 5) = 1.6863
VI(2, 6) = 1.7187
VI(2, 7) = 1.7574
VI(2, 8) = 1.8025
VI(2, 9) = 1.8522
VI(2, 10) = 1.9032
VI(2, 11) = 1.9524
VI(2, 12) = 1.999
VI(2, 13) = 2.0451
VI(2, 14) = 2.0957
VI(2, 15) = 2.1562

VI(3, 0) = 1.3249
VI(3, 1) = 1.3688
```

VI(3, 2) = 1.4073
VI(3, 3) = 1.4441
VI(3, 4) = 1.4862
VI(3, 5) = 1.5351
VI(3, 6) = 1.5849
VI(3, 7) = 1.6301
VI(3, 8) = 1.6718
VI(3, 9) = 1.7187
VI(3, 10) = 1.7792
VI(3, 11) = 1.8522
VI(3, 12) = 1.9281
VI(3, 13) = 1.999
VI(3, 14) = 2.0695
VI(3, 15) = 2.1562

VI(4, 0) = 1.1308
VI(4, 1) = 1.1953
VI(4, 2) = 1.2364
VI(4, 3) = 1.2811
VI(4, 4) = 1.34
VI(4, 5) = 1.395
VI(4, 6) = 1.4441
VI(4, 7) = 1.5019
VI(4, 8) = 1.5687
VI(4, 9) = 1.6301
VI(4, 10) = 1.6863
VI(4, 11) = 1.7574
VI(4, 12) = 1.8522
VI(4, 13) = 1.9524
VI(4, 14) = 2.0451
VI(4, 15) = 2.1562

VI(5, 0) = 1.1308
VI(5, 1) = 1.2073
VI(5, 2) = 1.2565
VI(5, 3) = 1.3249
VI(5, 4) = 1.395
VI(5, 5) = 1.4573
VI(5, 6) = 1.5351
VI(5, 7) = 1.6157
VI(5, 8) = 1.6863
VI(5, 9) = 1.7792
VI(5, 10) = 1.9032
VI(5, 11) = 2.0219
VI(5, 12) = 2.1562
VI(5, 13) = 2.3617
VI(5, 14) = 2.6014
VI(5, 15) = 2.9615

```
VI(6, 0) = 1.0002
VI(6, 1) = 1.1065
VI(6, 2) = 1.2016
VI(6, 3) = 1.2621
VI(6, 4) = 1.3474
VI(6, 5) = 1.4254
VI(6, 6) = 1.5101
VI(6, 7) = 1.6082
VI(6, 8) = 1.6939
VI(6, 9) = 1.8146
VI(6, 10) = 1.9643
VI(6, 11) = 2.1097
VI(6, 12) = 2.3385
VI(6, 13) = 2.6274
VI(6, 14) = 3.1396
VI(6, 15) = 4.1513

n = Val(txtPeriod.Text) * 4000  'loop times for time delay
‘to execute the dynamic switching.
Do
   For t = 1 To 6
      For s = 0 To CHN
         V(s) = VI(t, s)
      Next
      timestop = False
      Call voltageout
   Next
Loop Until stopclick = True
End Sub
```

```
‘to output voltage stored in V(k) to channels
Private Sub voltageout()
Do

   'To output corresponding positive voltage to every channel.

   For k = 0 To CHN

   PIODA_CalVoltage wSelectBoard, k, V(k)

   Next

   Call timedelay

   'To output corresponding positive voltage to every channel.

   For k = 0 To CHN

   PIODA_CalVoltage wSelectBoard, k, -V(k)

   Next

   Call timedelay

   DoEvents
```

```
Loop Until timestop = True
End Sub
---------------------------------------------------------------------------------------------------------
'To determine the period of the driving signal.
Private Sub timedelay()
Dim j As Long, m As Integer
For j = 1 To n
   m = m + 1
   m = m - 1
Next
End Sub
```

```
‘Using timer to control the time interval for each topological charge.
Private Sub Timer1_Timer()
timestop = True
End Sub
-------------------------------------------------------------------------
‘Using “CmdStop” button to stop the program
Private Sub CmdStop_Click()
stopclick = True
End Sub
---------------------------------------------------------------------------------------------------------
‘to use “exit” button to exit the program.
Private Sub exit_Click()
Unload Me
End Sub
---------------------------------------------------------------------------------------------------------
```

Appendix B: Program for data acquisition and data processing of the phase shift measurement system

(a). Visual Basic source code for the data acquisition of the measurement in Fig. 4.9(c)

```
    Dim i, j As Long
    Dim reading() As Byte
    Dim wavedata() As Byte
    Dim vdiv, acqsize As Single
    Dim fnum, v As Integer
    Dim voltage() As Single
    Dim exitclick As Boolean

Private Sub Form_Load()
-------------------------------------------
    'To generate the driving voltage data
    v = 40
    ReDim voltage(v)
    voltage(0) = 0
    For i = 1 To v - 1
    voltage(i) = voltage(i - 1) + 0.003
    Next
    -----------------------------------------
    Agt3494A1.Address = "COM1::Baud=9600,Parity=none,Size=8,Handshake=dtr_dsr"
    Agt3494A1.Output "apply:DC DEF,DEF,0"
    -----------------------------------------
    'To set the parameters of the Agt54641A oscilloscope
    vdiv = 0.02
    acqsize = 2000
    Agt3494A1.Address = "GPIB::7"
    Agt3494A1.Output "*RST"
    Agt3494A1.Output ":TRIGGER:MODE EDGE"
    Agt3494A1.Output ":TRIGGER:SOURCE EXTERNAL"
    Agt3494A1.Output ":TRIGGER:LEVEL 0.5"
    Agt3494A1.Output ":TRIGGER:COUPLING AC"
    Agt3494A1.Output ":TIMEBASE:SCALE 270.0E-06"
    Agt3494A1.Output ":TIMEBASE:POSITION 4.13E-3"
    Agt3494A1.Output ":CHANNEL1:SCALE " + CStr(vdiv) + "E+00"
    Agt3494A1.Output ":CHANNEL1:PROBE 1"
```

```
    Agt3494A1.Output ":CHANNEL1:OFFSET -0.1"
    Agt3494A1.Output ":CHANNEL1:COUPLING AC"
    Agt3494A1.Output ":ACQUIRE:TYPE AVERAGE"
    Agt3494A1.Output ":ACQUIRE:COUNT 32"
    Agt3494A1.Output ":WAVEFORM:FORMAT BYTE"
    Agt3494A1.Output ":WAVEFORM:SOURCE CHANNEL1"
    Agt3494A1.Output ":WAVEFORM:POINTS " + CStr(acqsize)

End Sub
-------------------------------------------------
‘The main program for the data acquisition process
Private Sub startmeasure_Click()
    ReDim wavedata(v, acqsize)
    For i = 0 To v - 1
        Agt3494A1.Address = "COM1::Baud=9600,Parity=none,Size=8,Handshake=dtr_dsr"
        Agt3494A1.Output "apply:DC DEF,DEF, " + CStr(voltage(i))
        Call timedelay
        Agt3494A1.Address = "GPIB::7"
        Call GETWAVEFORM(i)
        DoEvents
    Next
    Call writefiledata
    Agt3494A1.Output ":RUN"
    Agt3494A1.Address = "COM1::Baud=9600,Parity=none,Size=8,Handshake=dtr_dsr"
    Agt3494A1.Output "apply:DC DEF,DEF,0"
    Unload Me
End Sub
-----------------------------------------------------
‘Read signal data from the oscilloscope
Private Sub GETWAVEFORM(i)
    Agt3494A1.Output ":DIGITIZE CHANNEL1"
    Agt3494A1.Output ":WAVEFORM:DATA?"
    Agt3494A1.Enter reading, "I1"
    For j = 0 To UBound(reading)
        wavedata(i, j) = reading(j)
    Next
 End Sub
-------------------------------------------------
‘Log the signal data and driving voltage data to the file "c:\test.txt"
Private Sub writefiledata()
Dim fnum As Integer
```

```
fnum = FreeFile()
Open "c:\test.txt" For Output As #fnum
Print #fnum, v
For i = 0 To v - 1
   Print #fnum, voltage(i)
Next
Print #fnum, acqsize
For i = 0 To v - 1
   For j = 0 To acqsize - 1
      Print #fnum, wavedata(i, j)
   Next
Next
Close #fnum
End Sub

Private Sub timedelay()
      For k = 1 To 1700000 '9000000
         k = k + 1
         k = k - 1
      Next
End Sub
Private Sub exit_Click()
   Unload Me
End Sub
```

(b): Matlab source code for the data processing of the measurement in Fig. 4.9 (c)

```
clc
clear all
-------------------------------------------
% To extract signal data, voltage data and acquisition number from the file "C:\test.txt"
load C:\test.txt;
voltage=test(2:test(1)+1);
acqsize=test(test(1)+2);
waveform=test(test(1)+3:length(test));
lengthv=length(voltage);
data=reshape(waveform,acqsize,lengthv);
-------------------------------------------
logdata=data<max(max(data));
srchr=(acqsize/5);
ladder=0:srchr;
for i=1:lengthv
   srchst=fix(acqsize/10);
-------------------------------------------
% To separate two ranges in each waveform, so as to make sure that there is only one trough in each range.
   for j=1:2
      for m=srchst:acqsize-1
         if logdata(m,i)<logdata(m+1,i)&logdata(m,i)<logdata(m+fix(acqsize/30),i)
            s(j)=m; break
         end
      end
      srchst=m+srchr;
   end
   -------------------------------------------
   % To determine the trough position in each range.
   for j=1:2
      [btom,T]=min(data(s(j):s(j)+srchr,i));
```

```
        vb=btom;
        vt=max(max(data));
        t=vb<data(s(j):s(j)+srchr,i)&data(s(j):s(j)+srchr,i)<vt;
        w=t.*ladder';
        w1=w(1:T);
        w1=nonzeros(w1);
        wd1=s(j)+w1-1;
        min1=min(wd1);
        max1=max(wd1);
        w2=w(T:srchr+1);
        w2=nonzeros(w2);
        wd2=s(j)+w2-1;
        min2=min(wd2);
        max2=max(wd2);
        ind1=min1+sum(data(min1:max1,i)-data(max1,i))/(data(min1,i)-data(max1,i));
        ind2=min2+sum(data(max2,i)-data(min2:max2,i))/(data(max2,i)-data(min2,i));
        d(j,i)=(ind1+ind2)/2;
    end
    ----------------------------------------
    period(i)=abs(d(1,i)-d(2,i));
end
-----------------------------------------------
% To calculate the phase shift
shift(1)=0;
for i=1:lengthv-1
    for j=1:2
        for k=1:2
            m(j,k)=d(j,i)-d(k,i+1);
        end
    end
    shift(i+1)=shift(i)+mean(m(find(abs(m)<meanp/2)))/meanp*180;
end
shift=shift'*sign(shift(fix(lengthv/2)))*632.8/360;
```

```
-----------------------------------
% To calculate the measurement standard deviation.
p=polyfit(voltage,shift,1);
fitval=polyval(p,voltage);
rms=std(shift-fitval)
-----------------------------------
% To create the figure
figure
set(gcf,'unit','centimeters','position',[4,4,20,10])
plot(voltage,shift,'.',voltage,fitval,'r','markersize',15)
set(gca, 'fontsize',12,'ylim',[-1 +inf],'xtick',0:0.02:0.12)
xlabel('Voltage (V)','fontsize',14)
ylabel('Displacement (nm)','fontsize',14)
text(0.01,18,{'Average Number=' ['RMS=' num2str(rms,2)]},'fontsize',14)
---------------------------------
```

Appendix C: Program for automatic glass scribing

This program is written in Ladder-X language.

Return the robot to home position.								
	HOMSQ	AXY						
Set jumping line index								
	INDEX	1						
The speed of scribe wheel is set to be 250mm/sec, The normal speed range is 200 ~ 300mm/sec (see reference [61]), 0.12 is acceleration setting of robots.								
	SPEED	250	0.12					
Store value to variable register J001, which stores the x scribing repeating times.								
	LET	J001	1					
Store the y scribing repeating times to variable register J002.								
	LET	J002	3					
Store the dimensions for x scribing to variable register K001~004.								
	LET	K001	31					
	LET	K002	31					
	LET	K003	36					
	LET	K004	0					
Store value to variable registers W001 and W002, the meanings are shown in Fig. C-1								
	LET	W001	-1.1					
	LET	W002	-0.8					
Store value to variable registers K005~008, which store the dimensions for y scribing.								
	LET	K005	23.7					
	LET	K006	11					
	LET	K007	0					
	LET	K008	0					
Copy the coordinates data of point P0103 to P0101, P0104 to P0102.								
	POSCP	P0103	P0103	P0101				
	POSCP	P0104	P0104	P0102				
To wait the “start” button to be pressed								
	SQMWT							
SQM	LDI0001	AI0002						
To read the x coordinate value of point P0101 into variable register K010.								
	POSRD	K010	P0101	AX				
Add the value of W001 to K010, and save the sum into K010.								
	ADD	K010	W001					
Go to subroutine with line index of H1, which is for execution of x scribing.								
	GOSUB	H1						
Store 1 into variable register J007								
	LET	J007	1					
Use “For …Next” statement to start the cycle of x cutting.								
	FOR	J007	J001	1	F0000	F0000		

If the datum stored in K001 is not equal to zero, save the sum of K010 and K001 into K010, and go to subroutine with index H1, this subroutine is for execution of x scribing.								
	IF	K001	0				F0000	
	ADD	K010	K001					
	GOSUB	H1						
	ELSE							
	ENDIF							
If the datum stored in K002 is not equal to zero, execute the next line. Otherwise, break the “If…End if” statement.								
	IF	K002	0				F0000	
To save the sum of K010 and K001 into K010.								
	ADD	K010	K002					
To go to subroutine with index 1. This subroutine is for execution of x scribing.								
	GOSUB	H1						
	ELSE							
	ENDIF							
	IF	K003	0				F0000	
	ADD	K010	K003					
	GOSUB	H1						
	ELSE							
	ENDIF							
	IF	K004	0				F0000	
	ADD	K010	K004					
	GOSUB	H1						
	ELSE							
	ENDIF							
	NEXT							x scribing finished
Below is the code for y scribing, the meaning of each statement is the same as those for the x scribing.								
	POSRD	K011	P0102	AY				
Store the sum of -32.4 and W002 into W002. -32.4 mm is the position difference between x scribe wheel and y scribe wheel.								
	ADD	W002	-32.4					
	ADD	K011	W002					
	GOSUB	H2						
	LET	J007	1					
	FOR	J007	J002	1	F0000	F0000		
	IF	K005	0				F0000	
	ADD	K011	K005					
	GOSUB	H2						
	ELSE							
	ENDIF							
	IF	K006	0				F0000	

	ADD	K011	K006					
	GOSUB	H2						
	ELSE							
	ENDIF							
	IF	K007	0				F0000	
	ADD	K011	K007					
	GOSUB	H2						
	ELSE							
	ENDIF							
	IF	K008	0				F0000	
	ADD	K011	K008					
	GOSUB	H2						
	ELSE							
	ENDIF							
	NEXT							y scribing finished
Move the robot to position P0050, so as to be ready for next execution.								
	MOVEP	P0050						
Jump to the line with index 1, waiting for the “start” button to be pressed to start the next scribing routine.								
	JUMP	1						
The subroutine with index of 1 is for execution of x scribing.								
1	SRBGN							Subroutine begin
Write the datum stored in register K010 into the x coordinate of P0101.								
	POSWT	P0101	K010	AX				
To move the scribe wheel to point P0101.								
	MOVEP	P0101						
To put down the x scribe wheel.								
	DOSET	O0004						
To give 0.5 second time for the execution of the air cylinder for putting down x scribe wheel.								
	TIMEW	50						0.2sec
To move the scribe wheel by the increment stored in P0090 at a speed of 20 mm/sec, the low speed is to reduce the impact of the scribe wheel to the glass edge.								
	MOVEI	P0090		20				
To move the scribe wheel by the increment stored in P0091								
	MOVEI	P0091						
To resume the position of scribe wheel.								
	DORST	O0004						
To give 0.5 second time for the execution of the air cylinder for raising the x scribe wheel.								
	TIMEW	50						
	SREND							Subroutine end
The subroutine with index of 2 is for the execution of y scribing. The meaning of each								

Vacuum Hol
Sea

statement is the same as those in the subroutine for the execution of x scribing.								
2	SRBGN							
	POSWT	P0102	K011	AY				
	MOVEP	P0102						
	DOSET	O0005						
	TIMEW	50						
	MOVEI	P0092		20				
	MOVEI	P0093						
	DORST	O0005						
	TIMEW	50						
	SREND							

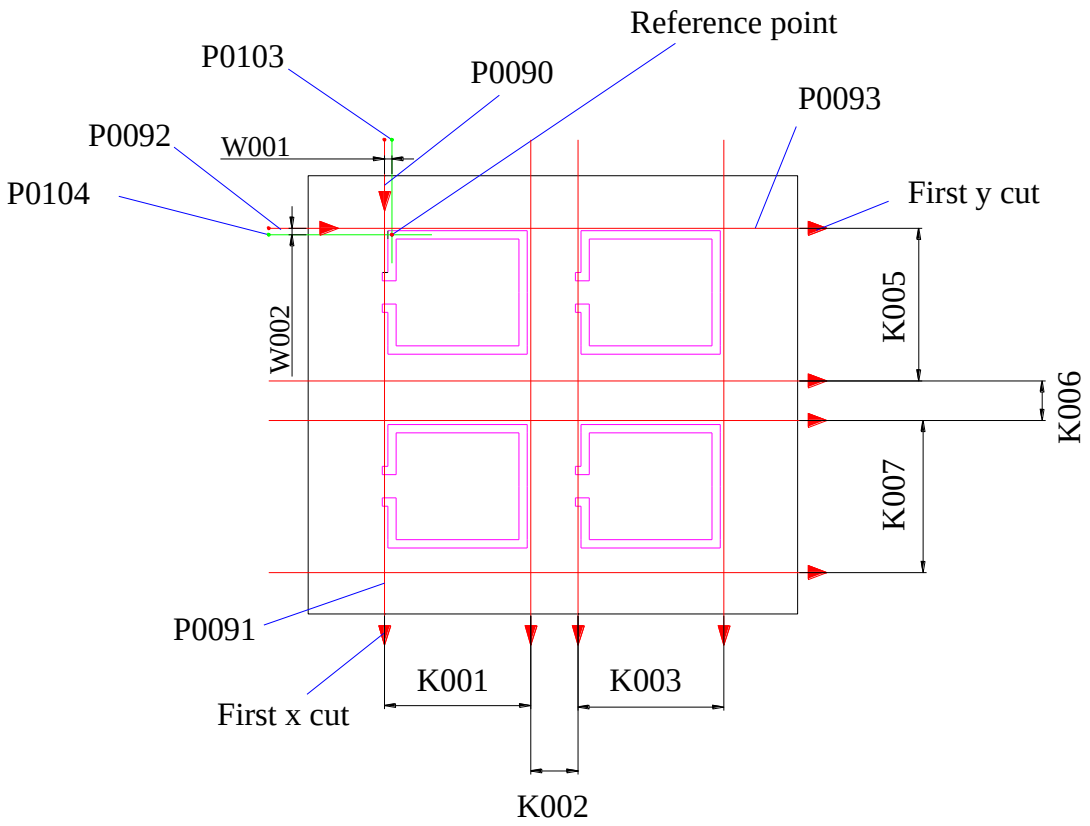

Fig. C-1.Illustration of the parameters for the glass scribing control program. The position coordinates in P0103, P0104, P0090, P0091, P0092 and P0093 are stored in advance.